

به نام خدا



مرکز دانلود رایگان مهندسی متالورژی و مواد

www.Iran-mavad.com



DESIGN OF WELDING ALLOYS CREEP AND TOUGHNESS

By
Murugananth Marimuthu
Queens College, Cambridge

University of Cambridge
Department of Materials Science and Metallurgy
Pembroke Street, Cambridge CB2 3QZ

A dissertation submitted for the degree of
Doctor of Philosophy
at the University of Cambridge
November 2002

Preface

This dissertation is submitted for the degree of Doctor of Philosophy at the University of Cambridge. The research described herein was conducted under the supervision of Prof. H. K. D. H. Bhadeshia in the Department of Materials Science and Metallurgy, Cambridge, between October 1999 and October 2002. This work is to the best of my knowledge original, except where acknowledgement and reference is made to previous work. Neither this, nor any substantially similar dissertation has been or is being submitted for any degree, diploma or other qualification at any other university. This dissertation contains less than 60,000 words.

Parts of this work are published in the following publications:

1. M. Murugananth, H. K. D. H. Bhadeshia, E. Keehan, H. O. Andrén and L. Karlsson. *Strong and Tough Steel Welds*, Mathematical Modelling of Weld Phenomena – 6., H. Cerjak., editor, Institute of Materials, pages 205–229, Graz University of Technology, Graz, 2002.
2. M. Murugananth and H. K. D. H. Bhadeshia. *Components of Creep Strength in Welds*, Mathematical Modelling of Weld Phenomena – 6., H. Cerjak., editor, Institute of Materials, pages 243–260, Graz University of Technology, Graz, 2002.
3. M. Murugananth and H. K. D. H. Bhadeshia. *Components of Creep Strength in Welds–Part II*, Recent Trends in Welding Research., Atlanta, Georgia, USA, 2002 (in press).
4. E. keehan, H. O. Andrén, L. Karlsson, M. Murugananth and H. K. D. H. Bhadeshia. *Microstructural and Mechanical Effects of Nickel and Manganese on High Strength Steel Weld Metal*, Recent Trends in Welding Research., Atlanta, Georgia, USA, 2002 (in press).

5. E. Keehan, L. Karlsson, M. Murugananth , H. K. D. H. Bhadeshia and H. O. Andrén. *High Strength Steel Weld Metals–Developments with Nickel and Manganese*, Today and tomorrow in the science and technology of welding and joining, Proceedings of the 7th International Welding Symposium, Japan Welding Society, pages 797–892, Kobe, Japan, 2001.
6. D. J. Widgery, L. Karlsson, M. Murugananth and H. E. Keehan. *Approaches to Development of High Strength Weld Metals*, 2nd International Symposium on High Strength Steel, Norway, 2002 (in press).

M.Murugananth

Dedication

I would like to dedicate this small piece of work to the Lotus Feet of my beloved Swami, parents (Mrs. R. Saraswathi and Mr. S. Marimuthu), without whose grace, love and forbearance it would not have been possible for me to learn many things not only in science but even in general aspects of life in the course of these three years and all through my life.

*The end of wisdom is freedom.
The end of culture is perfection.
The end of knowledge is love.
The end of education is character.*

*Politics without principles,
Education without character,
Science without humanity, and
Commerce without morality
Are not only useless, but positively dangerous.*

*Knowledge without integrity is dangerous and dreadful,
knowledge without character is a powerful evil.
Knowledge without action is useless; action without knowledge is foolishness.*

- Sri Sathya Sai Baba

Acknowledgements

I would like to thank Professor D. J. Fray for the provision of laboratory facilities in the Department of Materials Science and Metallurgy at the University of Cambridge.

I would like to express my heartfelt thanks to my parents and my supervisor Prof. H. K. D. H. Bhadeshia, whose encouragement and support has made me do this work possible. Moreover, I would like to emphasise the human values like simplicity and elegance that I found in Prof. Bhadeshia that has given me the inspiration to work in the Phase Transformation and Complex Properties Group. Hence, I would like to add a note that it has not only been scientifically beneficial for me, but I have also benefited as a person.

Due acknowledgement goes to Dr. Leif Karlsson, ESAB, Sweden, without whose valuable discussions and help in the mechanical testing of the alloys, this project would be incomplete. Thanks also to Mr. Enda keehan, Chalmers University of Technology for his friendship and discussions.

I would also like to thank the past and present members of the Phase Transformations and Complex Properties Group, in particular Dr. Thomas Sourmail, Dr. Miguel Yescas Gonzalez, Dr. Harsha Sree Lalam, Dr. David Cole, Vicky Yardly, Shingo Yamasaki, Mathew Peet, Dr. Carlos Garcia Mateo, Daniel Gaude-fugarolas, Dr. Yaan de Carlan and Prof. Yanhong Wei.

I would also like to express my thanks to my friends who are not directly related to my work or to the research group, in particular, Ganapathi subbu, Senthil, Rajkumar and Shantanu Madge for the fruitful discussions and entertainment they provided.

Though words are not sufficient to express, I would like to express my heartfelt gratitude to my sisters Ms. Nithyashree and Ms. Vanipriya, fiancée Ms. Pallavi, for the love and encouragement they provided me with.

Many thanks must go to the Nehru Trust for Cambridge University and the Cam-

bridge commonwealth trust for their funding. Also to Queens' college who had helped me monetarily to go for conferences. Last but not the least, I would like to thank all my friends and colleagues who have directly or indirectly helped me.

Abstract

The subject of welding is challenging because of its complexity and because its applications are in the majority of cases, safety critical. An important parameter which features in structural integrity at ambient temperatures is toughness, which essentially is the ability of the material to avoid brittle fracture. In the context of long term service at elevated temperatures of the kind typical in power plant, it is creep which frequently controls the life of components.

The work presented in this thesis deals with both these aspects from the point of view of welding alloys. Research has been in progress over many years to try and improve the toughness and strength of best available commercial alloy, but without much success.

It is frequently observed that the toughness of a steel or steel weld-metal decreases as it is strengthened. Brittle failure occurs when the stress required to cleave the metal becomes small compared with that needed to cause gross plastic deformation. It is natural therefore, that anything which makes plastic flow more difficult must lead to a greater risk of brittle failure unless something is done also to improve the resistance to cleavage.

It is common to add nickel to a ferritic steel in order to enhance toughness. However, it was demonstrated using models that contrary to popular belief, nickel does not improve the toughness at high concentrations of manganese. Indeed, it only enhances toughness when the manganese concentration is kept below a critical value.

The calculations, done using neural network within a Bayesian framework, have been verified experimentally and it is demonstrated that the *predicted* large improvement in toughness can indeed be achieved in practice. The work has also demonstrated the power of the method to assimilate the simultaneous effect of large number of variables, a feat which is hard to achieve when making qualitative judgements about complex phenomena.

A considerable amount of work has been done to investigate the mechanism of the

nickel-manganese effects. X-ray diffraction was used to measure the amount of retained austenite. Microstructural studies done using optical and scanning electron microscopy showed mixed microstructures of bainite and martensite.

Dilatometric analysis revealed that as expected, the low manganese alloys had a higher Ac_1 temperature where austenite formation begins during heating. This, in combination with tempering effects lead to a combination of soft and hard regions in the material exposed to a Charpy test. This was verified by high-resolution hardness map of the whole weld. This revealed that the weld with a low manganese concentration had a correspondingly smaller average hardness than that with a higher manganese concentration. The latter also contained localised regions with excessive hardness. This explains the improvement in toughness of the high nickel-low manganese steel welds.

On another aspect, previous work has focused on the quantitative modelling of the creep rupture strength of steel welds as a function of the chemical composition and heat treatment. The second part of the present work represents a first attempt at making these models more physically transparent.

Modern power plant steels and welding alloys, designed to resist creep deformation at high temperatures, contain a myriad of alloying elements and a microstructure which has six or more phases. It has not therefore been possible to identify the precise role of each chemical and microstructural component in determining the ultimate creep properties.

A combination of models and a knowledge of the mechanical properties and microstructure was used to factorise the long-term creep rupture strength into individual contributions. For example due, to solution strengthening, precipitate strengthening *etc.* The factorisation is non-linear and relies on thermodynamic and mechanical property models. The work is generic in the sense that it covers all common ferritic steels and welding alloys of the type used in the construction of power plant.

An assessment is included of some of the most modern alloys with interesting conclusions on the factors making major contributions to the long-term creep rupture strength.

Contents

ABSTRACT	i
NOMENCLATURE AND ABBREVIATIONS	vii
1 INTRODUCTION	1
1.1 Manual–Metal Arc Welding	2
1.2 Mechanical Properties	4
1.2.1 Stress–strain curve	4
1.2.2 Toughness	5
1.3 Solidification and Microstructure in Welds	8
1.4 Multirun Welds	9
1.5 Segregation during Solidification	11
1.5.1 Scheil Theory	14
1.6 Creep	15
1.6.1 The technical creep curve	15
1.6.2 Creep mechanisms	16
1.7 Factors Influencing Resistance to Creep	21
1.8 Ferritic Power Plant Steels	21
2 EVOLUTION OF STRONG AND TOUGH STEEL WELDS	24
2.1 Nickel–Containing Welds	24
2.1.1 Austenite formation in nickel steels	28

2.1.2	Austenite precipitation	28
2.2	Nickel-Manganese Steel Welds	32
2.3	Summary	36
3	EXPERIMENTAL TECHNIQUES	37
3.1	Manufacture of Weld Metals	37
3.2	Dilatometry using Thermecmastor Z thermomechanical simulator	38
3.3	Temperature Dependence of Hardness	38
3.4	Retained Austenite Measurement using X-ray Diffraction	40
3.5	Mechanical Testing	42
3.6	Metallography	42
3.7	Transmission–Electron Microscopy	43
3.7.1	Thin-foil steel specimens	43
3.7.2	Carbon replicas	43
4	ARTIFICIAL NEURAL NETWORKS	46
4.1	Basics of Neural Networks - An Overview	46
4.1.1	Training	48
4.1.2	Error estimates	49
4.1.3	Overfitting	50
4.2	Best Model and Committee	52
4.3	Computation of Weights - Probabilistic Approach	52
4.4	Model Development Procedure	54
5	RESULTS AND DISCUSSION	56
5.1	Artificial Neural–Network	57
5.2	An Optimum Composition	58
5.3	Toughness Improvement - Contribution due to Metallurgical factors	62

5.3.1	Temperature dependence of hardness	62
5.3.2	Retained austenite measurements	65
5.3.3	Effect of alloying on Ac_1 and uniformity of microstructure	66
5.3.4	Strain hardening versus toughness	67
5.3.5	Hardness maps and microstructure	68
5.3.6	Segregation	69
5.4	Strengths of Heat-Treated Welds A and C	70
5.5	Effect of Interpass Temperature on Low-Manganese High-Nickel Weldments	71
5.6	Tempering Resistance of 7Ni-2Mn and 7Ni-0.5Mn wt% Welds	71
5.6.1	Transmission-electron microscopy of tempered steels	72
5.7	Discussion and Conclusions	72
6	FERRITIC POWER PLANT STEELS	90
6.1	Design Philosophy	91
6.2	Precipitates in Power Plant Steels	97
6.2.1	$M_{23}C_6$	99
6.2.2	Laves phases	100
6.2.3	M_6C	100
6.2.4	M_7C_3	101
6.2.5	MX	101
6.2.6	Cementite	101
6.2.7	M_2X	101
6.3	Microstructure of Heat-Resistant Steels	103
6.4	Precipitate Stability	103
6.4.1	The stability parameter	104
6.5	Development of Heat-Resistant Steels	107

7	THE HYBRID MODEL	110
7.1	Phase Stability Calculations	111
7.1.1	System	111
7.1.2	Source	111
7.1.3	Selection of phases	111
7.1.4	Calculation of equilibrium precipitates	111
7.2	Database and Model Construction	112
7.3	Predictability of the Model	113
7.4	Summary	115
8	FACTORISATION OF THE CREEP STRENGTH OF $2\frac{1}{4}$Cr-1Mo, NF616 and HCM12A	122
8.1	Case Study: $2\frac{1}{4}$ Cr1Mo Steel	123
8.2	Case Study: NF616 Steel	128
8.3	HCM12A	131
8.3.1	Components of Creep Strength	136
8.4	Summary	141
9	SUMMARY AND FUTURE WORK	142
	APPENDIX I	145
	APPENDIX II	148
	APPENDIX III	152
	APPENDIX IV	156
	APPENDIX V	160
	BIBLIOGRAPHY	176

Nomenclature and Abbrevations

α	Low temperature ferrite
$\dot{\epsilon}_{ss}$	Steady-state strain rate
$\Delta\sigma_{X_{ss}}$	Change in creep-strength due to variation in concentration of dissolved alloying element X
γ	Austenite
σ_w	Standard deviation in the distribution of weights
$\sigma_{0.2\%}$	Proof stress at 0.2 % plastic strain
σ	Stress
σ_{pha}	Sigma phase (intermetallic compound of iron and chromium)
σ_{int}	Interfacial energy
$\sigma_y^{(m)}$	Standard deviation of variable y
α, β	Regularisers
σ_ν	Perceived noise
τ	Shear stress
Ac_1	Temperature at which ferrite starts transforming into austenite during heating (Ac stands for Arret Chauffage)
Ac_3	Temperature at which the sample becomes completely austenitic during heating
Ae_1	Equilibrium austenite + ferrite (or) ferrite + cementite phase boundary
Ae_3	Equilibrium austenite and austenite + ferrite phase boundary
AWS	American Welding Society
b	Burgers vector
BCC	Body-centered cubic
BS	British standard
C^L	Concentration of solute in liquid
C_0	Average solute concentration
C^S	Concentration of solute in solid
$c^{\alpha\theta}$	Concentration of solute in α in equilibrium with θ
$c_r^{\alpha\theta}$	Concentration of solute in α in equilibrium with precipitate θ of radius r
$c^{\theta\alpha}$	Concentration of solute in θ in equilibrium with α
D	Diffusion coefficient
D_{eff}	Effective diffusion coefficient
D_i	Diffusion coefficient of component i
E_D	Error
e^{-2m}	Temperature factor
F	Structure factor
FCC	Face-centered cubic

f_s	Fraction of liquid solidified
HAZ	Heat-affected zone
HI	Heat input
I_γ	Integrated intensity of austenite peak
I_α	Integrated intensity of ferrite peak
k	Partition coefficient
k_{bolt}	Boltzmann constant
LPE	Log predictive error
L_p	Lorentz polarisation factor
MMAW	Manual metal arc welding
MTDATA	Metallurgical Thermochemical databank
M_s	Martensite start temperature
n	Strain hardening exponent
pwhtT	Post-weld heat treatment temperature
pwhtt	Post-weld heat treatment time
Q	Activation energy
R	Gas constant
r	Radius of precipitate
T	Temperature
T_M	Temperature of melting
T_t	Transition temperature
UTS	Ultimate-tensile strength
VHN	Vickers hardness number
v	Velocity of interface between precipitate and matrix
V^α	Molar volume of ferrite
V_γ	Volume fraction of austenite
V_α	Volume fraction of ferrite
\bar{x}	Mean
x_N	Normalised value of x
X_{ss}	Dissolved solute X
YS	Yield strength

Chapter 1

INTRODUCTION

One of the most useful materials for structural applications is steel, with its incredible versatility and low production costs. The world's steel production has increased from approximately 770 million tons in 1989 to about 850 million tons in 2001 [1]. This versatility is a consequence of the natural complexity of the iron-carbon system. An even wider-range of steels can be produced by alloying with other elements and by using suitable mechanical and heat treatments. Diverse properties, for example, yield strengths in the range 200 MPa to 5000 MPa can be obtained commercially at a cost which is affordable.

Many applications require a strong joint between steel components. Joining two pieces of steel by welding is an established process, which probably originated in the era when man first became proficient in the manufacture of wrought iron; the process of working the pasty metal so as to expel the entrapped slag, was effectively one involving fracture and joining. Certainly, hammer-welding was well known more than a thousand years ago; witness, for example, the well known Damascus swords [2]. These and many other specimens of ancient and medieval swords were produced by welding strips of high-carbon to low-carbon steel, forging the composite metal, doubling it upon itself, again welding and forging, and repeating these steps until a finely laminated strip was obtained from which the blade was forged and ground. Such a weapon could be hardened to give it a keen cutting edge, but it was also ductile enough so that it would not shatter in combat.

The application of welding to the mass production of machines, structures, and equipment dates only from about the time of World War I (1914). After the Germans smashed the cast-iron cylinders of the large reciprocating engines in their interned ships, the seemingly irreparably damaged cylinders were carefully fitted together and welded. The attendant publicity gave modern welding its start. During the following six decades the use of welding multiplied rapidly and today this method of joining has a dominant feature in modern life.

A weld as defined by the American Welding Society [3], is a localised coalescence of metals. This coalescence is usually brought about by the application of heat, with or without fusion, with or without the addition of filler metal, and with or without the application of pressure. From a metallurgical viewpoint, welding processes may be divided into two main categories: fusion and solid-phase welding. Welds in which fusion occurs are, by far, the most common. And one such process is manual metal arc (MMA) welding, an overview of which is presented in the next section.

1.1 Manual–Metal Arc Welding

MMA welding, also known as shielded-metal arc welding, is a fusion welding process in which the base metals are welded using a metal–cored electrode which also serves as filler metal. The electrode essentially consists of a central metallic core and a coating of flux. The core wire is generally made of mild steel, while the alloying elements found in the final weldment come from the metallic powders in the coating. Depending on the nature of the coating, the electrodes are classified into four main types: basic, cellulosic, rutile and acidic. The electrode coating is composed of a mixture of minerals, organic materials, ferro-alloys and iron powder bonded together with sodium or potassium silicate. Cellulosic (BS class C or AWS 6013) electrodes contain cellulose, rutile and magnesium silicate, while

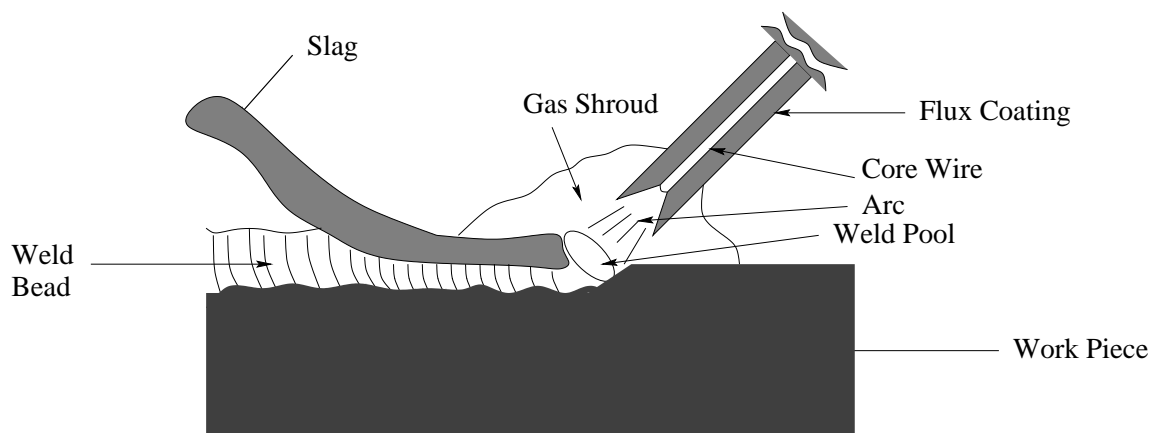


Figure 1.1: Manual Metal Arc Welding

rutile (BS class R or AWS 6013) electrodes contain a small amount of cellulose with rutile and calcium carbonate. Because of the organic content, these types of coatings embody a substantial amount of moisture. Consequently, the gas that is generated during welding by decomposition of the coating contains a high proportion (about 40%) of hydrogen which can embrittle the joint. Basic (BS class B AWS 7015, 7016 and 7018) electrode coatings, on the other hand, contain no organic matter, and therefore can be baked at 400-450 °C, to drive off the bulk of the moisture. The mineral content of such coatings is largely calcium carbonate, which breaks down during welding to provide a CO/CO₂ shield. The volume of gas so generated is smaller than with cellulosic or rutile coatings. Their choice is determined by the characteristics of the arc, the welding position and the type of the weld produced. In MMA welding the drops that transfer from the electrode to the weld pool are coated with slag and the weld pool itself has a slag coating. The self-generated gas is the main protective agent during metal transfer while the slag protects the solidifying and cooling weld metal (Fig. 1.1).

The metals that are joined together are generally known as parent metals or base metals, whereas the solidified region of a weld is known as a “weldment”.

1.2 Mechanical Properties

Most of the mechanical properties of a weldment are different from that of the parents metals. Amongst these properties strength and toughness of a weld are of paramount importance.

1.2.1 Stress–strain curve

A stress–strain curve can be of two types; engineering stress vs engineering strain and true stress vs true strain. An engineering stress is defined as applied load over the initial cross–sectional area, whereas the true stress is applied load over the instantaneous cross–sectional area. Similarly, engineering strain (e) is the change in length divided by the original length, whereas true strain equals $\ln(1 + e)$.

The engineering stress–strain curve is obtained from an uniaxial tension test. It is used widely to provide design information on the strength of materials [4]. A typical stress–strain curve is illustrated in Fig. 1.2. Tensile strength is the maximum engineering stress that a material can withstand before failure. The plastic strain experienced before the onset of necking is known as *uniform strain*. The proof stress is normally obtained at 0.2% of the strain. This can also be approximated from the Vickers–hardness measurements (Eq. 1.1).

$$\sigma_{0.2\%} = 3.27 \times VHN \times (0.1)^n \quad (1.1)$$

where $\sigma_{0.2\%}$ is the proof strength in MPa, VHN is the Vickers hardness number and n is the strain–hardening exponent [4]. Hardness of the steel depends on the type of microstructure amongst other factors. A weldment exhibits different hardness levels in different zones depending on its composition, degree of chemical segregation, thermal cycle encountered and hence the microstructure.

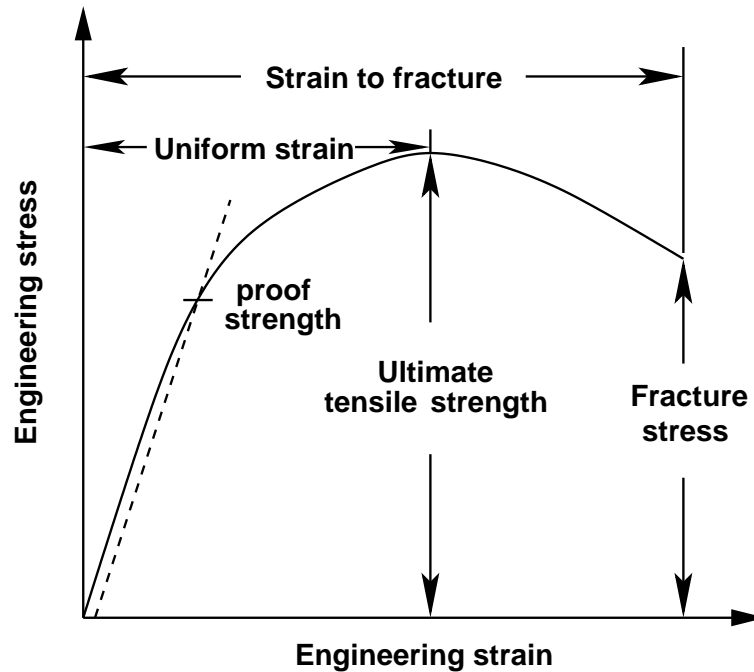


Figure 1.2: Schematic diagram of a typical stress–strain curve.

1.2.2 Toughness

Impact toughness is generally characterised by a Charpy test in which a square sectioned, notched bar is fractured under given conditions and the energy absorbed in the process is taken as an empirical measure of toughness [5]. The purpose of the blunt notch is to concentrate the stress in such a way that it increases the degree of constraint in the vicinity of the notch. The yield stress for plastic flow is therefore raised, making brittle fracture more likely. The tests are conducted over a range of temperatures, and a plot of the impact toughness versus temperature is called the *impact transition curve*, which normally assumes a sigmoidal shape for body-centered cubic (BCC) metals as shown in Fig. 1.3.

The flat region of the curve at high temperatures is called the *upper shelf* and represents ductile failure. The corresponding flat region at lower temperatures is called the *lower shelf* and represents cleavage failure. In the transition region the fracture occurs

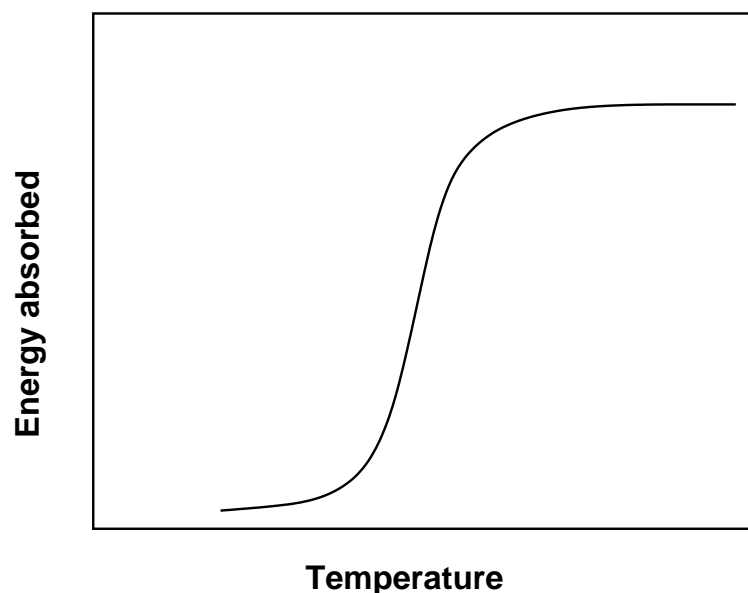


Figure 1.3: Schematic ductile–brittle transition curve as exhibited by all BCC and some FCC metals (e.g. Iridium).

in mixed mode. The impact transition temperature (T_t) is usually defined as that at which fracture surface shows 50% cleavage.

An impact transition temperature is found when cleavage stress is insensitive to temperature, but whose plastic flow stress rises rapidly as the temperature decreases (Fig. 1.4). It is frequently thought that the ductile–brittle transition occurs only in BCC metals, but it is in fact also found in face–centered cubic metals such as rhodium and iridium. Recent work [6] has shown that the condition for the existence of a ductile/cleavage transition is that the ratio of the shear and bulk modulus (μ/K) must exceed a critical value. A large μ implies difficult slip.

The rapid increase in the plastic flow stress is partly a consequence of the Peierls–Nabarro barrier to dislocation motion and partly a consequence of the ubiquitous presence of traces of interstitial elements, which interact strongly with dislocation motion [5]. At the transition temperature the curves representing cleavage and flow cross on a plot of stress versus temperature. Below T_t , the cleavage is easier than plastic flow and *vice versa*.

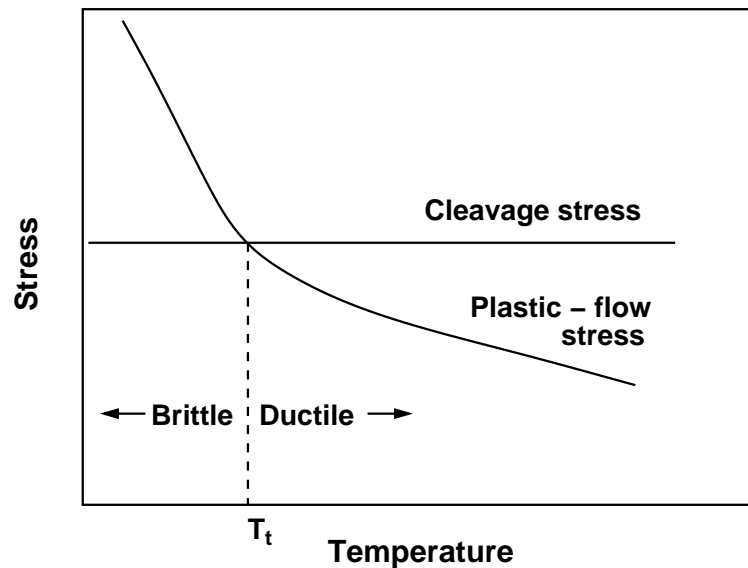


Figure 1.4: Influence of temperature on the stress required for cleavage and plastic flow.

Any effect which raises the plastic yield stress (such as physical constraint caused by a notch) without influencing the nucleation or growth of cleavage cracks inevitably leads to an increase in T_t . In general, cleavage fracture is fast, occurs with little warning, absorbs minimal energy and is undesirable so that a low transition temperature is an important aim in safe design [5].

For any given composition the impact toughness depends mainly on microstructure, grain size and inclusion content. A weldment can have a combination of microstructures due to different cooling rates experienced at different passes. The toughness of a multipass weld is thus a contribution from all the existing phases. An extremely brittle phase like a high carbon martensite would facilitate fast crack propagation (poor toughness), whereas a soft phase like austenite would retard the process of crack propagation (good toughness). Hence, a phase with a high hardness is often not desirable for good toughness. On the other hand, phases like acicular ferrite have a positive effect on toughness [7] making crack propagation difficult.

1.3 Solidification and Microstructure in Welds

Solidification in welding is similar to that occurring in castings except that the mould here is the surface of the parent metal. Unlike in casting, the cooling rate is very high in welds due to high thermal conductivity of the metallic surfaces and small volumes of material involved. Solidification occurs epitaxially at the edge of the fusion zone and progresses inwards in a columnar manner along thermal gradients [8–10]. Grain selection occurs because those oriented with their $\langle 100 \rangle$ directions aligned with the direction of maximum heat flow stifle the growth of other grains. Hence the width of the columnar grains is observed to increase as a function of the distance from the fusion zone boundary.

The microstructure which forms as a steel weld cools from the liquid phase to ambient temperature is called the ‘as-deposited’ or ‘primary’ microstructure. In general allotriomorphic, acicular and Widmanstätten ferrite form the majority of this microstructure (Fig. 1.5). During slow cooling, the first phase to transform from the austenite is allotriomorphic ferrite [11, 12]. Widmanstätten ferrite grows at high temperatures by a paraequilibrium mechanism which involves only diffusion of interstitial carbon, but not substitutional atoms. But due to the high cooling rates involved in welding acicular ferrite or bainite and martensite may be dominant depending on the weld composition. Acicular ferrite unlike bainite is chaotic in nature; it nucleates on non-metallic inclusions and hence grows in many different directions from the nucleation site. However, bainite nucleates by paraequilibrium diffusion of carbon and involves displacive growth. Martensite is formed by diffusionless transformation in steel and occurs when there is sufficient driving force to cause diffusionless nucleation and growth. Martensite forms with a plate morphology that can extend across austenite grains. Hard martensite is not a desirable phase in welds because it is hard and brittle. The hardness of martensite is sensitive to the carbon concentration (Fig. 1.6 [13]).

Fig. 1.7 shows a flow chart summarising the phases that form by the reconstructive

and displacive mechanisms of transformation [5].

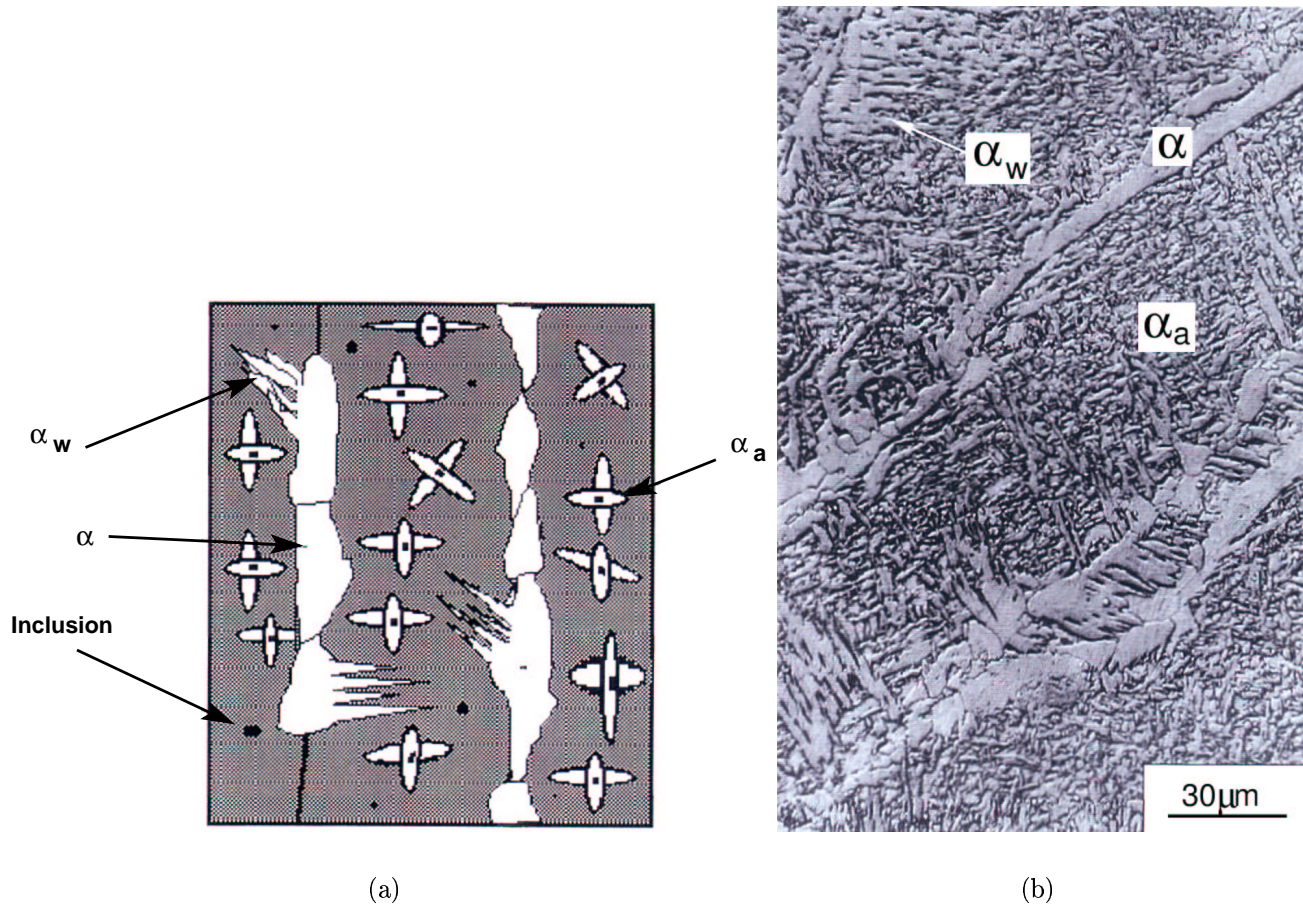


Figure 1.5: a) Illustration of the morphology of allotriomorphic (α), acicular (α_a) and Widmanstätten ferrite (α_w) b) scanning electron micrograph of a weld microstructure [14].

1.4 Multirun Welds

In multirun welds, the gap between the components to be joined is filled using a sequence of weld passes, each of which fills only a part of the weld gap (Fig. 1.8). The metal deposited is therefore influenced significantly by the additional thermal cycles induced by the deposition of subsequent layers. Only the final layer to be deposited can then be

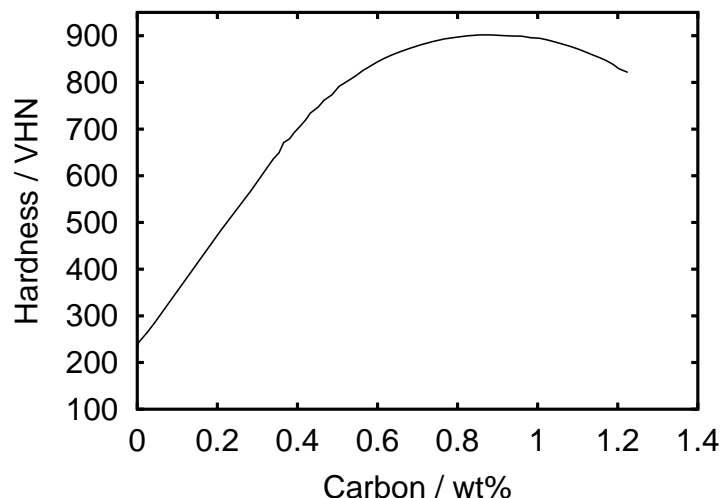


Figure 1.6: Hardness of a martensitic microstructure as a function of carbon concentration. Note that at higher carbon contents fraction of retained austenite increases, thus reducing the overall hardness.

expected to exhibit a true primary microstructure. The remaining regions of the welds may have undergone transient temperature rises high enough to cause partial or complete reverse-transformation into austenite, which on subsequent cooling retransforms to ferrite, but not necessarily to the same microstructure as the primary regions. The regions which do not experience peak temperatures high enough to cause reversion to austenite, are tempered to an extent which is dependent on factors such as the starting microstructure and alloy chemistry. Given that each region of a multirun weld is likely to have experienced a different thermal history, the weld microstructure is expected to be inhomogeneous on a scale related to the dimensions of each weld pass, and on the detailed welding conditions such as the heat input. This should necessarily lead to variations in mechanical properties, a feature which is most obviously reflected in the hardness profiles of such welds. There are indications that welds which are not mechanically homogeneous are susceptible to undesirable scatter in toughness [15–17], scatter which prevents achievement of optimum properties and presents difficulties in engineering design. This phenomenon is widely accepted for wrought steels where a mixture of martensite and bainite leads to scatter in

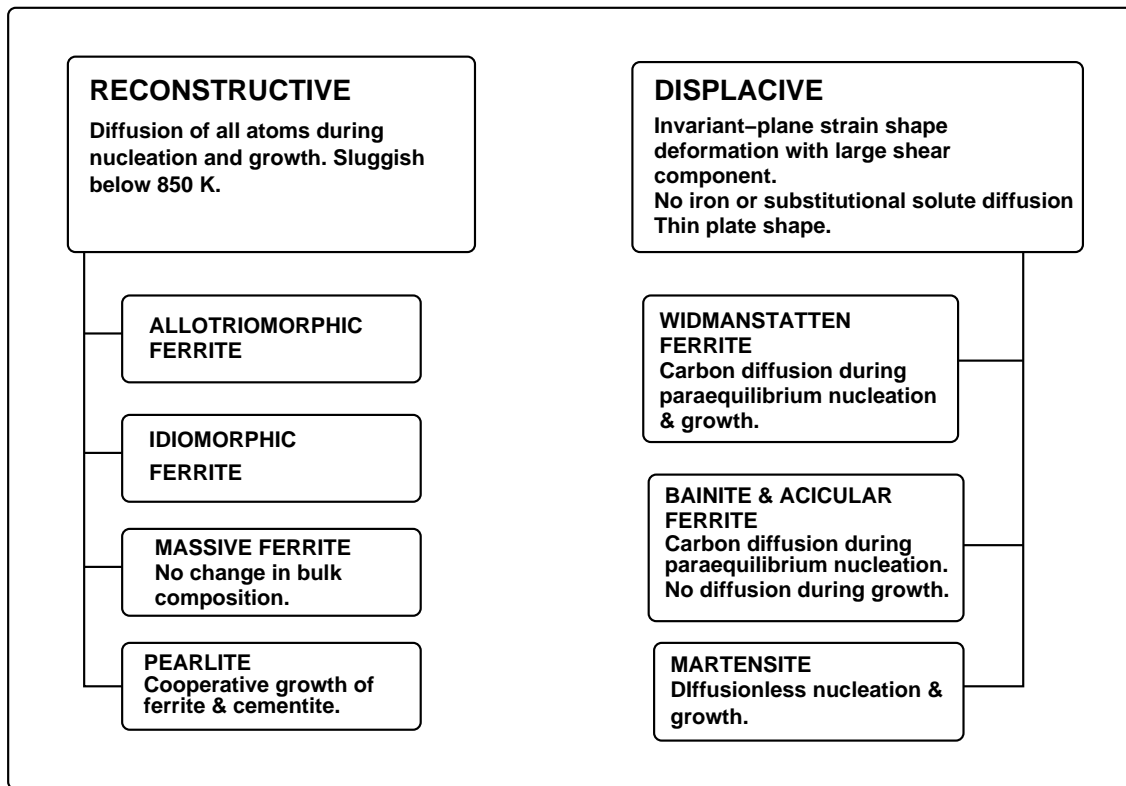


Figure 1.7: Flowchart summarising the characteristics of transformations in steels [5].

toughness larger than the corresponding uniform microstructures with either martensite or bainite [18]. The HAZ formed in the weld beads can be divided into two regions; (a) re-austenitised and quenched, (b) tempered as shown in Fig. 1.9.

1.5 Segregation during Solidification

Solidification in a fusion welding process is analogous to ingot solidification, but occurs at relatively high cooling rates. Three main kinds of solidification behaviour can be observed in alloys [19–22]:

1. During equilibrium solidification diffusion takes place in both the solid and liquid phases, but equilibrium does not generally apply to welding because of the high

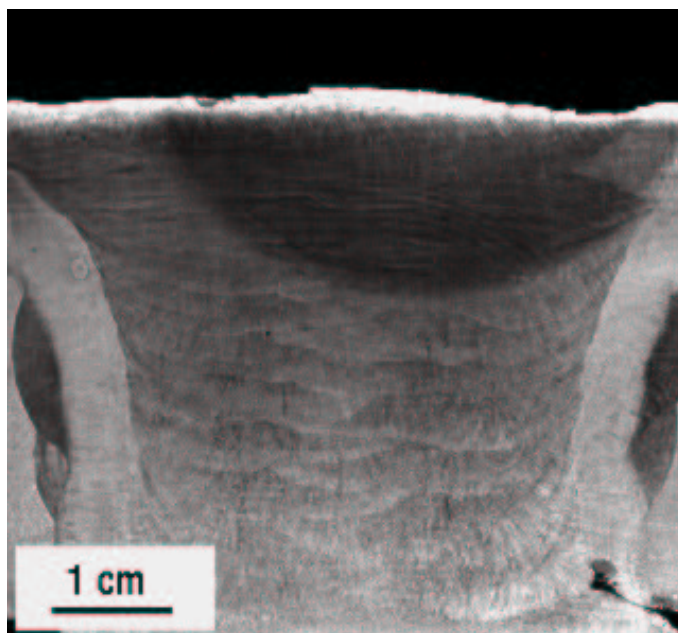


Figure 1.8: Section of multi-run arc weld of Fe-7Ni-0.5Mn wt% steel.

solidification rates.

2. Diffusion can be limited or absent in the solid but with complete mixing in the liquid due to convection and diffusion. This is one of the main causes for microsegregation in weld microstructures.
3. With limited diffusion in liquid due to absence of heat convection and nil diffusion in the solid, there can be no solute boundary layer in front of the solid/liquid interface.

Preferential segregation or partitioning of solute, occurs in most of the solidification processes. The segregation can be classified as either microsegregation (extending over distances of individual grains) or macrosegregation (extending over distances larger than the size of individual grains). Microsegregation can be further divided into cellular, dendritic and grain-boundary segregation. Cellular segregation produces compositional changes over short-distances, and hence can be eliminated by heat treatment. However, the accumulation of solute in interdendritic spaces is more difficult to eliminate. Such segregation occurs either by solute accumulation at grain-boundary grooves or by the

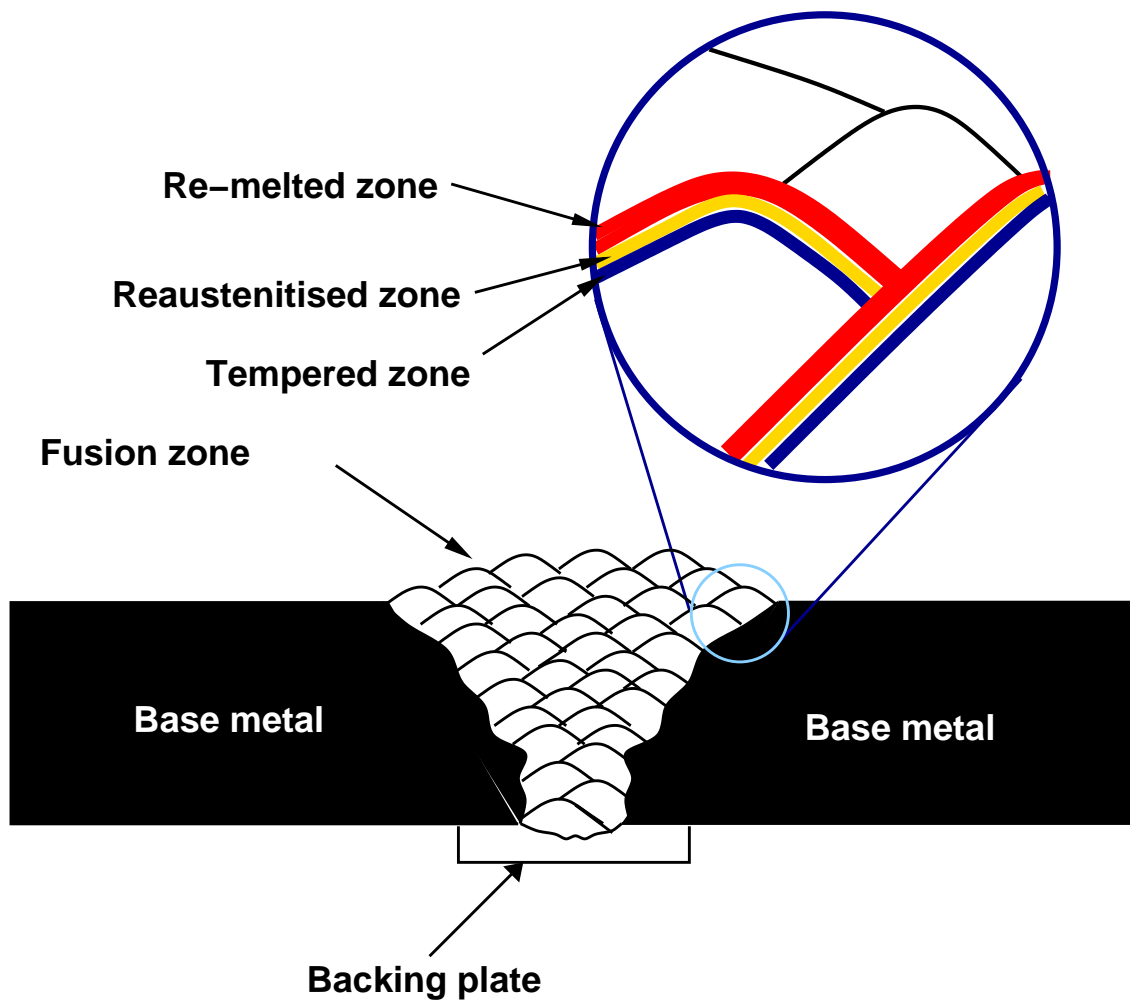


Figure 1.9: Effect of heat from a subsequent pass on the prior passes. Schematic diagram showing the re-melted, reaustenitised and tempered zones in a multipass weld.

impingement of two interfaces growing with a growth component normal to each other. This type of segregation is classified under the macrosegregation category. A characteristic segregation pattern observed frequently in both manual and automatic welding, made with or without the use of filler additions, is solute-banding. This is caused either by enrichment or depletion of solute and can be observed after etching as light and dark regions. Segregation leads to the variation in mechanical properties.

1.5.1 Scheil Theory

During welding, convection in the liquid metal reduces the solute gradients in the liquid. For a liquid of composition C^L (not in equilibrium with the solid), the composition of the solid phase at the interface between solid and the liquid is given by $C^S = kC^L$, where k is the partition coefficient [23]. If f_s is the fraction solidified, then from Fig. 1.10 the increase in solute concentration in the liquid fraction $(1-f_s)$ is equal to the amount of solute rejected during solidification of df fraction of solid given by Eq. 1.2.

$$(C^L - kC^L)df = (1 - f)dC^L \quad (1.2)$$

$$\int_0^{f_s} \frac{df}{1-f} = \int_{C_0}^{C^L} \frac{dC^L}{C^L(1-k)} \quad (1.3)$$

$$\text{so that} \quad C^L = C_0(1 - f_s)^{k-1} \quad (1.4)$$

$$\text{and since} \quad C^S = kC^L \quad (1.5)$$

$$C^S = kC_0(1 - f_s)^{k-1} \quad (1.6)$$

Eq. 1.6 is known as the *Scheil equation*, which gives the concentration of solute in solid, which is not in equilibrium with the liquid.

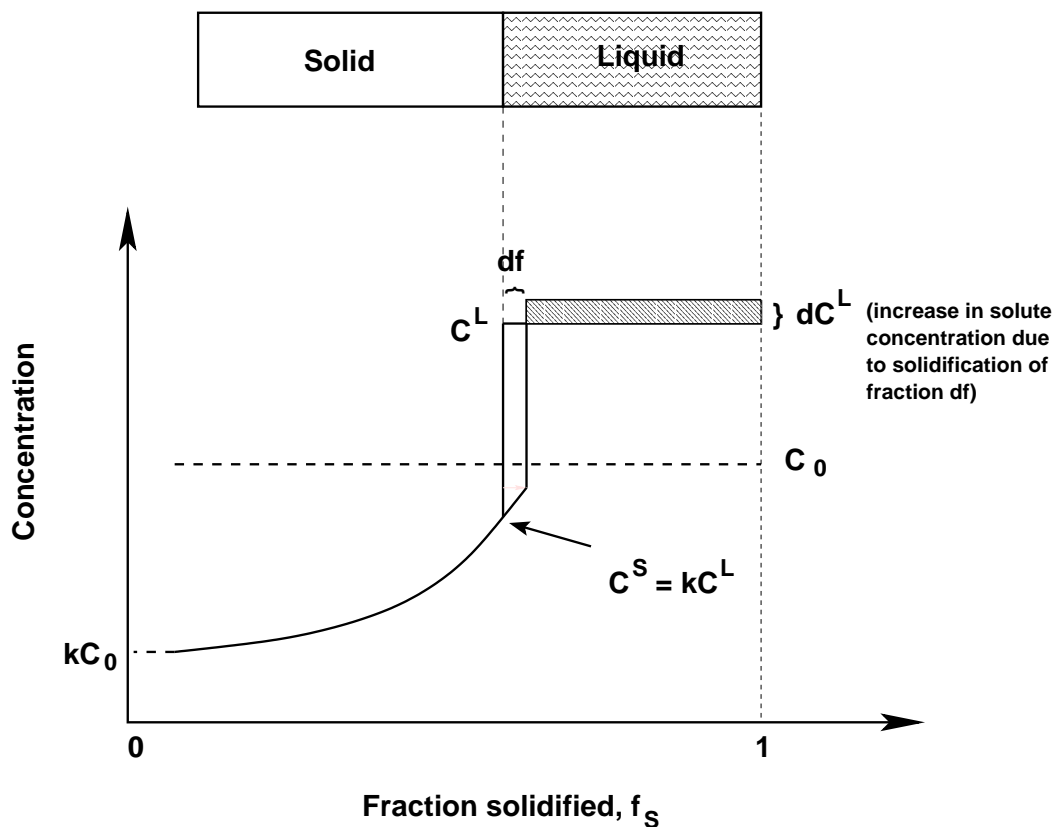


Figure 1.10: Schematic diagram of concentration profile of solute in solid and liquid during solidification, considering no diffusion in solid but mixing in the liquid due to convection.

1.6 Creep

Creep can be described as a time-dependent and permanent deformation of a material when exposed to a constant load, which is generally below the yield strength, at a certain temperature.

1.6.1 The technical creep curve

The usual method of carrying out a creep test is to subject a specimen to a steady tensile load whilst maintaining it at a constant temperature. The elastic and plastic strain on loading are measured as a function of time. The total plastic strain is plotted against time as illustrated in Fig. 1.11.

The region **ABC** is commonly considered as primary or transient creep, **CD** as secondary or steady-state creep and **DE** as tertiary or accelerating creep. Creep rupture occurs at the point **E**. The primary creep could be described as the work-hardening stage for the material in which the resistance to creep is built up by virtue of its own deformation; during secondary creep there is a state of balance between work-hardening and thermal softening; tertiary creep precedes fracture through cavitation, intercrystalline cracking or some other damage mechanism.

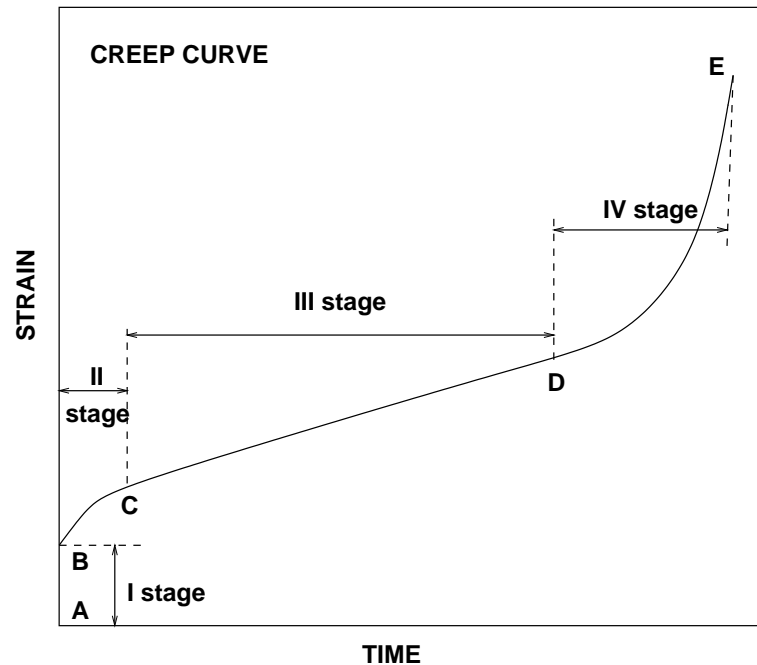


Figure 1.11: General form of strain against time curve. **AB**, elastic extension; **BC**, decreasing creep rate; **CD**, minimum rate of creep; **DE**, increasing creep rate.

1.6.2 Creep mechanisms

Dislocation creep is caused by the diffusion of atoms, which unlock the dislocations that get pinned by obstacles in their path [24]. The movement of dislocations is resisted by the lattice and the obstructing effect of obstacles such as dissolved solute atoms, precipitates or other dislocations.

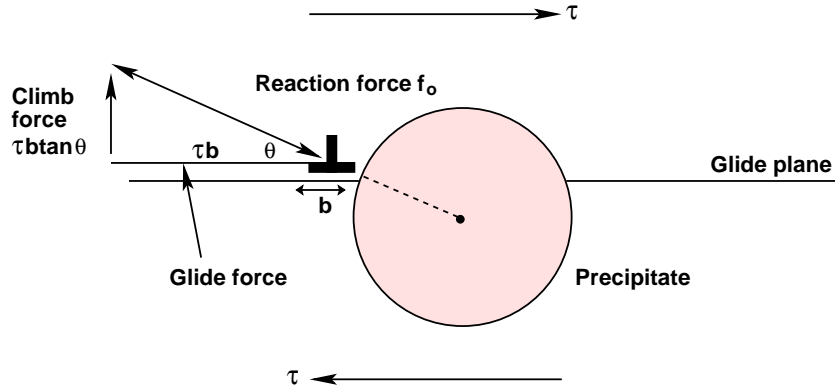


Figure 1.12: Climb force on a dislocation with burgers vector \mathbf{b} due to shear stress τ . \mathbf{b} is along the direction of the shear stress.

It can be seen from Fig. 1.12 [24] that a dislocation whose path is blocked by a precipitate has a perpendicular component of the force $\tau b \tan \theta$ that encourages it to move out of the slip plane. Assuming that the dislocation cannot glide upwards it can move vertically if the lower half of the atoms diffuse away as can be seen from Fig. 1.13 [24]. This process which is widely known as “climb”, requires diffusion and hence can occur only when the temperature is above $0.3T_M$ or so, where T_M is the absolute melting point of the material.

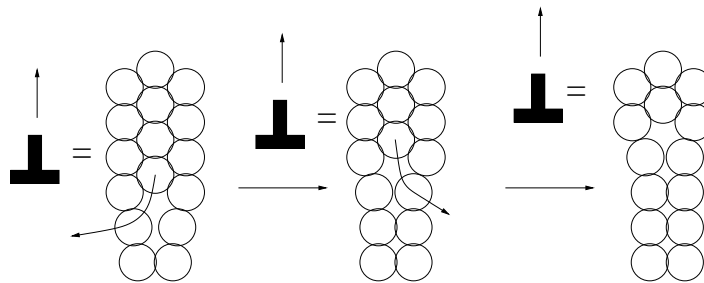
Climb unlocks dislocations from the precipitates which pin them and further slip (or glide) can then take place as seen from Fig. 1.14 [24], leading to creep. This explains the progressive and continuous nature of creep, and the role of diffusion, with diffusion coefficient

$$D = D_0 \exp\{-Q/RT\} \quad (1.7)$$

which explains the dependence of the steady state creep rate $\dot{\epsilon}_{ss}$ on temperature (T), with

$$\dot{\epsilon}_{ss} = A\sigma^n \exp\{-Q/RT\} \quad (1.8)$$

where n is the creep exponent, A is a constant, Q is an activation energy and R is the gas constant. The dependence of creep rate on applied stress σ is due to the climb force:



Atoms diffuse away from the bottom of the half plane.
At high T/T_M this takes place mainly by bulk diffusion through the crystal

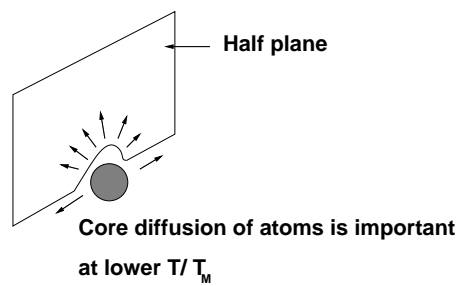


Figure 1.13: Diffusion of atoms leading to climb

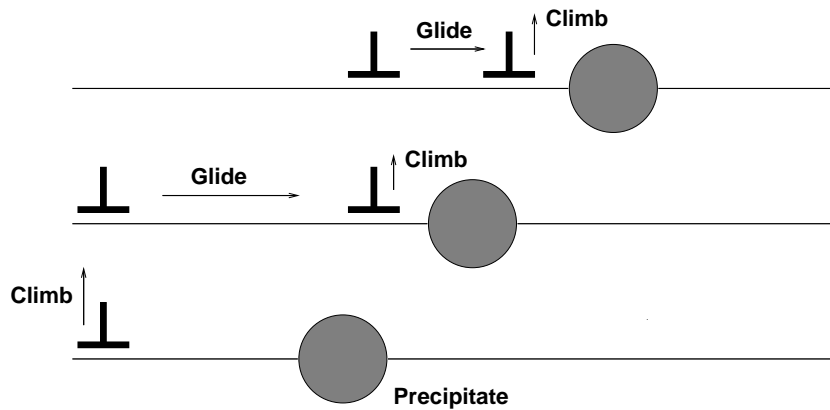


Figure 1.14: Climb-glide sequence leading to creep

the higher σ , the higher the climb force $\tau b \tan \theta$, the more dislocations become unlocked per second, the more dislocations glide per second, and the higher is the strain rate.

Diffusion creep: From Eq. 1.8, it is clear that as the stress decreases, the rate of the power law creep also diminishes, but at this reduced stress level, creep does not come to a halt, it occurs instead by an alternative mechanism. As can be seen from Fig. 1.15 [24], a polycrystal can expand due to the applied stress, σ , by grain elongation; here σ acts as a mechanical driving force but, this time atoms diffuse from one set of the grain faces to the other, and dislocations are not involved. At high T/T_M , this diffusion takes place through the crystal itself, that is, by bulk diffusion. The rate of creep is hence proportional to diffusion coefficient D , and to the stress σ ; and the creep rate varies as $1/d^2$ where d is the grain size. These facts lead to the constitutive equation

$$\dot{\epsilon}_{ss} = C \frac{D\sigma}{d^2} = \frac{C'\sigma e^{-Q/RT}}{d^2} \quad (1.9)$$

where C and $C' = CD_0$ are constants. At lower T/T_M , when bulk diffusion is slow, grain boundary diffusion takes over, but the creep rate is still proportional to σ . In order that holes do not open up between the grains, grain-boundary sliding is required as an accessory to this process.

In summary, creep is a process influenced by temperature, stress and time of expo-

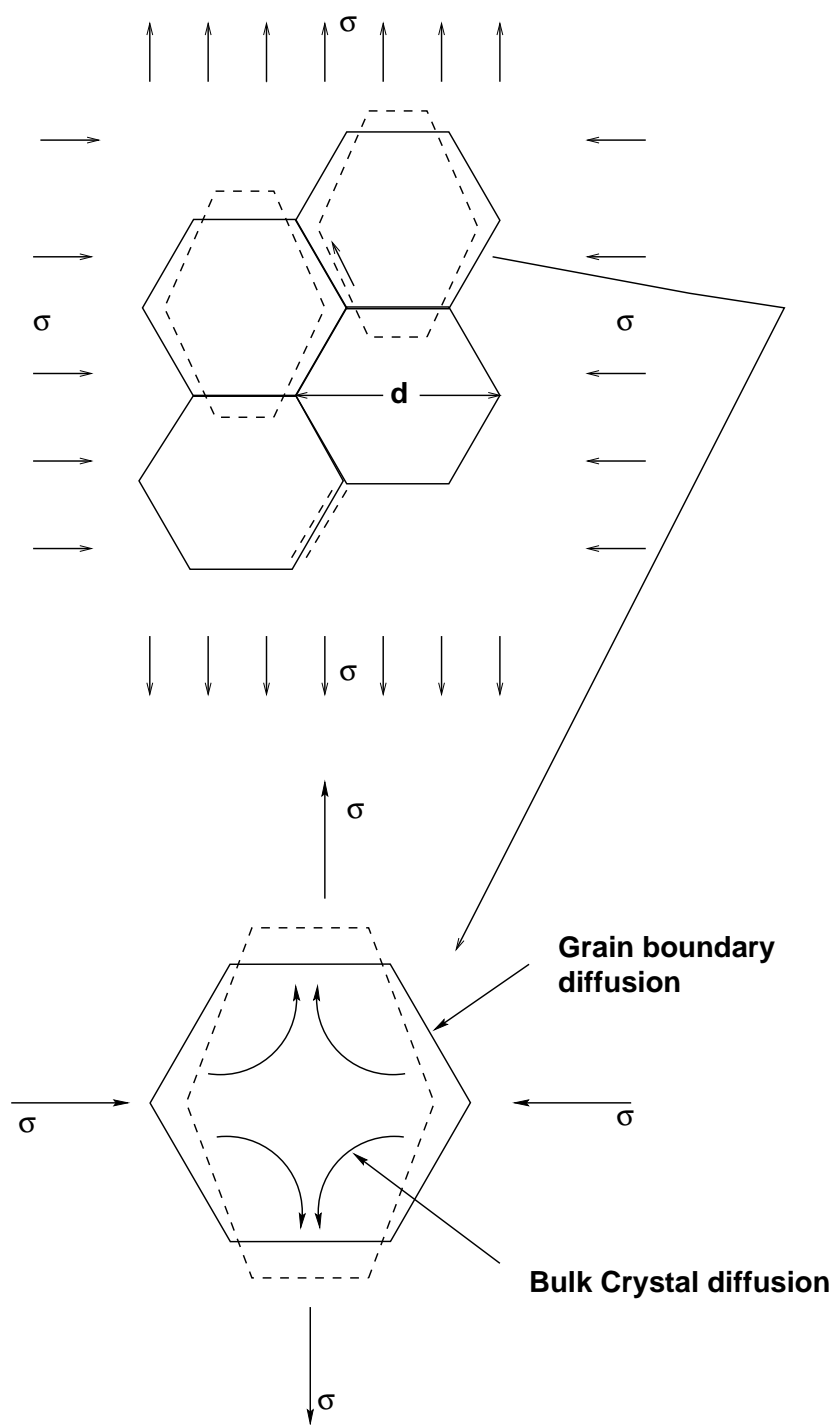


Figure 1.15: Diffusion leading to creep

sure to both these variables. The resistance to creep is an important factor in design of steels used in power plants.

1.7 Factors Influencing Resistance to Creep

The fundamental criterion for resistance to creep is evidently chemical composition. Alloying elements may act in different ways :

1. By raising the recrystallisation temperature of the base material
2. By introducing solute atoms in solid solution in the lattice.
3. By precipitates: carbides, nitrides or intermetallic compounds.

This last factor is the most important in the context of steels for power plant applications. Precipitates impede the movement of dislocations; their mode of action is a function of their size, of their position in the microstructure and their stability. The stability of the microstructure as a whole depends on:

1. Recrystallisation of the matrix.
2. Coarsening of the precipitates, leading to decrease in creep resistance.
3. Dissolution of metastable phases.

1.8 Ferritic Power Plant Steels

Ferritic steels are used extensively in the construction of power plant for electricity generation [25–31]. Their low thermal expansion coefficient and high thermal conductivity

makes them suitable for high-temperature applications. Nickel alloys do have a sufficiently low expansion coefficient, but are expensive.

The main design requirement is that the ferritic steel should resist creep and oxidation, but should at the same time be easy to fabricate into large components. This in turn means that they should be weldable and that any welds must be sufficiently robust to meet the creep requirements. There are in this context, major international research programmes with the aim of designing novel steels and welding alloys [25–31]. The design procedure is based on scientific and engineering experience and the use of a variety of models, for example, phase stability calculations, the assessment of diffusion coefficients, kinetic theory associated with precipitation reactions, elementary creep theory and complex neural network models (as will be discussed later) to express the creep strength as a function of a very large number of variables.

Elementary creep theory, such as that used in the construction of Ashby diagrams, is useful in gaining insight into the creep mechanisms, but is unable to predict the creep behaviour of multicomponent steels as a function of the chemical composition, heat treatment and service conditions. Well-constructed neural network models based on vast experimental datasets are able to cope with such complexity and help visualise the nature of the interactions between variables in a way that is impossible with any other method of pattern recognition [32]. They are, nevertheless, empirical making it difficult to extract physical mechanisms.

The creep resistance of ferritic steels, over long periods of time at elevated temperatures, relies on the presence of stable precipitates which interfere with the climb and glide of dislocations, and which retard the coarsening rate of the microstructure as a whole, for example, the size and shape of martensite or bainite plates. The nature of the precipitate clearly depends on the detailed composition and heat treatment, but the variety is impressive, including Fe_3C (cementite), M_{23}C_6 , M_7C_3 , M_6C , M_2X , Laves, M_5C_2 and Z-phase. There may typically be five or more of these precipitate phases in a creep-resistant steel.

Precipitation also affects the solute left in solution in the ferrite; solution strengthening is believed to be an important component of the long-term creep life. It would be incredibly useful to know quantitatively, the contribution made by each of the precipitate phases, and by solution strengthening due to each solute, to the long-term creep strength. There are currently no models capable either of extracting this information from experimental data or of making quantitative predictions. The purpose of the present work was to attempt precisely this task, using a neural network model but with inputs chosen to represent precipitates and solutes. This is what is known as a hybrid model, *i.e.*, one which takes advantage of known physical relationships but which implements them into an empirical framework capable of dealing with complexity.

Chapter 2

EVOLUTION OF STRONG AND TOUGH STEEL WELDS

Researches in the past and present have discovered ways of producing steels of the desired strength and toughness. There are varying techniques starting from the classical quench and temper method to *in situ* controlled quenching, thermo-mechanical treatments and grain refinement techniques to obtain the desired mechanical properties of a steel. Going further into microstructure, the concept of carbon equivalents has been used extensively to control the toughness and strength of steel by avoiding brittle martensite. A low value of carbon equivalent is supposed to produce less hard martensite thus improved toughness, though at the expense of yield strength.

It has also been common practice to improve the toughness of ferritic steels by increasing the concentration of nickel. The following section discusses the various established facts that contribute to improvement in toughness due to addition of nickel.

2.1 Nickel-Containing Welds

Alloying elements such as nickel are added to steel for many reasons. The increase in hardenability allows more gentle heat treatments and hence mitigates quench cracking by depressing the martensite-start temperature (M_s). Low-carbon martensite can be strong

and tough at very low temperatures. Ni-alloyed steels for cryogenic service are characterised by low levels of the impurity elements such as phosphorus and sulphur, careful control of the interstitial elements, carbon and nitrogen. Aluminium and other elements are added to tie up the interstitial atoms including oxygen and various combinations of the major alloying elements. Manganese and molybdenum give the desired balance of strength, toughness and cost effectiveness to these steels.

The application of a ferritic steel to subzero temperatures is always limited because of the ductile-brittle transition. A transition temperature is a concept that is common in BCC metals whose cleavage stress is insensitive to temperature, but with a plastic flow-stress which increases with decrease in temperature. This increase in flow stress is partly a consequence of the large Peierls–Nabarro barrier to dislocation motion and partly a consequence of the ubiquitous presence of traces of interstitial elements which interact strongly with dislocation motion. However such steels have low thermal expansion coefficient ($\approx 9 \times 10^{-6}/^{\circ}\text{C}$) and are cheap. In 1947 it was shown that a low carbon 3.5 wt% Ni steel has good Charpy impact strength at temperatures as low as -130°C [33]. For a temperature of -196°C , good impact strength can be obtained in low carbon steels containing 8-13 wt% nickel. Later a 5 wt% Ni steel was developed as a lower cost alternative to the 9 wt% Ni steel. The reduction in nickel content can raise the ductile to brittle transition temperature (DBTT) to unacceptable levels. To overcome this problem, some manufacturers replace about 3.5 wt% Ni in this type of steel with 1.5 wt% Mn which gives good impact properties at temperatures as low as -196°C . However, the alloy was found to be sensitive to temper embrittlement and had to be heat treated in too narrow a temperature range to obtain the necessary toughness. The addition of about 0.2 wt% Mo overcomes this problem, by scavenging the impurity atoms. But this can be ineffective as the molybdenum reacts with carbon to form stable carbides, leaving the impurity atoms to segregate to boundaries [34]. Ni-alloyed steels for cryogenic applications can be categorised into three main groups:-

1. **Low Ni concentration (3.5 wt%)**: Steels of this group have low carbon (< 0.2 wt%), Mn up to 0.8 wt%, Si content in the range 0.15-0.3 wt%, low impurity content and are in some cases alloyed with Mo (≈ 0.3 wt%), Cr (up to 1 wt%) and micro-alloyed with Al, Ti or other elements. Applications include storage tanks for ethylene and liquefied petroleum gas, large forgings such as steam turbine shafts, because of their good combination of strength and ductility.
2. **Steels with 5-6 wt%Ni**: These were developed because they are less expensive than 9 wt% Ni steels, still having good impact resistance but somewhat weaker. The carbon is usually < 0.12 wt%, Si is the same as group one but the manganese ranges between 0.3-1.0 wt%, or 1.5-4.5 wt%.
3. **9 wt% Ni steels**: These steels provide an attractive combination of properties at a moderate price, although they are not particularly strong or corrosion resistant when compared with austenitic Cr-Ni stainless steels. The excellent low temperature notch impact properties of 9 wt% Ni steels are due to a fine grained structure of tough nickel-rich ferrite, devoid of embrittling carbide networks, a structure of the type produced on tempering martensite. Small amounts of stable austenite formed during tempering, indirectly improves the impact strength after conventional heat treatment by taking the carbides into solution in the austenite. Steels of this group are low in carbon (< 0.1 wt%), Si ranges from 0.15-0.3 wt%, Mn upto 1 wt%, and a very low impurity content. Aluminium is used to control the oxygen content. In some cases small additions of Mo (0.3 wt%) are used to make the steel less sensitive to temper embrittlement [33]. Table 2.1 gives composition and properties of the above three category of steels containing nickel [33].

3.5 wt% nickel steels for low temperature service						
	ASTM A336	ASTM A203	ASTM A334	SA 203	KLN 3A	KLN 3B
	All values in wt%					
C	0.35	0.23	0.19	0.1	0.17	0.17
Si	0.1-0.4	0.15-0.3	0.18-0.4	0.24	0.15-0.4	0.15-0.4
Mn	0.5-0.9	0.7-0.8	0.3-0.6	0.6	0.4-0.7	0.4-0.7
S	< 0.04	–	–	0.004	< 0.04	< 0.04
P	< 0.035	–	–	0.008	< 0.035	< 0.035
Ni	2.25-3	3.25-3.75	3.18-3.82	3.43	3.25-2.75	3.25-2.75
Cr	–	–	–	–	–	–
Mo	0.2-0.5–	–	–	–	–	–
YS / MPa	–	–	241	450	450	–
UTS / MPa	–	–	448	540	550	–
Toughness / J	–	–	–	–	–	–
5 wt% nickel steels for low cryogenic service						
	ASTM A352	CRIOSEI	5.5 wt% Ni	ASTM A645		
C	< 0.15	0.1	0.06	< 0.13		
Si	< 0.6	< 0.4	0.2	0.2-0.3		
Mn	0.5-0.8	0.5-1	0.9	0.3-0.6		
S	–	< 0.03	0.005	< 0.025		
P	–	< 0.025	0.006	< 0.025		
Ni	4-5	5.5-6.5	5.8	4.7-5.2		
Mo	< 0.25	0.3-0.6	0.17	0.2-0.35		
Cr	–	0.3-0.6	0.52	–		
YS / MPa	276	550	620	514		
UTS / MPa	483	700	770	676		
Toughness –190 °C / J	–	35	–	50		
9 wt% nickel steels						
	ASTM A553	ASTM A353	BS 1501	17 501	Vitkovice	VDEh680 X8Ni9
C	< 0.13	< 0.13	< 0.1	< 0.1	0.06-0.12	< 0.1
Si	0.15-0.3	0.15-0.3	0.1-0.3	0.15-0.35	0.1-0.35	0.1-0.35
Mn	< 0.9	< 0.9	0.3-0.8	0.3-0.8	0.3-0.8	0.3-0.8
S	< 0.04	< 0.04	< 0.03	< 0.03	< 0.025	< 0.035
P	< 0.035	< 0.035	< 0.025	< 0.025	< 0.025	< 0.035
Ni	8.5-9.5	8.5-9.5	9.75-9.75	8.5-10.5	8.5-10.5	8.5-9.5
Mo	–	–	–	–	0.4-0.6	–
YS / MPa	517	–	–	490	650	490
UTS / MPa	689	–	–	637	833	637
Toughness at - 196 °C / J	34	–	–	29	90	41

Table 2.1: Composition and mechanical properties of 3.5, 5.5 and 9 wt% nickel steels [33].

2.1.1 Austenite formation in nickel steels

The ferrite→austenite transformation occurs in Ni steels at relatively low temperatures particularly in alloys containing greater than 8 wt% nickel. The transformation behaviour of a low-carbon 9 wt% Ni steel is similar to that of a binary Fe-Ni alloy, with equilibrium achieved slowly. Thus, in tempered martensite, small quantities of a high-carbon Ni austenite regions are formed which remain stable even at liquid nitrogen temperatures. The austenite derives its enriched carbon content from the solution of carbides [33].

Some metallurgical aspects of 9 wt% Ni steels are summarised as follows [35]:

1. A high nickel content combined with appropriate heat treatment produces a fine microstructure of tempered martensite with finely distributed islands of austenite. This fine structure as well as the ferrite matrix with a high nickel content is the main reason for the excellent toughness.
2. The high nickel content lowers the Ac_1 temperature to the extent that austenite islands are formed during tempering. Unless the heat treatment is adjusted to make the austenite stable, it transforms to martensite at subzero temperatures or during deformation so that the toughness is impaired.

These features are summarised in Fig. 2.1. Characteristic notch toughness transition curves for the three types of nickel steels are presented in Fig. 2.2 [33].

2.1.2 Austenite precipitation

The three main hypotheses, which suggest that the lowering of DBTT occurs due to austenite precipitation are as follows [33]:

- *Austenite acting as a crack blunter*: this hypothesis assumes that a crack propagating through the steel would blunt in the ductile face-centered cubic austenite.

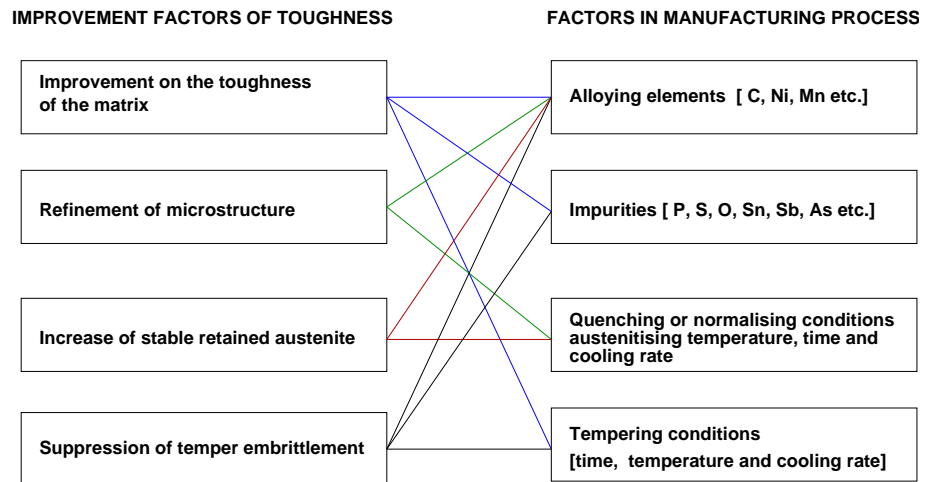


Figure 2.1: Factors affecting the toughness of the nickel-alloyed steels

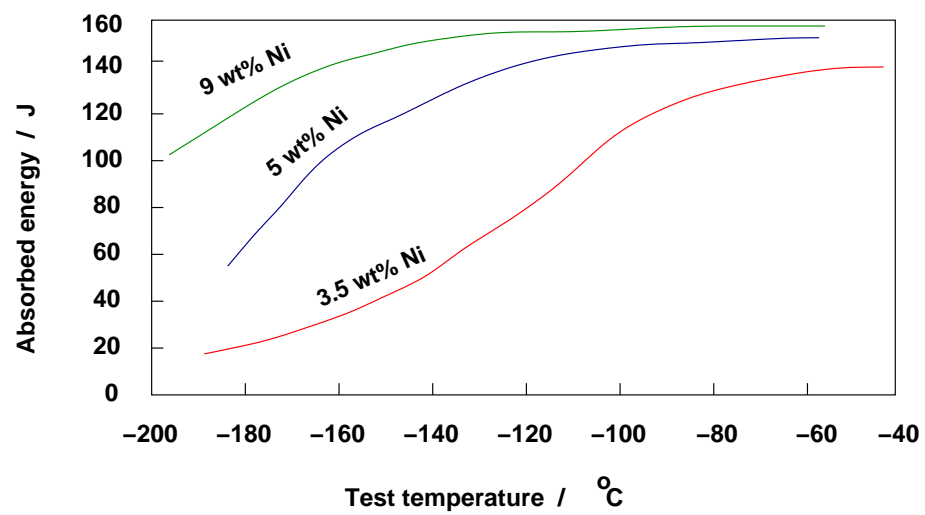


Figure 2.2: Characteristic Charpy notch toughness transition curves for the three types of Ni steels

- *Austenite as a scavenger*: the austenite acts as a sink for grain boundary pollutants, such as phosphorus and sulphur, so the toughness is increased by eliminating intergranular fracture.
- *Crystallographic cleavage impairment model*: the austenite transforms to a variant of martensite that relieves the strained region in front of the crack tip. The fracture surface would then consist of smaller facets due to the presence of the mechanically transformed austenite.

The influence of phosphorus on the intergranular fracture of ferritic steels at 77 K has been well documented by Darrel and Morris [36]. In a Fe-7.95Ni-1.93Mn-0.007Ti-0.003N-0.003P-0.003S-<0.001C wt% alloy with a martensitic microstructure they found intergranular fracture when tested at 77 K. Auger analysis revealed phosphorus at the prior austenite grain boundaries, at a concentration 60 times that in the bulk of the material. It was therefore concluded that phosphorus segregated to the grain boundaries during the austenitizing treatment to cause intergranular fracture. To avoid this a three stage heat treatment process was adopted. The material was austenitised at 900 °C for 2 h and then annealed at 750 °C for 1 h; both the cases followed by water quenching. Further an intercritical anneal at 660 °C for 1 h was performed followed by water quenching. This annealing treatment enabled formation of an unstable austenite, which was made stable by combining yet another intercritical annealing treatment (in the two-phase region) at 550 °C for 12 h. The alloy after these treatments when tested resulted in a transgranular fracture, which shows that austenite at the grain boundary scavenges the impurity elements like phosphorus and sulphur thus avoiding an intergranular fracture.

It is said that, alloy steels of type 9 wt% Ni can combine high strength levels (0.2% proof stress of 600 MPa) with superior notch toughness (Charpy V-notch values 35 J) even at -196 °C, but can do so only if their microstructure consists of fine-grained high-temperature tempered martensite, with no more than 10 vol.% of retained austenite [37].

Kim *et al.* [38] adopted a three step heat treatment process to improve the toughness of a 5.5 wt% nickel steel. The steel was austenised at 800 °C for 1 h. An intercritical anneal at 670 °C for 1 h was followed by an intercritical temper at 600 °C for 1 h. They claim to have lowered the ductile–brittle transition temperature by precipitating a thermally stable austenite along the martensite lath boundaries. There have been many other researchers who have associated the toughness improvement to the presence of retained austenite between the martensite lath boundaries [39–43].

Furukimi and Saito have studied the effects of phosphorus segregation to grain boundaries on the toughness of 9 wt% Ni steel welds [44]. It was concluded that toughness of this kind of steel increases with decrease in grain boundary segregation of phosphorus. Simulated weld joints showed that a concentration of phosphorus above 0.008 wt% decreased the Charpy toughness.

Thaulow conducted experiments on submerged–arc welded Fe–0.12C–11.5Mn wt% steels with a range of titanium concentrations [45]. A small amount of titanium in carbon–manganese steels is good for toughness since it decreased the fraction of proeutectoid ferrite. However, an increase in titanium concentration above 0.06 wt% led to decrease in toughness. This was attributed to the presence of titanium carbo–nitride inclusions. They did not observe any retained austenite in the steels studied [45].

Kim *et al.* studied the weld metal impact toughness of electron beam welded high nickel steels (9–16 wt%) and inferred that an increase in nickel concentration improved toughness from 25 J (9 wt% Ni) to 118 J (16 wt% Ni). This increase in toughness was attributed to the presence of high nickel martensite which could autotemper. It has also been noted that stable retained austenite is responsible for the improved toughness [46]. Though the toughness of low and high nickel welds were compared, no account was taken of the variations in strength. Further the theory of autotempering is not adequately supported since the weld with lower nickel having a higher M_s temperature would autotemper in the course of cooling [7].

Kim and Morris used a two-step heat-treatment process to refine the microstructure with the aim of improving the toughness of a ferritic weld [47]. The steel had a nickel concentration 12 wt% with 0.25 wt% of titanium and 0.003 wt% boron. The toughness achieved was 136 J at - 196 °C at a yield strength of 1000 MPa. When the nickel content was increased to 17 wt% the toughness decreased due to the retention of unstable austenite in the weldment. Boron is a strong surfactant in the boundaries of the weld metal. It also prevents intergranular separation [47].

Since the presence of oxides reduces toughness, Widgery recommended a low manganese to silicon ratio to obtain efficient deoxidation in welds [48]. The absence of silicon in 9 wt% nickel steel welds leads to porosity due to insufficient deoxidation. But silicon and manganese decrease the low temperature toughness of welded 9 wt% nickel [49]. Addition of titanium to the filler metal thus removes the necessity for manganese and silicon, titanium being a stronger deoxidiser [50].

The next section discusses specifically the influence of manganese and nickel on the strength and toughness of steel welds.

2.2 Nickel-Manganese Steel Welds

The previous section highlighted the importance of nickel in improving the toughness of steels. There have not been many studies in which both nickel and manganese concentrations are large. Manganese is often thought of as a substitute for nickel [51], so it did not seem necessary to add both in large concentrations.

Kang *et al.* attempted to develop welding consumables with better resistance to cold cracking [52]. Cold-cracking generally occurs at temperatures below about 200 °C and can be aided by the presence of hydrogen, stress and a brittle microstructure [53]. The compositions tried by Kang *et al.* included a variety of nickel and manganese contents

(table 2.2). The welds were made using SMA welding with a heat input of 1 kJ mm^{-1} . They observed that the hardness increased linearly with manganese and nickel concentration, which was attributed to solid-solution strengthening. Also varying nickel content influenced Charpy impact energy, the extent of which depended on manganese content. This is evident from Fig. 2.3.

Weld label	All elements in wt%							
	C	Mn	Si	P	S	Ni	N	O
W1	0.008	0.4	0.18	0.008	0.009	1.08	0.0037	0.1527
W2	0.005	0.52	0.27	0.009	0.01	3.85	0.0032	0.1223
W3	0.01	0.49	0.24	0.009	0.01	6.95	0.0031	0.1354
W4	0.02	1.76	0.43	0.021	0.008	2.88	0.0074	0.1260
W5	0.02	1.61	0.40	0.018	0.009	5.23	0.0057	0.1180
W6	0.02	1.61	0.40	0.018	0.009	7.45	0.0055	0.1150
W7	0.01	0.91	0.23	0.009	0.01	3.47	0.0037	0.1308

Table 2.2: Chemical compositions of weld metals used by Kang *et al.* [52].

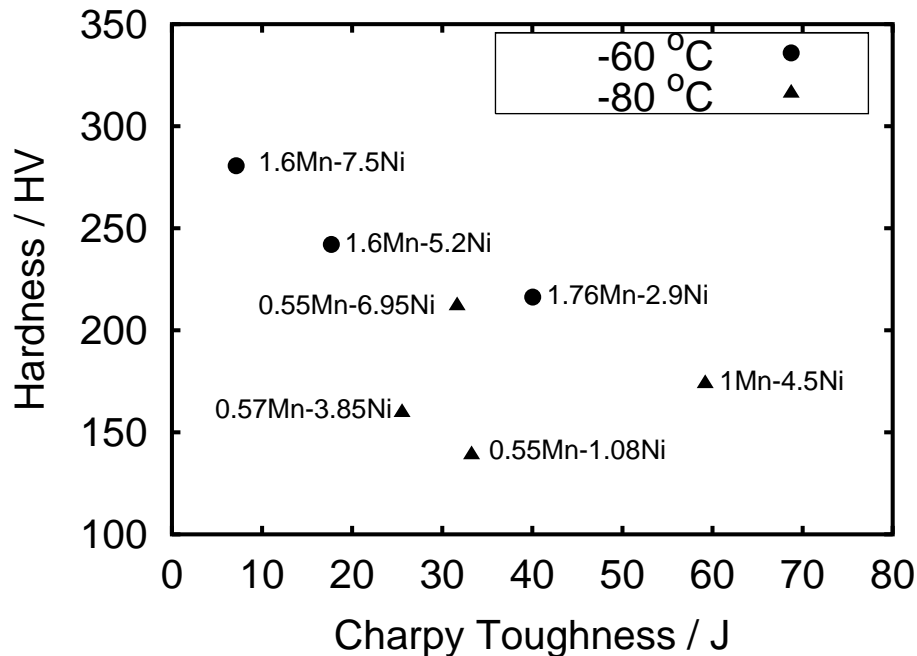


Figure 2.3: Influence of nickel and manganese content on Charpy toughness and hardness of low-carbon weld metals [52].

Hardness as a function of nickel concentration was found to follow the trend described as follows:

$$(1.6 \text{ wt\% Mn welds}) \text{ VHN} = 13 \times (\text{wt\% Ni}) + 177 \quad (2.1)$$

$$(0.5 \text{ wt\% Mn welds}) \text{ VHN} = 14 \times (\text{wt\% Ni}) + 111 \quad (2.2)$$

Increasing nickel concentration in the high manganese welds changed the solidification mode from ferritic to austenitic causing intergranular fracture. This was speculated to be due to segregation of impurity elements like phosphorus and sulphur to the prior austenitic grain boundaries. All other welds, fractured in a transgranular manner. Furthermore, the toughness improvement with increasing nickel concentration in the low manganese steel welds was due to refinement of columnar austenite grains. It was speculated that grain boundary embrittlement is made worse by simultaneous increases in the nickel and manganese concentration

In previous work done by Lord, six variants of a commercial weld electrode H1 (OK75.78) were studied [54], the compositions of which are presented in table 2.3. The welds were made using MMA welding at a heat input of 1 kJ mm^{-1} . The Charpy impact toughness, yield and ultimate-tensile strength values for these welds are presented in Fig. 2.4. The reasons behind the choice of the particular compositions are as follows:

1. Weld H1, has a high yield strength of 850 MPa and good toughness of 66 J at -60°C . The microstructure consists of bainitic ferrite.
2. H2 has a similar composition as H1, except for carbon. It has comparable toughness and strength. A concentration of 0.02 wt% carbon in H2 is expected to be retained in ferrite, hence avoiding the enrichment of residual austenite which may decompose to hard martensite.

Element / wt%	Weld						
	H1	H2	H3	H4	H5	H6	H7
Carbon	0.049	0.037	0.045	0.026	0.025	0.022	0.102
Manganese	2.09	2.13	1.11	0.97	0.85	0.78	2.18
Silicon	0.29	0.27	0.29	0.23	0.022	0.17	1.63
Phosphorus	0.005	0.010	0.008	0.010	0.010	0.010	0.009
Sulphur	0.012	0.006	0.006	0.010	0.009	0.011	0.005
Chromium	0.43	0.46	0.43	0.44	0.03	0.03	0.02
Nickel	3.04	3.03	3.91	4.00	3.91	4.25	2.07
Molybdenum	0.59	0.60	0.58	0.61	0.60	0.13	0.23
Vanadium	0.019	0.019	0.016	0.015	0.015	0.011	0.019
Copper	0.03	0.03	0.03	0.03	0.03	2.18	0.03
Titanium	0.014	0.014	0.014	0.012	0.012	0.010	0.039
Tin	0.007	0.010	0.007	0.004	0.002	0.001	0.010
Arsenic	0.012	0.012	0.012	0.006	0.005	0.000	0.013
Boron	0.0005	0.0006	0.0004	0.0002	0.0001	0.0000	0.0007
Oxygen	0.0267	0.0307	0.0310	0.0348	0.0299	0.0423	0.0205
Nitrogen	0.0118	0.0143	0.0101	0.0143	0.0148	0.0125	0.0113
Iron	bal.	bal.	bal.	bal.	bal.	bal.	bal.

Table 2.3: Compositions of the variants of OK75.78 electrode

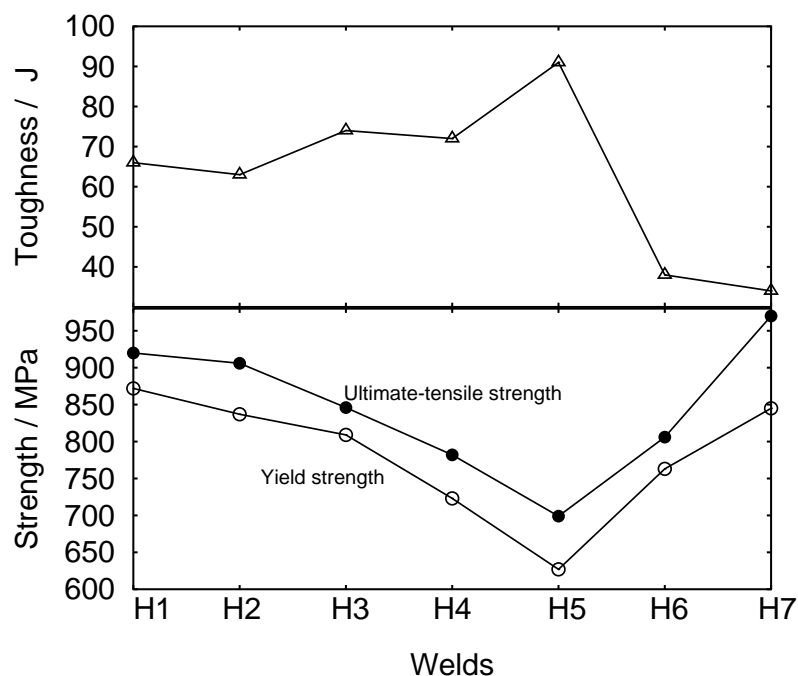


Figure 2.4: Charpy toughness at -60 °C, yield and ultimate-tensile strengths of the six variants of H1.

- H3 with lower manganese concentration than H1 and H2 but with higher nickel content, has a slightly improved toughness but the yield strength decreased. Increase

in nickel concentration was thought to improve the toughness.

4. A decrease in carbon concentration in H4 resulted in no change in toughness but reduced the yield strength further. The carbon concentration was relative to H3 for the reasons stated in (2).
5. With removal of chromium from H4 the toughness of H5 improved but at the expense of yield strength which is the lowest among all the variants.
6. H6 with 2 wt% copper has a higher yield strength than H5 but the toughness is very poor. This was attributed to the fact that weld H6 has a higher oxygen content (0.0423 wt.%) when compared with H5 (0.0299 wt.%). Oxide inclusions proliferate at large oxygen concentrations.
7. Among all the variants of H1, weld H7 with high carbon concentration and lower molybdenum content (0.2 wt%) has the highest yield strength, but poorest toughness. This is due to the formation of high carbon brittle martensite from the high carbon retained austenite under the influence of stress.

2.3 Summary

Morris states that “the trade-off between strength and toughness is a recurring theme in the metallurgy of high-strength steels” [55]. Many researchers have tried to improve the toughness of ferritic steels by adding nickel. Some have tried refining the grain size using heat treatment techniques for improving both toughness and strength. Yet others have stuck to the philosophy of maintaining retained austenite between martensite laths for optimising toughness and strength. But very few have tried to concentrate on improving the toughness and strength of a weldment, which is even more complex. Most of the work has been resorted to GTA welding for the sake of cleanliness of the weld.

Chapter 3

EXPERIMENTAL TECHNIQUES

3.1 Manufacture of Weld Metals

All the welds were fabricated using the manual metal arc (MMA) process from experimental electrodes produced to our composition specification at the ESAB AB Central Laboratories, Gothenburg, Sweden. As this work focuses upon the weld metal itself, a particular joint geometry (ISO 2560) was chosen to reduce the effects of dilution due to mixing with the base metal (Fig. 1.8). The welds were fabricated using 20 mm thick plates.

Three experimental welds designated A, B and C (described later) were fabricated. Weld A and B consisted of 22 beads using a heat input of 1.1 kJ mm^{-1} , whereas weld C contained 24 beads with a heat input of 1.0 kJ mm^{-1} . An interpass temperature of 250°C was specified. Battering of the plates was performed prior to welding, involving the deposition of a layer of weld beads along the edge of the plates.

3.2 Dilatometry using Thermecmator Z thermomechanical simulator

The *Thermecmator Z* (Fig. 3.1) allows the computer controlled application of heat treatments and deformation to a sample of material. Laser dilatometry is used to follow phase transformations as they occur, where the temperature is recorded using a Pt-PtRh thermocouple attached to the sample. The experiments are performed in a sealed chamber which is usually evacuated to allow efficient cooling of the specimen and to prevent oxidation. The specimen is seated centrally between Si_3N_4 platens. Heating is via a water-cooled induction coil surrounding the specimen. The maximum heating rate that can be achieved is around $50\text{ }^\circ\text{C s}^{-1}$ but this is dependent upon the material. Cooling is controlled using helium jets. The specimens are usually solid cylinders of length 12 mm and diameter 8 mm. For experiments in which rapid cooling is required, better results are achieved using hollowed out specimens with an internal diameter of 5 mm. A scanning laser beam is used to measure the diameter of the specimen during testing. A thermocouple is attached to the specimen using spot welding and, on placing the specimen in the machine, the thermocouple is located in order to prevent interference with the dilatometry measurements. Data from the dilatometer, the thermocouple and the load cell are logged simultaneously by a computer for later analysis.

3.3 Temperature Dependence of Hardness

In order to measure the hardness as a function of temperature below ambient, the weld metal sample was placed in a metallic container filled with liquid nitrogen (Fig. 3.2). The liquid nitrogen was allowed to evaporate and as the sample warmed up, hardness measurements were performed.

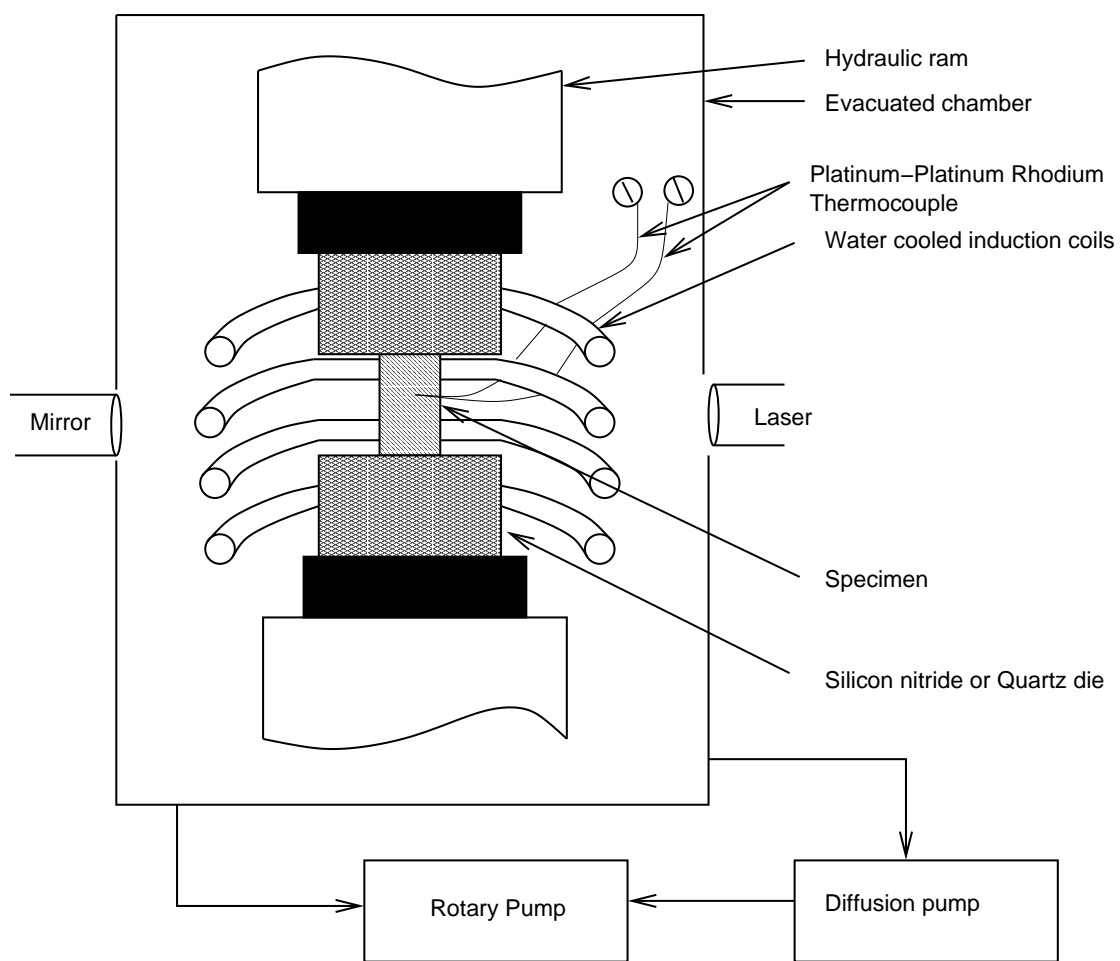


Figure 3.1: A schematic representation of thermomechanical simulator.

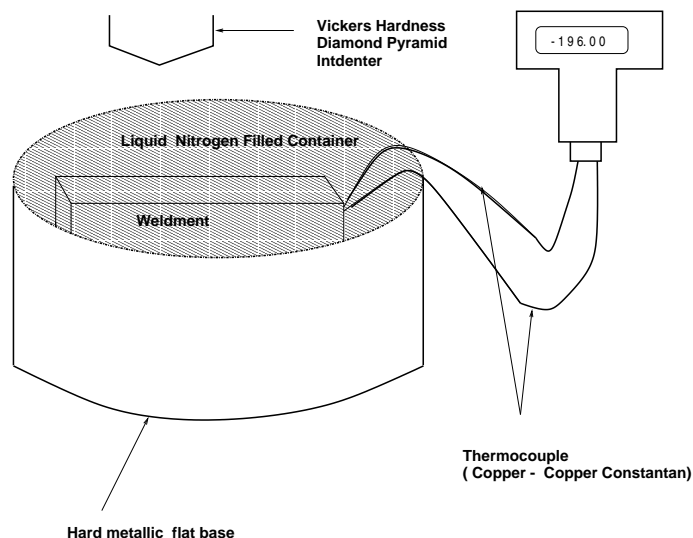


Figure 3.2: Experimental equipment for the measurement of hardness as a function of temperature.

3.4 Retained Austenite Measurement using X-ray Diffraction

The retained austenite content was measured using X-ray diffraction (Cu-K_α with wavelength, $\lambda : 1.5418 \text{ \AA}$). Metallographically polished samples were chemically etched to remove the deformed layer, and then step-scanned in a Phillips diffractometer over the 2θ range $47\text{-}130^\circ$. The step size being 0.03° with a dwell time of 30 s. The amount of specimen area illuminated by the X-ray beam depends on the divergence slit used. In the present case, a divergence slit of $\frac{1}{2}^\circ$ was used, giving an illumination of $(15 \pm 3) \times (3 \pm 1) \text{ mm}^2$ on the welds. The measurements were conducted in each case such that the weld centerline, along the cross-section, was illuminated, but it is not possible to comment on its exact location.

Assuming that there are only two phases, ferrite and austenite, the measured integrated intensities of austenite and ferrite can be used to calculate the retained austenite. Ratio of the intensities of austenite (γ) and ferrite (α) reflections is given by [56]:

$$\frac{I_{\gamma(hkl)}}{I_{\alpha(hkl)}} = \frac{R_{\gamma(hkl)}}{R_{\alpha(hkl)}} \times \frac{V_{\gamma}}{V_{\alpha}} \quad (3.1)$$

where $I_{\gamma(hkl)}$ is integrated intensity from a given (hkl) plane of austenite, $I_{\alpha(hkl)}$ is integrated intensity from a given (hkl) plane of ferrite, V_{γ} and V_{α} are the volume fractions of austenite and ferrite respectively. R_{γ} and R_{α} are given by following expression [56]:

$$R = \frac{1}{v^2} \times [|F|^2(p)(L_p)] e^{-2m} \quad (3.2)$$

where

- v is the volume of the unit cell,
- F is the structure factor which is proportional to the ratio of the amplitude of wave scattered by an atom to that scattered by an electron,
- p is the multiplicity factor which takes into account the number of equivalent planes that contribute to a reflection,
- e^{-2m} is the temperature factor and
- L_p is Lorentz–polarisation factor. Polarisation includes the effect of electron acceleration in different directions on the intensity of scattered beam at any point of consideration. The Lorentz factor includes the geometric factors that affect the intensity of the beam.

Considering that all materials in reality exhibit preferred–orientation to a greater or lesser extent, an average integrated intensity from three specific reflection of austenite and ferrite was used (table 3.1) [57].

Phase	Planes
Ferrite	(002), (112), (022)
Austenite	(002), (022), (113)

Table 3.1: Planes of ferrite and austenite whose integrated intensities were used in calculation of the amount of retained austenite.

$$\frac{I_{\gamma}}{R_{\gamma}} = \frac{1}{3} \sum_{i=1}^3 \frac{I_{\gamma,i}}{R_{\gamma,i}} \quad (3.3)$$

$$\frac{I_\alpha}{R_\alpha} = \frac{1}{3} \sum_{i=1}^3 \frac{I_{\alpha,i}}{R_{\alpha,i}} \quad (3.4)$$

In Eq. 3.1 V_γ/V_α can be found once the ratio of intensities, I_γ/I_α is calculated. Further, using the relation $V_\gamma + V_\alpha = 1$, the fraction of retained austenite can be calculated.

To make this simpler, a computer program using “C” was coded, documented and made available [58].

3.5 Mechanical Testing

All mechanical testing was done on samples machined from the weld metal itself. Cylindrical tensile specimens, 10 mm in diameter were machined along the weld direction. The specimens were degassed at 250 °C for 16 h prior to testing. Standard 10 mm × 10 mm Charpy V-notch specimens were machined such that the position of the notch lay within the weld metal and the axis of the specimen was normal to the welding direction. Both the Charpy and tensile specimens were machined from the center of the welds. Tensile specimens were machined as per ASTM standards (Fig. 3.3). The gauge length was approximated to $5.65 \times \sqrt{\text{Cross-sectional area}}$ to avoid size effects as is a standard practice.

3.6 Metallography

For optical metallography, the samples were etched using 2% nital. Scanning electron microscopy was also conducted on etched specimens using a Phillips XYZ20 microscope in the secondary electron mode.

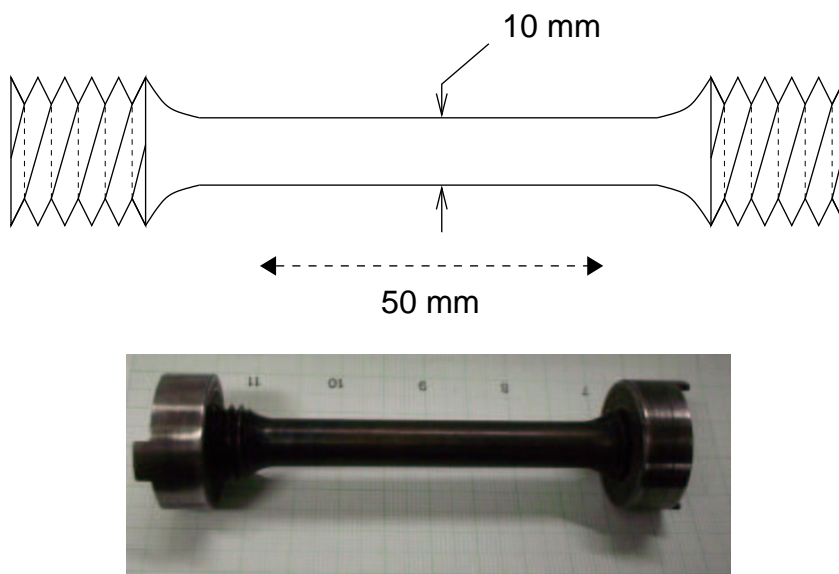


Figure 3.3: Tensile testing specimen made from all-weld metal

3.7 Transmission–Electron Microscopy

3.7.1 Thin-foil steel specimens

The starting sample usually is a piece of steel having a cross section much larger than can be analysed using a TEM. A thin cutting-disk was used to slice a 350 μm piece of metal with negligible surface deformation. It was then polished to 50 μm on both sides with a 1200 grit silicon carbide paper.

The foils were then electropolished using a twin-jet electropolisher with a solution of 5% perchloric acid, 85% ethanol and 10% glycerol. This electropolishing enables formation of a perforation (Fig. 3.4).

3.7.2 Carbon replicas

One method to avoid interference from the matrix during diffraction experiments on small precipitates is to extract the particles as a carbon replica. This also allows a larger field of view than would be possible with a thin foil. The procedure followed to

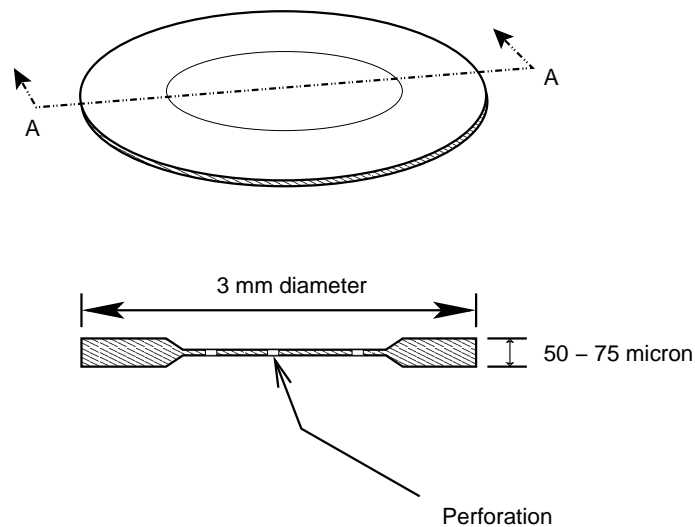


Figure 3.4: Schematic representation of a thin foil.

prepare the replicas from surfaces prepared using optical microscopy is shown in Fig. 3.5. Carbon from a sharpened graphite pencil was deposited in a vacuum of 10^{-5} torr on to the etched sample. The deposited carbon layer was then cut into 2 mm square pieces to enable removal of several small sections covering the whole area of the sample. The film was then detached from the sample by electrolytic etching in a solution of 5% hydrochloric acid in methanol at 1.5 volts. Each replica was washed in methanol and finally in distilled water. The floating replicas were then fished on to 400 square mesh copper grids for examination in the transmission electron microscope.

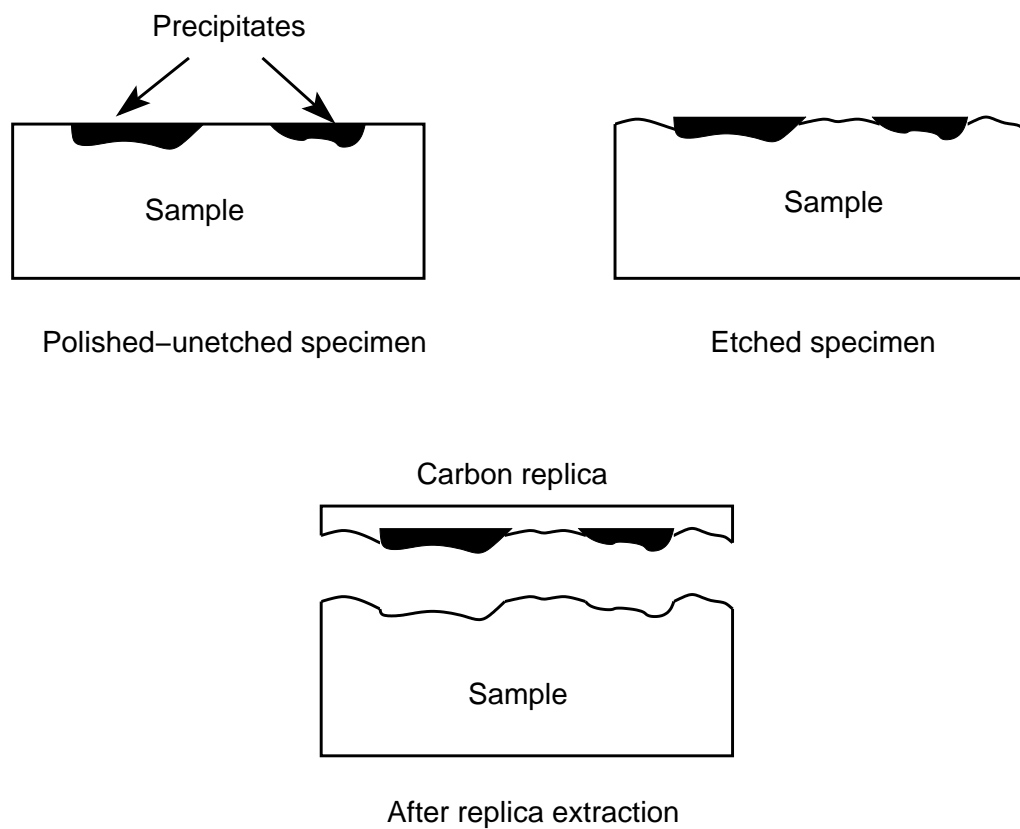


Figure 3.5: Schematic diagram illustrating preparation of carbon replicas.

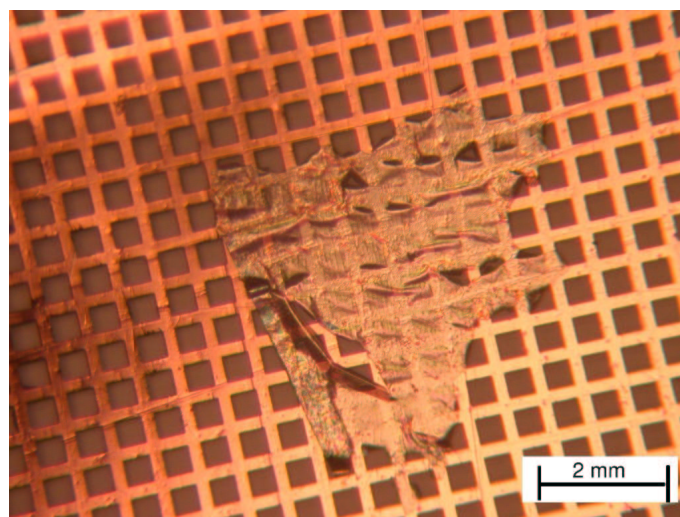


Figure 3.6: A carbon replica on a square mesh of copper grid.

Chapter 4

ARTIFICIAL NEURAL NETWORKS

Linear regression has been a widely used scientific tool for analysing experimental data in which a relationship as given by a best-fit is assumed between the inputs and the output. The general form of the equation developed using linear regression is a sum of the inputs x_i each of which is multiplied by a corresponding coefficient or weight w_i , and a constant, θ : $y = \sum_i x_i w_i + \theta$. Artificial neural networks are a more general method of regression analysis.

4.1 Basics of Neural Networks - An Overview

Similar to linear regression, the input variable x_i is multiplied by weight $w_{ij}^{(1)}$, but the sum of all these products form an argument of another transfer function, in this present work it is hyperbolic tangent as in Eq. 4.1. The final output is defined as linear function of hidden nodes and a constant, Eq. 4.2. Thus, the dependent variable y is given by Eq. 4.2.

$$h_i = \tanh \left(\sum_j w_{ij}^{(1)} x_j + \theta_i^{(1)} \right) \quad (4.1)$$

and

$$y = \sum_i w_i^{(2)} h_i + \theta^{(2)} \quad (4.2)$$

where x_j are the j variables on which the output y depends, w_i are the weights (coefficients) and θ_i are the biases (equivalent to the constants in linear regression analysis). The combination of Eq. 4.1 with a set of weights, biases, value of i and the minimum and maximum values of the input variables defines the network completely (Fig. 4.1).

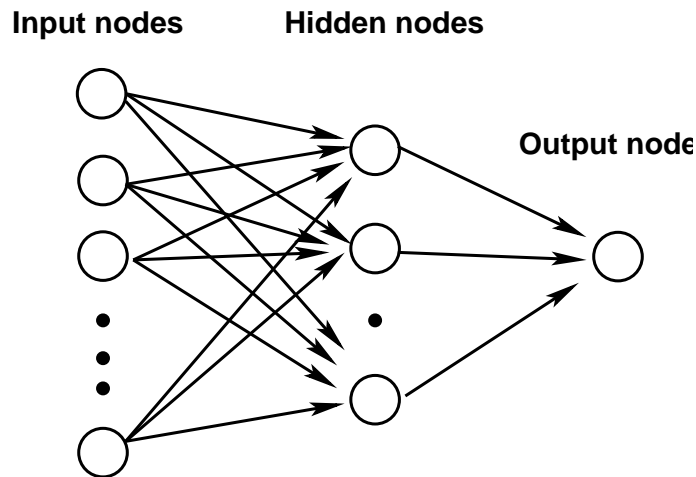


Figure 4.1: Schematic illustration of input, hidden and output layers of neural network model.

The flexibility of neural networks makes them able to discover more complex relationships in data than traditional statistical models which may assume a linear or pseudo-linear dependence of an “output” variable on the given set of “input” variables. Neural networks are able to implement more general (and more complex) non linear relationships. When the neural network is ‘trained’ on an empirical data, its parameters are adjusted so as to produce a non linear function which fits the data well. The flexibility of the non-linear function scales with the number of hidden nodes i . The complexity of the function is related to the number of hidden units. The strength of the hyperbolic tangent transfer function is determined by the weight w_j , the exact shape of which can be varied according to the availability of data in the input space. A model with one hidden unit (Fig. 4.2a) may not be sufficiently flexible to capture the information from the database, however non-linearity can be increased by combining several of the hyperbolic tangents as shown in Fig. 4.2b.

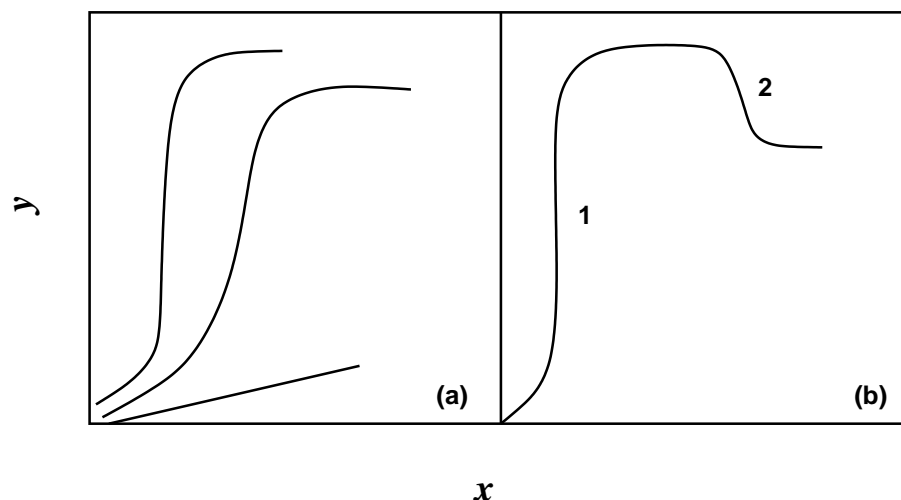


Figure 4.2: Hyperbolic tangent relation between inputs x and output y , a) three hyperbolic tangents with different weights b) combination of two hyperbolic tangent functions.

4.1.1 Training

Training involves the derivation of the weights and a specification of the functions which in combination with the weights relate the input to the output. The training process involves a search for optimum coefficients in the weight space to establish a non-linear relationship between the inputs and the outputs, and is computer intensive. Typically an 'objective function' or 'error function' is defined as a function of \mathbf{w}^1 to measure how well the network, with its weight set to \mathbf{w} , solves the task. The objective function is a sum of terms, one of each input/target pair $\{\mathbf{x}, t^2\}$, measuring how close the predicted output $y(\mathbf{x}; \mathbf{w})$ is to the target t . The training process is an exercise in *function minimisation*, – *i.e.*., finding \mathbf{w} that minimises the objective function. Once the network is trained, estimation of the outputs for any given inputs is very rapid.

The nature of the resulting function can be examined by making predictions and see how these depend on various combinations of inputs.

Because the neural network is able to implement more complex relationships than

¹Vectors are identified in the text using bold fonts

²Target experimental value the network uses for getting trained.

linear regression, it is also able to ‘overfit’ the training data; there is therefore a potential problem of obtaining a model that fits the training data well, but generalises poorly to test examples. To solve this problem, Bayesian regularisation theory can be used to control the complexity of the model [59, 60]. Using recently developed Bayesian neural network methods [59, 60], it is possible to automatically identify which of the many possibly relevant input variables are in fact important factors in the regression.

The network’s predictions are accompanied by error bars which depend on the specific position in input space. These quantify the model’s certainty about its predictions.

4.1.2 Error estimates

The overall error is estimated by comparing the predicted values of the output (y_j) against those measured (t_j):

$$E_D \propto \sum_j (t_j - y_j)^2 \quad (4.3)$$

E_D is expected to increase if important input variables have been excluded from the analysis. Whereas E_D gives an overall perceived level of noise in the output parameter, it is, on its own, an unsatisfying description of the uncertainties of prediction. MacKay has developed a particularly useful treatment of neural networks in a Bayesian framework [32], which allows the calculation of error bars representing the uncertainty in the fitting parameters. The method recognises that there are many functions which can be fitted or extrapolated into uncertain regions of the input space, without unduly compromising the fit in adjacent regions which are rich in accurate data. Instead of calculating a unique set of weights, a probability distribution of sets of weights is used to define the fitting uncertainty (as will be discussed in section 4.3). The error bars therefore become large when data are sparse or locally noisy (Fig. 4.3).

In this context, a very useful measure is the log predictive error (LPE) which gives the predictive performance of the test data or validation data. When compared with the

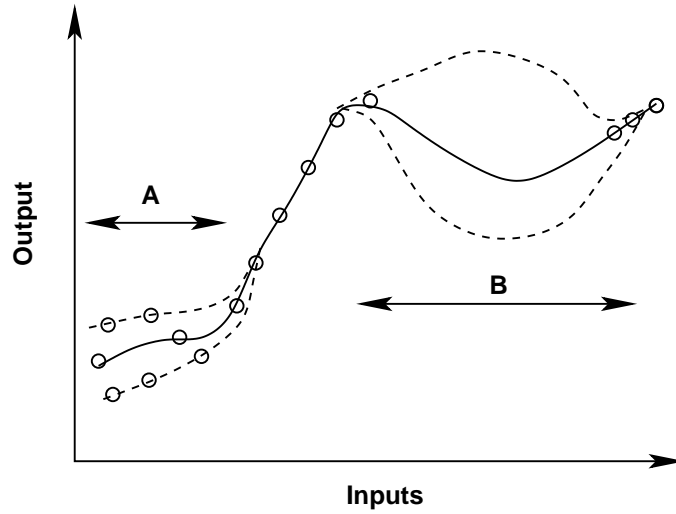


Figure 4.3: Schematic illustration of the uncertainty in defining a fitting function in regions where data are sparse (B) or where there is scatter (A). The dashed lines represent error bounds due to uncertainties in determining the weights.

test error, the penalty of making a wild prediction is much less, if the wild prediction is accompanied by appropriately large error bars (Eq. 4.4) [32].

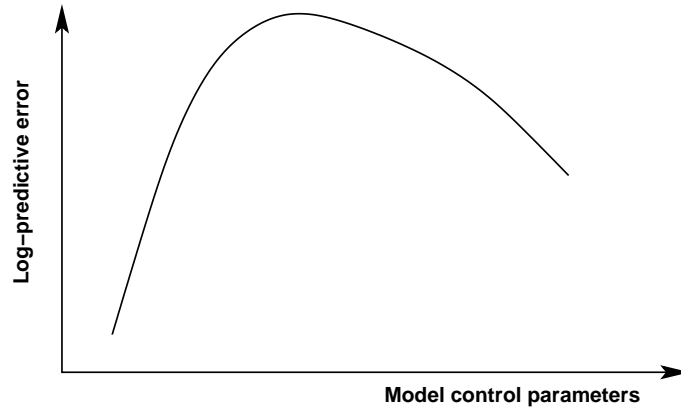
$$LPE = \sum_m \left[\frac{(t^{(m)} - y^{(m)})^2}{2(\sigma_y^{(m)})^2} + \log \left(\sqrt{2\pi\sigma_y^{(m)}} \right) \right] \quad (4.4)$$

where, $\sigma_y^{(m)}$ is the standard deviation of the output variable.

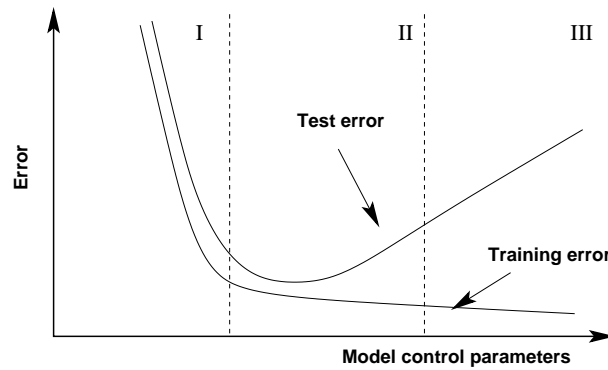
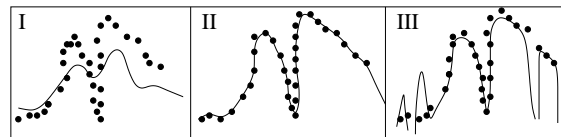
A model is better with a large log predictive error and low the test error (Fig. 4.4). The error bars presented throughout this work therefore represent a combination of the level of noise in the output and the fitting uncertainty as described above.

4.1.3 Overfitting

As specified earlier a potential difficulty with the use of powerful non-linear regression methods is the possibility of overfitting data. To avoid this, the experimental data can be divided into two sets, a *training* dataset and a *test* dataset. The model is at first produced using only training data. The test data are then used to check the way the



(a)



(b)

Figure 4.4: Ranking procedure of trained models with varying model complexity using a) Log-predictive error b) test error. The latter also shows the generalising capabilities of the models starting from left (simple) to right (complex)

model behaves when presented with previously unseen data. The training error tends to decrease continuously as the model complexity increases. The best model in this case is chosen on the basis of the test error, which is required to be minimum [61].

4.2 Best Model and Committee

A model is necessarily an approximation to the truth. In any real data analysis situation no single model will completely capture the true relationship between the inputs and outputs. Among a set of models, a *best model* is the one which most closely captures the true relationship for the particular purpose. But, the aim is to predict well as judged by minimising the squared error between the predictions and the actual outcome *i.e.*, minimisation of the test error, which can be better achieved by averaging over a set of specific models known as a *committee*.

4.3 Computation of Weights - Probabilistic Approach

The explanation presented in this section has been adapted from the references [59, 62–64]. For a continuous variable x , a Gaussian probability distribution is given by:

$$P\{x\} = \frac{1}{\sigma\sqrt{2\pi}} \exp \left[-\frac{(x - \bar{x})^2}{2\sigma^2} \right] \quad (4.5)$$

where σ is the standard deviation or the width of the Gaussian, \bar{x} is the mean and the term outside of the exponential normalises the distribution such that the area under the curve (*i.e.* total probability) is unity.

The aim of the Bayesian inference is to find a distribution of weights (fitting parameters) given data. The method is general but for simplicity is illustrated using a straight line model as shown in Fig. 4.5, which conforms to the equation:

$$y = w_1 x_1 + w_2 x_2 \quad (4.6)$$

where w_1 is the slope and w_2 the constant when x_2 is set to 1. Let the vector describing the set of weights (w_1, w_2) be \mathbf{w} . Now all these prior beliefs can be expressed as a Gaussian

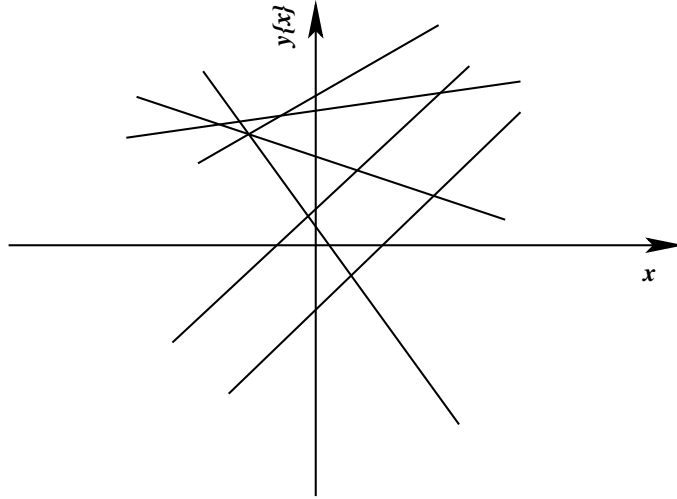


Figure 4.5: Prior beliefs about straight line models

distribution function as:

$$P(w_i) = \exp(-\alpha w_i^2/2)/Z \quad (4.7)$$

where Z is the normalising factor and $\alpha = 1/\sigma_w^2$ (σ_w is the standard deviation in the distribution of w_i).

Suppose there are some experimental data $D = \{\mathbf{x}_m, t_m\}$, where $m = 1 \dots N$ is a label running over the pairs of inputs \mathbf{x}_m and target t_m .

Given the data, a line with connections \mathbf{w} can make predictions about the target output t_m as a function of the input vector $\mathbf{x}_m = (x_1, x_2)_m$ in accordance with the probability distribution

$$P(t_m | \mathbf{w}, \mathbf{x}_m) = \frac{1}{Z'} \exp \left[-\frac{\beta(t_m - y(\mathbf{x}_m; \mathbf{w}))^2}{2} \right] \quad (4.8)$$

with $\sigma_\nu^2 = 1/\beta$, where σ_ν is the perceived noise in the output (Fig. 4.6).

As per Bayes theorem, the desired probability distribution of weights is given by the *likelihood* times the *prior* beliefs:

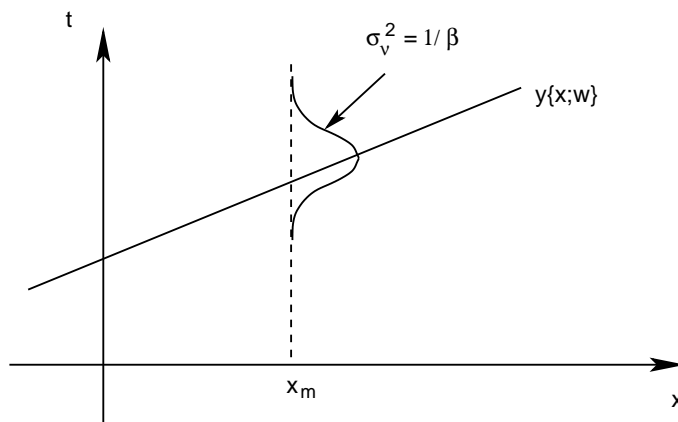


Figure 4.6: Gaussian noise associated with the output

$$P(\mathbf{w} \mid \{t\}, \{x\}) \propto P(\{t\} \mid \mathbf{w}, \{x\}) \times P(\mathbf{w}) \quad (4.9)$$

$$= \frac{P(\{t\} \mid \mathbf{w}, \{x\}) \times P(\mathbf{w})}{P(\{t\} \mid \{x\})} \quad (4.10)$$

$$= \frac{\exp\{-M\{\mathbf{x}\}\}}{Z_M} \quad (4.11)$$

Where

$$M\{\mathbf{x}\} = \frac{\alpha}{2} \sum_i w_i^2 + \frac{\beta}{2} \sum_{m=1}^N \left(t_m - \sum_i w_i x_{m,i} \right)^2$$

$\{x\}$ and $\{t\}$ are the set of inputs and targets respectively of the whole database.

4.4 Model Development Procedure

The experimental data collected are stored in a particular format and normalised as:

$$x_N = \frac{x - x_{min}}{x_{max} - x_{min}} - 0.5 \quad (4.12)$$

where x is the original value from the database, x_{max} and x_{min} are the respective maximum and minimum of each variable in the original data and x_N is the normalised value. Though

the normalisation of data is not necessary for the development of models, it helps in comparing the relative influence of different input variables. Around 80 different models with varying hidden units and seeds (to generate random starting weights) are selected for training over chosen functions (Eqs 4.3 & 4.1). Before training, the database is randomised in order to divide the information into test and training datasets in a fair manner. One of the datasets are used for training while the other for testing how the trained models behave with unseen data.

For a trained model the overall error E_D is the sum of squared error between the desired output (target) t and calculated output y as given in Eq. 4.3. A committee is formed which consists of models that have contributed to the minimisation of the overall test error. The committee prediction is the average value of individual model predictions.

Without changing the complexity of individual models, the committee is retrained on the whole database. During retraining the weights are adjusted to fit the whole database better. Once the retraining operation is completed, the models are ready for use.

Chapter 5

RESULTS AND DISCUSSION

Based on an existing commercial alloy, (table 2.3) Lord [54] performed a variety of experiments on six different weld compositions, with varying carbon, nickel and copper concentrations. None of these succeeded in achieving better combinations of strength and toughness relative to the original commercial alloy. The research presented here is a continuation of the work by Lord, with the aim of achieving better than the commercially available alloy.

Dislocations in ferrite can be thought of as being three-dimensionally dissociated (Fig. 5.1) [4, 34], making glide difficult. The yield strength is therefore particularly temperature sensitive, leading to ductile-brittle transition when cleavage becomes easier than plastic flow. Nickel is known to increase the stacking fault energy [4], making flow easy, thus preventing cleavage.

With this in mind, the nickel concentration of the commercial alloy H1 was empirically increased to 7 and 9 wt% (welds A and B respectively) at the beginning of this project. The electrodes and the welds were manufactured as described in chapter 3. Mechanical tests were performed on all-weld specimens of weld A and B.

The yield and ultimate-tensile strengths increased due to the nickel additions but unfortunately, this was at the expense of toughness (table 5.1). A different approach was therefore sought.

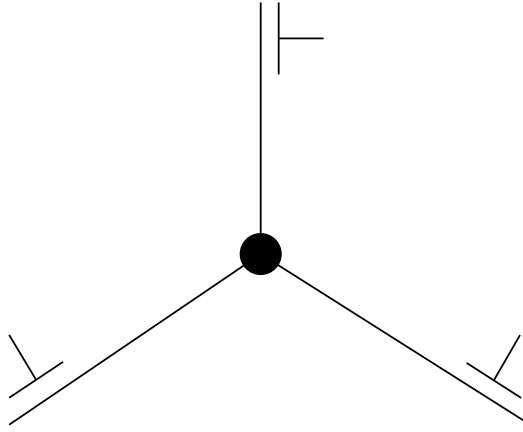


Figure 5.1: Schematic diagram of three-dimensional dissociation of dislocations in ferrite.

	Weld A	Weld B	Weld C
Yield strength (YS) / MPa	789	841	725
Ultimate tensile strength (UTS) / MPa	1009	1055	822
Elongation / %	14.8	14	21.4
YS/UTS	0.78	0.80	0.87
Charpy toughness at -60 °C / J	15	10	101

Table 5.1: Mechanical properties of welds A, B and C

5.1 Artificial Neural–Network

Artificial neural network (ANN) models for the yield and ultimate tensile strength, toughness and elongation, were created from an experimental database representing 3300 ferritic welds, which included experimental results from the new 7 wt% and 9 wt% nickel welds. The vast majority of the data were from the published literature. The description of the method itself can be found in chapter 4 and elsewhere [32, 59, 60]. The database consisted of information from multi-run weld deposits designed for low-dilution to enable specifically the study of all-weld metal properties from electric arc welds made using one of the following processes: manual metal arc (MMA), submerged arc (SAW) and tungsten inert gas arc (TIG). The spread of the data is as shown in Figs 9.1 & 9.2 (Appendix I), which indicate that carbon, manganese, nickel, oxygen, interpass temperature and

heat input are uniformly represented, although it must be emphasised that each graph represents only one variable.

The base set of input variables (table 9.1, Appendix I) for the network consisted of chemical composition, welding parameters, heat treatment and the temperature at which the Charpy toughness tests were conducted.

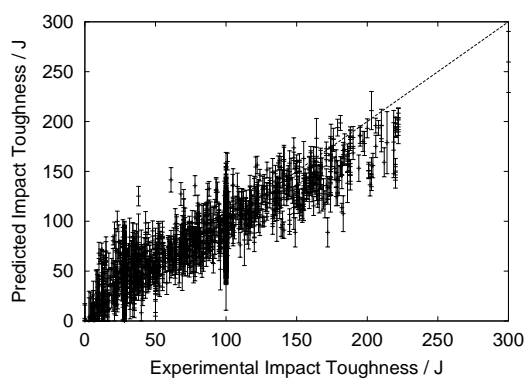
Oxygen was an input variable for the toughness, ultimate tensile strength and elongation models since the inclusion content has an effect on all these properties, but not on yield strength. Excluding oxygen from the yield strength analysis also permitted the use of a larger set of data.

Fig. 7.7 illustrates the overall behaviour of each of the committee of models (chapter 4). The error bars illustrated represent the $\pm 1\sigma$ uncertainties in the predictions; a further contribution to the error comes from noise, which is not illustrated. The maximum perceived noise in the toughness, yield strength, ultimate tensile strength and elongation was ± 0.0833 , 0.04024 , 0.0232 and 0.0638 respectively, when each output is normalised from 0 to 1. The models used are freely available on [65].

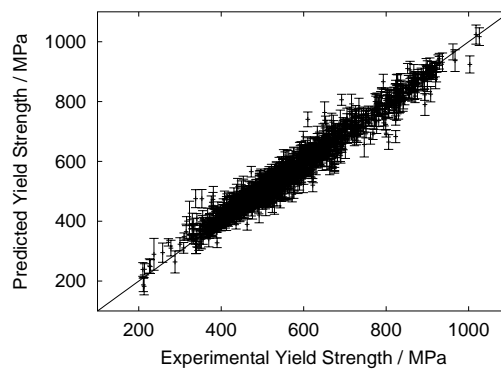
5.2 An Optimum Composition

It is widely believed in the welding industry that nickel is a panacea for improving the toughness of welds. On the other hand, these perceptions are generally based on a limited set of observations. A neural network is probably the best way of studying trends in an objective manner given the complexity of the problem. The toughness was therefore estimated as a function of nickel and manganese concentrations with the other variables controlled as in table 5.2, since the interest here is in high strength welds.

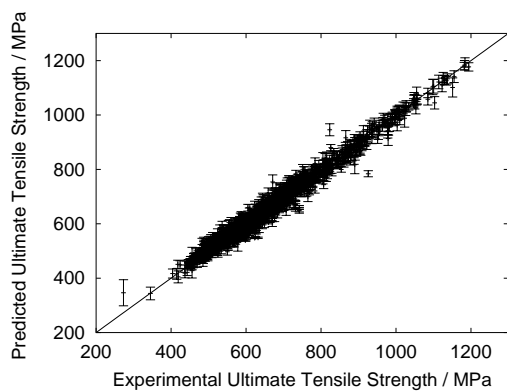
The results (Fig. 5.3) revealed a remarkable trend, that for the system studied, nickel only leads to an improvement in toughness when the manganese concentration is small.



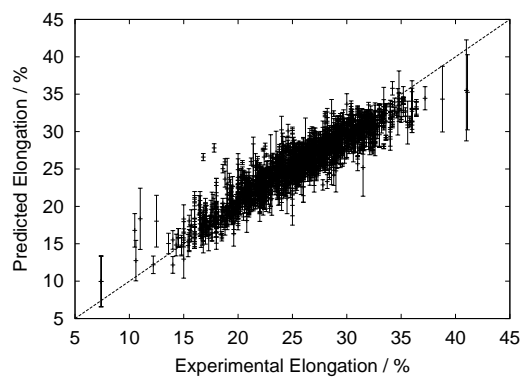
(a) Toughness model



(b) Yield strength model



(c) Ultimate tensile strength model



(d) Elongation model

Figure 5.2: Predictions made using the committee of models.

C	Si	Mn	S	P	Ni	Cr	Mo
0.034	0.25	0.2	0.008	0.01	0-12	0.5	0.62
V	Cu	Co	W	O / ppm	Ti / ppm	N / ppm	B / ppm
0.011	0.04	0.009	0.005	380	80	250	1
Nb / ppm	HI / kJ mm ⁻¹	IT / °C	pwhtT / °C	pwhttt / h			
10	1	250	250	16			

Table 5.2: Base variables used for analysing the effects of nickel and manganese concentrations. All elements are in wt% unless otherwise specified. HI - Heat Input; IT - Interpass Temperature; pwhtT - Post Weld Heat Treatment Temperature; pwhttt - Post Weld Heat Treatment Time.

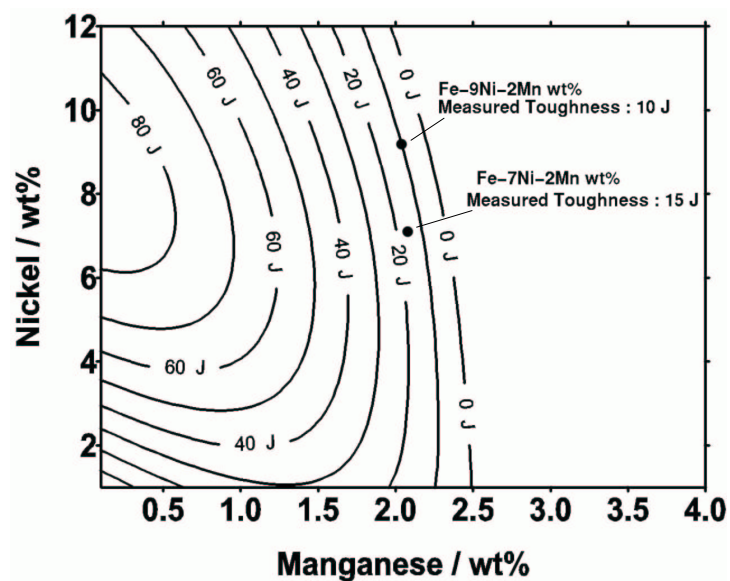
It is otherwise detrimental to toughness.

Following this analysis, a new experimental weld with a manganese concentration below 0.7 wt% (weld C) was manufactured (table 5.3).

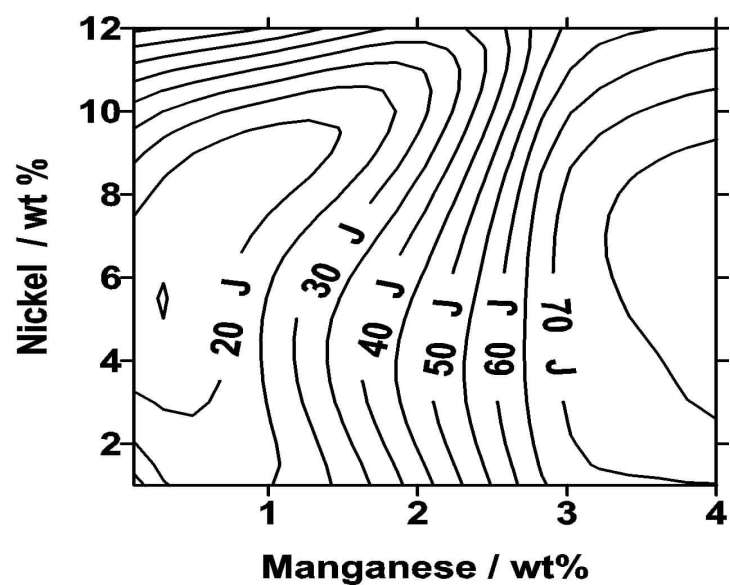
C	Si	Mn	S	P	Ni	Cr	Mo
0.025	0.65	0.37	0.006	0.013	6.6	0.21	0.4
V	Cu	Co	W	O / ppm	Ti / ppm	N / ppm	B / ppm
0.011	0.03	0.009	0.005	380	80	180	1
Nb / ppm	HI / kJ mm ⁻¹	IT / °C	pwhtT / °C	pwhttt / h			
10	1	250	250	16			

Table 5.3: Manufactured composition of experimental weld C measured using optical emission spectrometry and Leco combustion equipment.

The actual composition of weld C (as opposed to its design settings) was analysed using the ANN model and the results are illustrated in Fig. 5.4. They show that increasing the nickel beyond 8 wt% should not be beneficial for toughness. Furthermore, increasing the carbon concentration in excess of 0.03 wt% is deleterious to toughness (Fig. 5.4c). Chromium and molybdenum have little effect on toughness. The essential outcome of the analysis is that the composition of weld C, as given in table 5.3, is in fact optimum. Even the trace elements are well-controlled. Heat input and interpass temperature do have significant effects because they determine the weld cooling rate. A higher cooling rate, lower heat input or lower interpass temperature reduces the toughness because they lead



(a)



(b)

Figure 5.3: Effect of manganese and nickel concentrations on toughness, as predicted using the neural network models. (a) Predictions. (b) $\pm 1\sigma$ uncertainty in prediction.

to an increase in strength (Figs 5.5d, 5.5e). It is exciting that these results were predicted and that no new experimental programme was necessary before the manufacture of weld C. We now proceed to examine possible reasons for the nickel–manganese effect.

5.3 Toughness Improvement - Contribution due to Metallurgical factors

As already discussed Charpy toughness experiments on three welds A (7Ni-2Mn wt%), B(9Ni-2Mn wt%) and C (7Ni-0.5Mn wt%) revealed the huge increase in toughness due to reduction in manganese concentrations (Fig. 5.6). The three alloys all had high nickel concentrations, the critical difference being the concentration of manganese. But, how does this difference of 1.5 wt% manganese between weld C and weld A/B produce such a huge variation in toughness? The next few sub-sections deal with various studies made to find the mechanism.

5.3.1 Temperature dependence of hardness

Toughness data should strictly be compared at constant strength. Unfortunately, tensile tests are usually conducted at ambient temperature whereas Charpy data are of greatest interest at sub-zero temperatures. The temperature dependence of the flow stress for welds A and C was thus studied by measuring the hardness as a function of temperature in the hope that the toughness of the two welds could be compared at constant hardness. However, as shown in Fig. 5.7, the hardness curves are almost horizontal as a function of temperature and sufficiently apart to prevent such a comparison.

However, a limited account can be taken of the influence of strength by comparing the Charpy toughness at -60 °C against welds H1–H7 (compositions listed in chapter 2), A, B and C. Fig. 5.8 shows that welds A and B, in spite of their high nickel concentrations, have very poor toughness when compared with welds H1 and H3 respectively which match

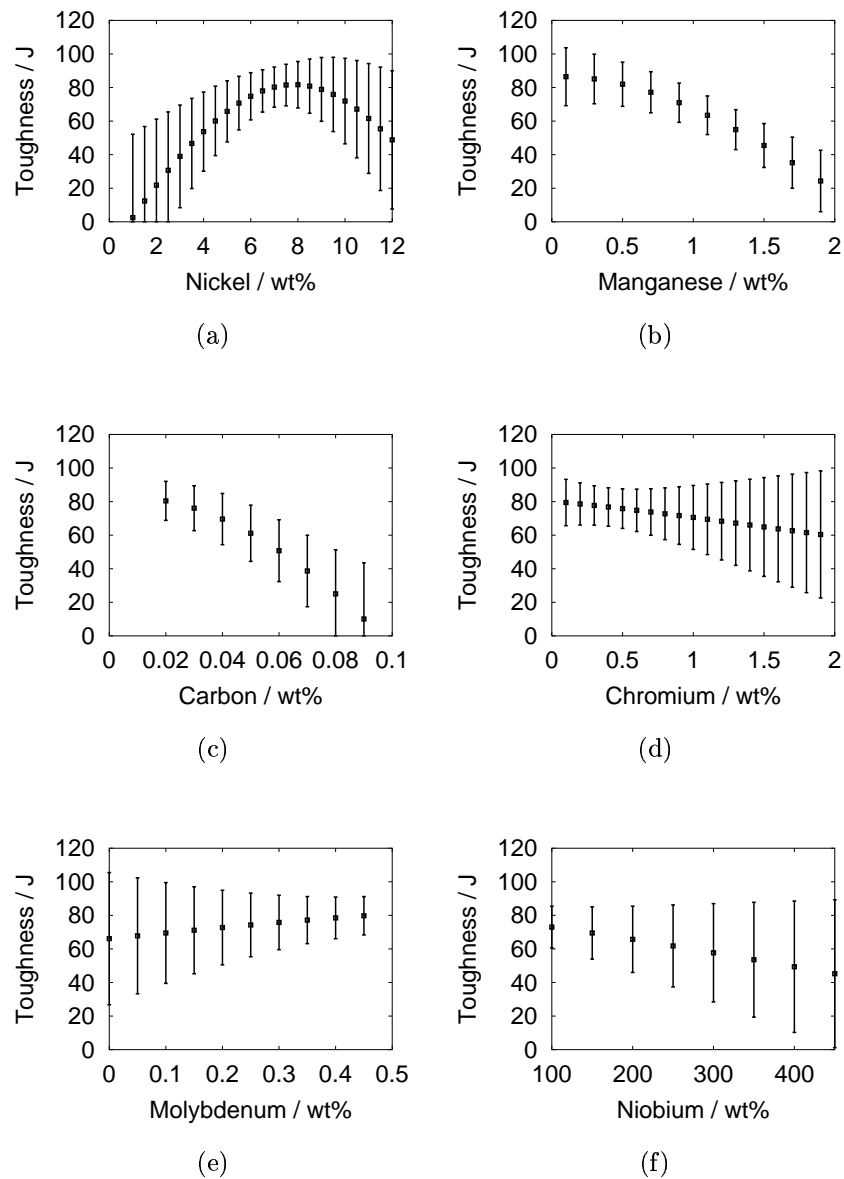


Figure 5.4: Effect of variation in concentration of alloying elements and heat input on toughness of weld C at a test temperature of - 60 °C.

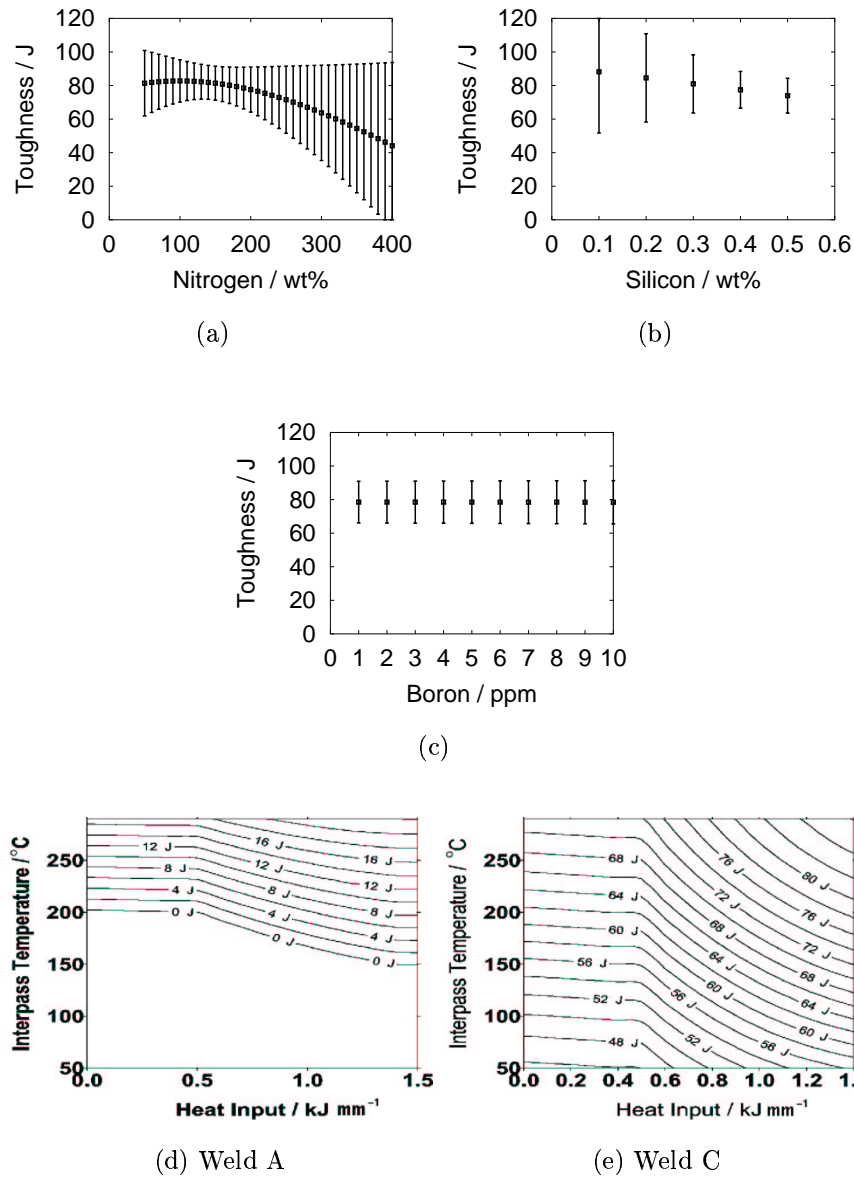


Figure 5.5: Effect of variation in concentration of alloying elements on toughness of weld C at a test temperature of - 60 °C.

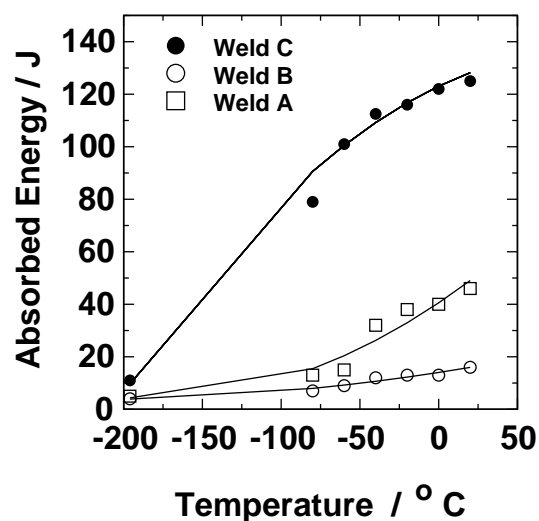


Figure 5.6: Effect of temperature on the absorbed energy of welds A, B and C during Charpy impact test.

in terms of strength. On the other hand, weld C is better than H4 which has identical strength. This reinforces the conclusion that weld C has exceptionally good toughness.

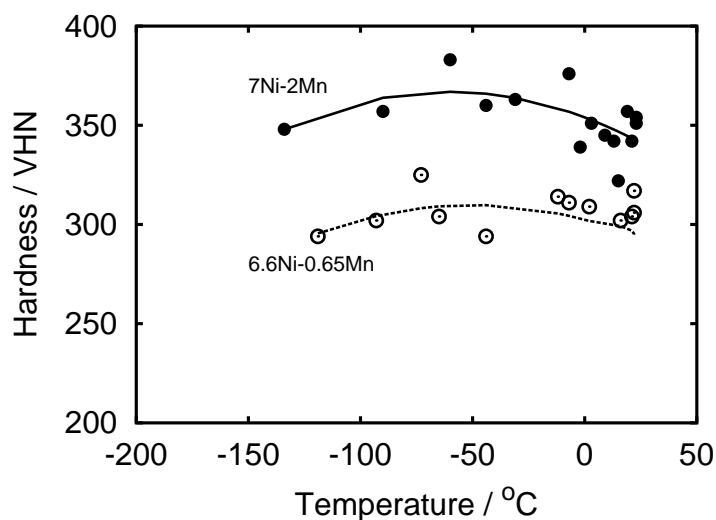


Figure 5.7: Temperature dependence of hardness.

5.3.2 Retained austenite measurements

Retained austenite measurements were performed using X-ray diffraction as described in section 3.4. The austenite and ferrite peaks used are shown in Fig. 5.9. Re-

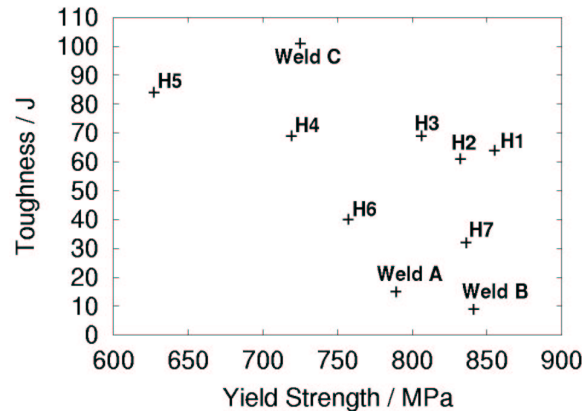


Figure 5.8: Charpy toughness measured at -60°C against the yield strength.

tained austenite can in principle improve the toughness by the crack blunting effect [33]. However, the differences between the three welds (table 5.4) are unlikely to be sufficient to explain the large variations in toughness.

Material	Retained austenite / volume %	Error/ %
Weld A	1.5	0.1
Weld B	0.8	0.1
Weld C	2.2	0.1

Table 5.4: Retained austenite content as measured using X-ray diffraction technique. More information can be found in chapter 3.

5.3.3 Effect of alloying on Ac_1 and uniformity of microstructure

The variation in hardness of a multipass weld is expected to depend on its Ac_1 temperature; this variation is on two scales, first because the deposition of a bead causes heat treatment of the underlying layer, and secondly a coarser effect because of tempering by the repeated deposition of layers [66]. The scatter in strength/hardness of multipass welds is expected to depend on its Ac_1 temperature. This is because in a multipass weld, an increase in Ac_1 also increases the section of the material which is tempered. The severity of tempering also increases with Ac_1 [66].

With high Ac_1 , in a multipass weld, a portion of the previous pass tempers whereas for lower Ac_1 alloys the previous pass largely reaustenises and transforms back to hard microstructures on cooling (Fig. 5.10). Higher concentrations of austenite stabilising elements lead to a decrease in the Ac_1 temperature.

Dilatometric experiments were used to measure the Ac_1 temperature of each weld in which the sample was austenitised at 1000 °C for 10 min using a heating rate of 10 °C s⁻¹. This revealed that weld A with the higher alloy content has a lower Ac_1 temperature \approx 650 °C (Fig. 5.11a), whereas for weld C, $Ac_1 \approx$ 680 °C (Fig. 5.11b). Although the difference in Ac_1 temperatures is only 30°C, it is consistent with the fact that the *variation* in hardness is greater in weld C, when measured on the weld centerline on a cross-section of the weld (Fig. 5.12).

Fig. 5.11 also shows two effects which are reproducible but whose consequences are not yet understood. The temperature range over which austenite forms is greater for weld C. Also the total dilatation for weld A is almost twice that for weld C during austenite formation.

5.3.4 Strain hardening versus toughness

When an alloy is stressed beyond its yield strength, it undergoes plastic deformation. The stress to produce continued plastic deformation increases with increasing plastic strain *i.e.*, the alloy strain hardens. The volume of the specimen remains constant during plastic deformation, and as the specimen elongates, it decreases uniformly along the gauge length in cross-sectional area. Initially the strain hardening more than compensates for this decrease in area and the engineering stress continues to rise with increasing strain. Eventually a point is reached where the decrease in cross-sectional area is greater than the increase in deformation load arising from strain hardening [4]. The strength of the alloy at this point is called the ultimate-tensile strength, since this is the maximum stress the material can withstand before necking down. A material that strain hardens more is

likely to have a higher ultimate-tensile strength. The ratio of yield to ultimate-tensile strength gives an approximate measure of strain hardening in the alloy. If the ratio is large, then strain-hardening is less and vice versa.

Comparison of this ratio for welds A and C show that the latter has less strain hardening (0.88) than weld A (0.78).

Manganese is known to contribute to a larger strain hardening coefficient in steels [34, 67]. There is no sufficient evidence in the literature as to how toughness is affected by the strain hardening coefficient.

Comparison of the toughness of a series of alloys having similar strain hardening effects showed that strain-hardening behaviour does not completely explain the change in toughness (Fig. 5.13).

5.3.5 Hardness maps and microstructure

To better characterise the uniformity of mechanical properties a facility for automated hardness mapping was used, at the U. S. Navy Laboratories in Washington. The tests were carried out on the author's behalf by D. Moon.

The Vickers microhardness tests were conducted with a load of 1 kg maintaining a distance of 0.5 mm between successive indentations. The hardness maps reveal that welds H1 and C have lower overall hardness whereas weld A has higher uniform hardness throughout the weld (Fig. 5.14, 5.15 & 5.16). This is expected since weld A has higher hardenability and in addition also has a lower Ac_1 temperature.

The time taken for the weld to cool from 800 °C to 500 °C was measured to be 10 s, which gives a cooling rate of 30 °C/s. The measurement was done at ESAB AB, Sweden by Enda Keehan at the author's request. The temperatures between 800 and 500 °C are important since many of the transformations during cooling from austenite take place in this temperature range. At this measured cooling rate, the transformation products of welds A and C are martensitic as can be seen from the calculated Time Temperature

transformation (TTT) diagrams [68] shown in Fig. 5.17.

Analysis of hardness data revealed that 40% of weld A has hardness greater than 350 VHN, whereas weld C has hardness less than 350 VHN throughout its microstructure, as can also be seen from the plots showing the percentage distribution of hardness in the welds (Fig. 5.18). Weld H1 does have regions with hardness greater than 350 VHN, but as seen in Fig. 5.14, these regions lie in the top layer which is not accessed in mechanical property measurements. Charpy and tensile specimens are machined from the center of the weld. Hence these hard zones on the top bead do not affect the results from Charpy impact tests.

Furthermore weld A has localised regions that are as hard or even harder than 360 VHN. These regions are probably due to the formation of fresh martensite after having reaustenitised by the heat from successive beads.

5.3.6 Segregation

Solute segregation occurs when an alloy cools from liquid to solid. A calculation using the Schiel theory (explained in section 1.5.1) for welds H1, A and C is shown in Fig. 5.19. The calculation was done using MTDATA [69]. For an alloy composition consisting of Fe, Cr, Mo and Mn the amount of elemental segregation to liquid phase was calculated by allowing FCC_A1(austenite), BCC_A2 (ferrite) and liquid to exist. The temperature was stepped from 950–1550 °C in intervals of 1 °C .

All three welds are sensitive to the segregation of nickel, but welds H1 and A show considerable manganese segregation. However, the extent of segregation is less in H1 due to the lower nickel concentration (≈ 3 wt%) unlike weld A where the nickel concentration is large (≈ 7 wt%). In weld C, the main segregate is nickel.

However, this does not explain the overall increase in hardness of weld A as discussed in section 5.3.5. Considering the scale of segregation and the region over which hardness is measured, it does not make sense to correlate microsegregation to the observed variations

in hardness. But the study is useful in indicating solute partitioning during solidification. Consistent with the calculations, the optical micrographs in Figs 5.20 & 5.21 reveal the effect of segregation on the microstructure of weld A in the form of banding, whereas the other two welds do not show any effect of the microsegregation on microstructure though.

Weld H1 solidifies as δ -ferrite, whereas welds A and C solidify as austenite. In principle, an alloy solidifying as austenite should exhibit an intergranular fracture during a Charpy impact test due to segregation of impurity elements like sulphur and phosphorus to the grain boundaries [52]. But, the specimens of weld A and C fractured during Charpy impact test at -60°C , analysed under a scanning electron microscope as shown in Fig. 5.22 do not reveal intergranular cleavage. Instead weld A shows quasi-cleavage and weld C shows a ductile fracture. This shows that the impurity elements were under control during the manufacture of the welds.

5.4 Strengths of Heat-Treated Welds A and C

Welds A and C have different yield and ultimate-tensile strengths. The reasons for weld C having a lower yield strength is that many of the weld portions are tempered to give a softer phase during multipass welding, whereas the lower Ac_1 of weld A reduces the tempering tendency. If this explanation for the lower strength of weld C holds true, then a tensile specimen of both welds A and C austenitised and quenched to give fresh untempered martensite should give similar strength values. This was verified by austenitising the tensile specimens of welds A and C at 1000°C for 15 min and quenching in iced brine. The stress-strain curves in Fig. 5.23 show that both the heat treated welds have similar yield strength but different ultimate-tensile strengths, as expected. Hence it is a conclusive evidence that a lower Ac_1 in combination with lower hardenability makes weld C softer than weld A. When the microstructure is completely martensitic, the yield

strengths of the two are similar.

5.5 Effect of Interpass Temperature on Low–Manganese High–Nickel Weldments

A variety of measurements were done on weld C, as a function of the interpass temperature. Fig. 5.24 shows a comparison of measured values against those predicted using neural network models (chapter 4); there is excellent agreement. It is emphasised that the experimental data illustrated were not used in creating the neural network model.

Decrease in interpass temperature increases the cooling–rate and hence leads to the formation of hard martensite, thus increasing the yield strength and vice versa. Insensitivity to interpass temperature is advantageous as it gives reproducible mechanical properties during practical welding when interpass temperatures are unlikely to be carefully controlled. The measured values show that yield strength of weld C is not sensitive to interpass temperature.

5.6 Tempering Resistance of 7Ni-2Mn and 7Ni-0.5Mn wt% Welds

Rods of 3 mm were machined from welds A and C and austenitised at 1000 °C sealed in a quartz tube with a partial pressure of argon for 15 min and quenched in iced brine to ensure a completely martensitic microstructures. After quenching the rods were tempered at 100 °C, 200 °C and 250 °C each for 15 min, 350 °C for 1 h and 2 h, and 500 °C for 3 h.

The experiments showed that in the as–quenched and tempered states, weld A remains harder than weld C. Even at temperatures as low as 100 °C for 15 min, there is

a drop of ≈ 40 VHN in both the welds. But, by doing so the hardness of weld C has a hardness of 320 VHN which is much less than that of weld A which has 345 VHN. And for all other conditions weld A maintains an average hardness of 338 VHN, whereas weld C shows a large scatter.

5.6.1 Transmission–electron microscopy of tempered steels

A thin foil of weld A and C tempered at 500 °C at 3 h was used in transmission electron microscopy (TEM) examination. The microstructure of welds A and C after heavy tempering at 500 °C for 3 h is expected to be ferrite. However, examination of thin foils under TEM shows that martensite laths are clearly visible (Fig. 5.26) since the tempering temperature is well below recrystallisation temperature. Weld A has a very fine lath compared to weld C. At a low concentration of carbon, martensite is not essentially different from ferrite, since the tetragonality of martensite is less and resembles a body–centered cubic structure.

5.7 Discussion and Conclusions

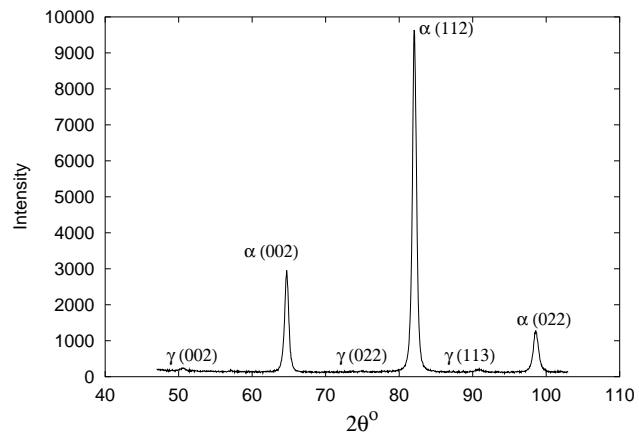
The generally accepted concept that addition of nickel improves toughness of ferritic steel has been shown to be incorrect. Neural network analysis of a very large database has shown that for a particular class of high strength welds, nickel only improves the toughness at low manganese concentrations ($\approx \leq 0.6$ wt%). This conclusion has been verified experimentally, by manufacturing a novel weld designated “weld C”.

The toughness of weld C is high, but comparisons should be strictly made at the same strength. A study of temperature dependence of hardness was conducted in order to make a fair comparison but unfortunately the hardness curves of the welds studied did not overlap for a valid hypothesis. A comparison with weld H4 having similar strength to that of weld C did however prove that the latter has significantly improved toughness.

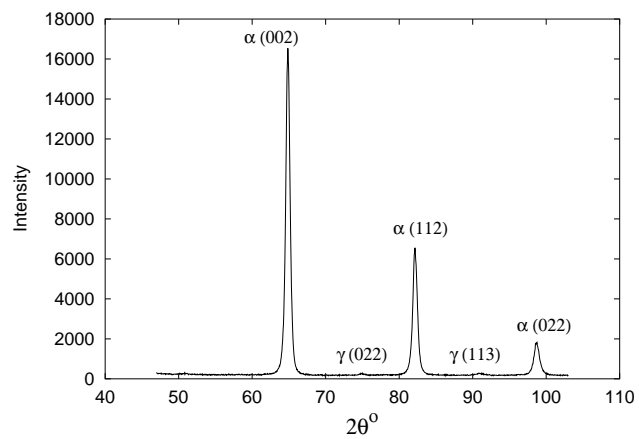
The quantity of retained austenite was measured for each weld but the differences were found to be too small to make any sensible conclusions about its role in determining the toughness of the three welds.

Hardness measurements along the weld centerline on a cross-section of the welds A and C showed that on a microscopic scale the latter had a greater variation in hardness. This is explained by the larger Ac_1 temperature which leads to an excessive tempering of the underlying structure during multipass welding. The hardness of tempered microstructure in weld C is much lower than that of weld A. High resolution hardness maps demonstrated that the overall hardness of weld C is also less than that of weld A which tends to contain hard patches. And this is merely due to the tempering effect, as confirmed by the fact that an austenitised and quenched specimen of weld C has a hardness of 373 VHN compared to a maximum hardness value of 355 VHN in a weld. Further, tensile tests of austenitised and quenched specimens of welds A & C resulted in essentially the same yield strengths for both welds, proving that untempered martensite in weld C has the same strength as weld A.

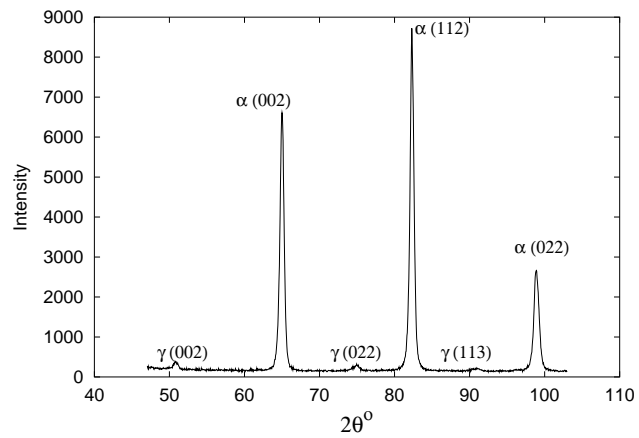
The reason for low toughness of weld A is its hardness. Three different welds with varying toughness were mapped for hardness to check if hard zones related to decrease in toughness. All other elements being constant, the three welds had a typical composition of 9Ni-0.03C-0.5Mn(weld D), 7Ni-0.06C-0.5Mn (weld E) and 10.5Ni-0.03C-0.5Mn-1.13Cr (weld F) wt%. The Charpy toughness of welds D, E & F were 60 J, 85 J and 29 J respectively at -60 °C. Hardness measurements as seen from the frequency plots in Fig. 5.18 shows that weld F has about 50% of its regions with hardness more than 350 VHN, whereas welds D & E have regions less harder than 350 VHN. This strongly supports the fact that high hardness of the weldment is the cause for decrease in toughness of welds A & D.



(a) Weld A



(b) Weld B



(c) Weld C

Figure 5.9: Intensity vs 2θ plots for welds A, B and C showing the austenite and ferrite peaks obtained from X-ray diffraction experiments.

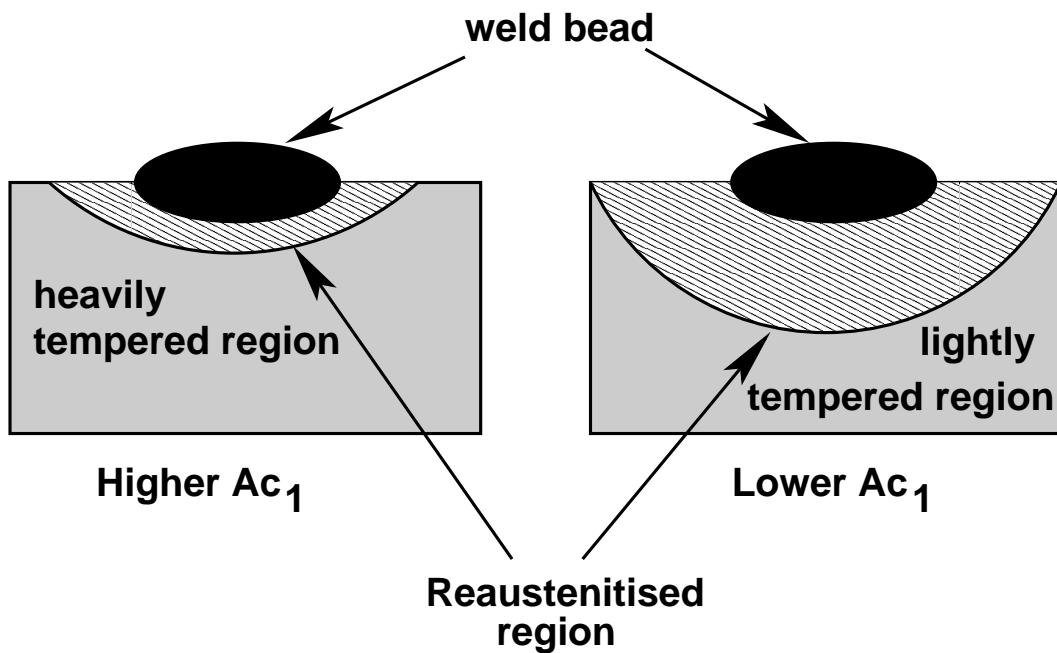


Figure 5.10: Effect of Ac_1 on the hardness of final weld microstructure of welds A and C [5].

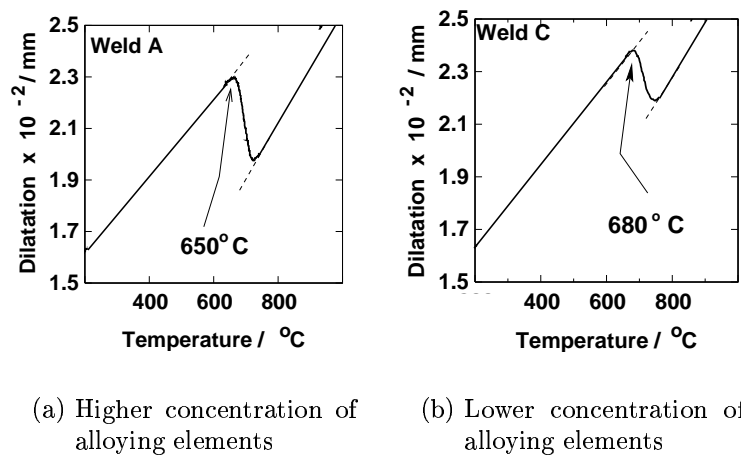


Figure 5.11: Dilatation curves for welds A and C, showing corresponding Ac_1 temperatures, obtained at a heating rate of $10\text{ }^{\circ}\text{C s}^{-1}$ using a cylindrical sample of diameter 7 mm and height 12 mm.

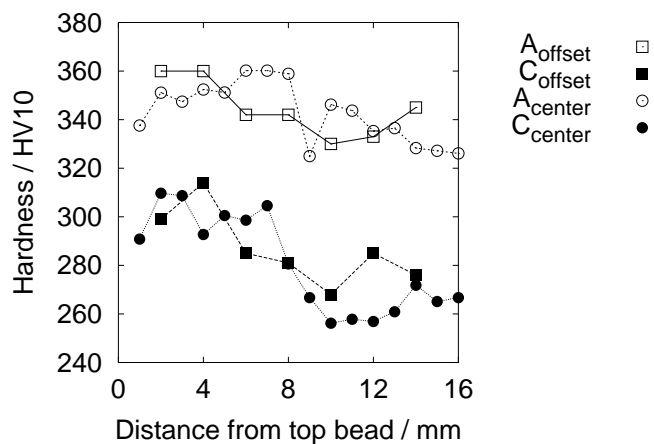


Figure 5.12: Variation in hardness along the depth, for welds A and C measured along the weld centerline and at a offset distance of 5 mm from the weld center.

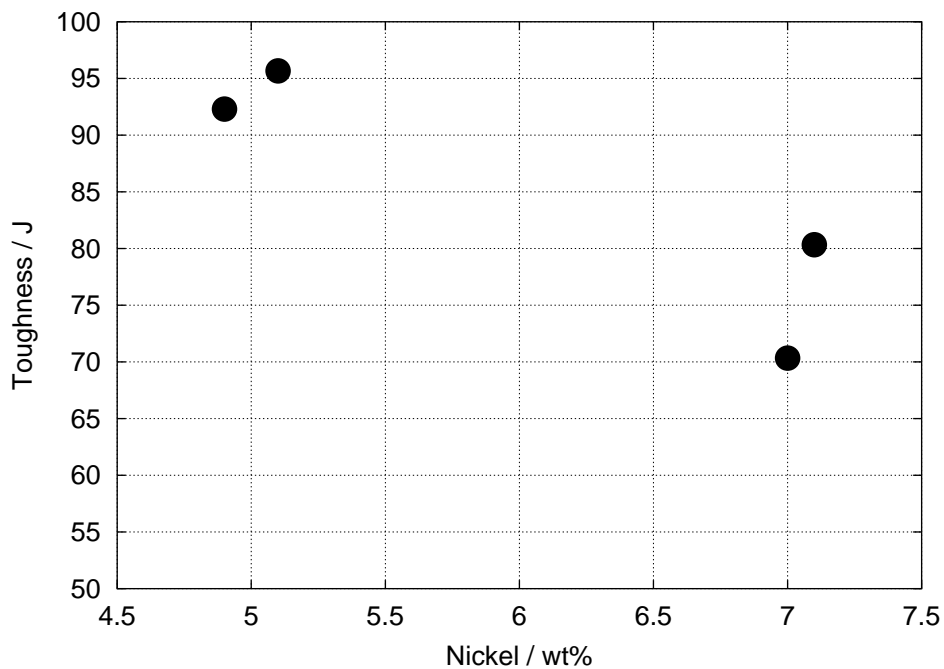


Figure 5.13: Welds having same YS/UTS ratio (0.94), but show different toughness values at -60 °C. All the four experimental welds have $\approx 0.1\text{C}-0.6\text{Mn}-0.3\text{Si}-0.01\text{S}-0.01\text{P}-0.4\text{Mo}$ wt% except for nickel content.

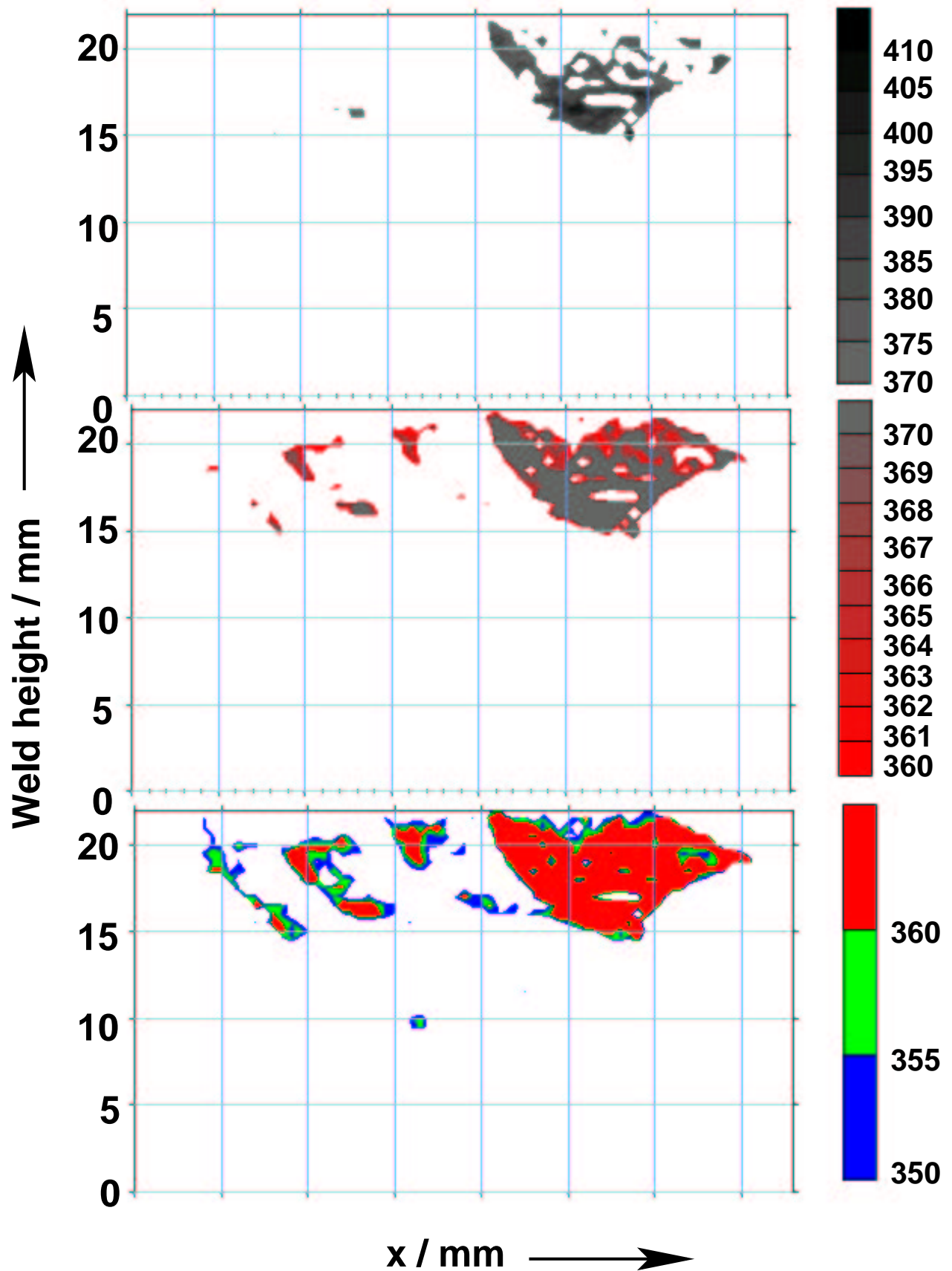


Figure 5.14: Hardness map of 3Ni-2Mn wt% weld. H1, showing a uniform hardness below the top layer.

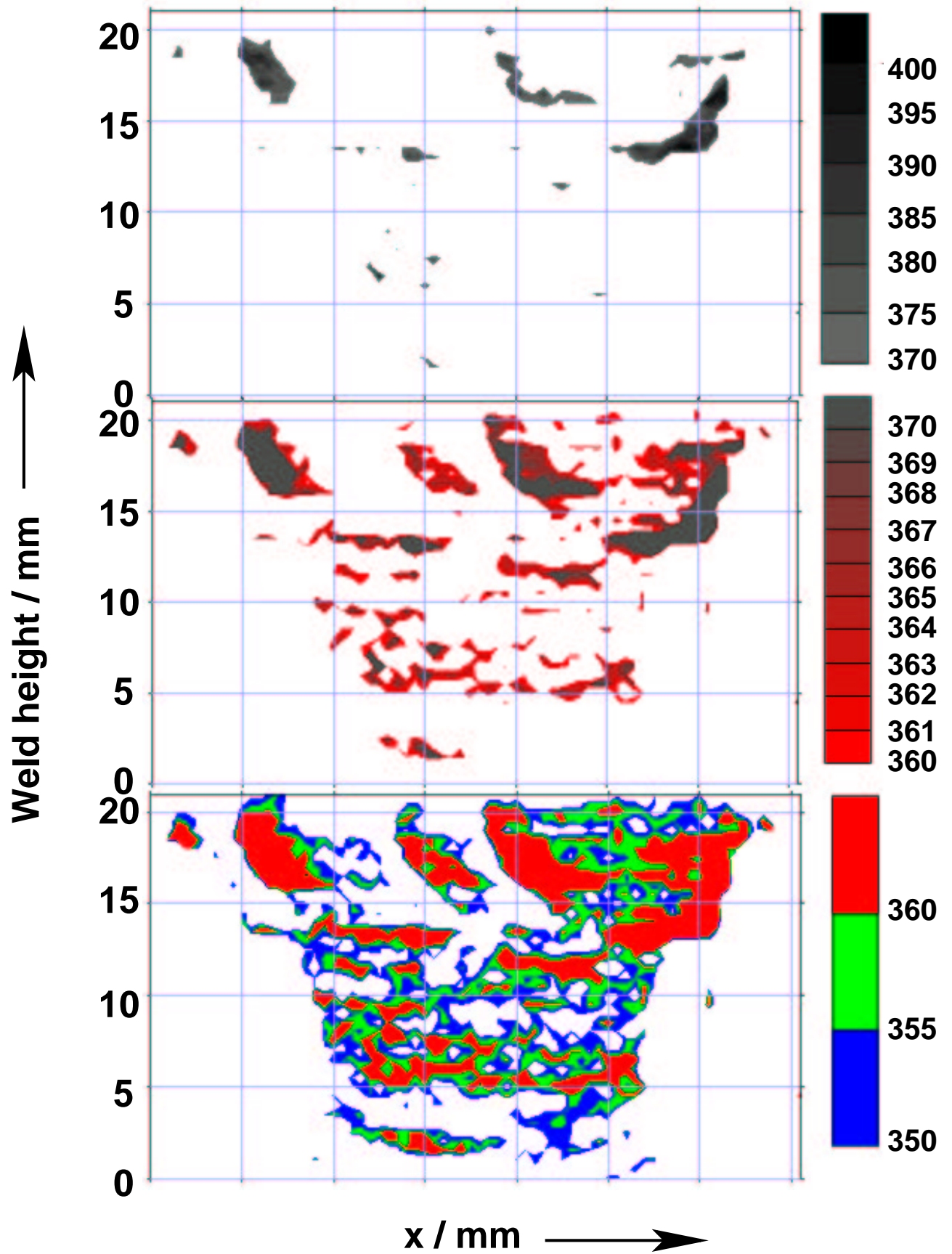


Figure 5.15: Hardness map of 7Ni-2Mn wt% weld.

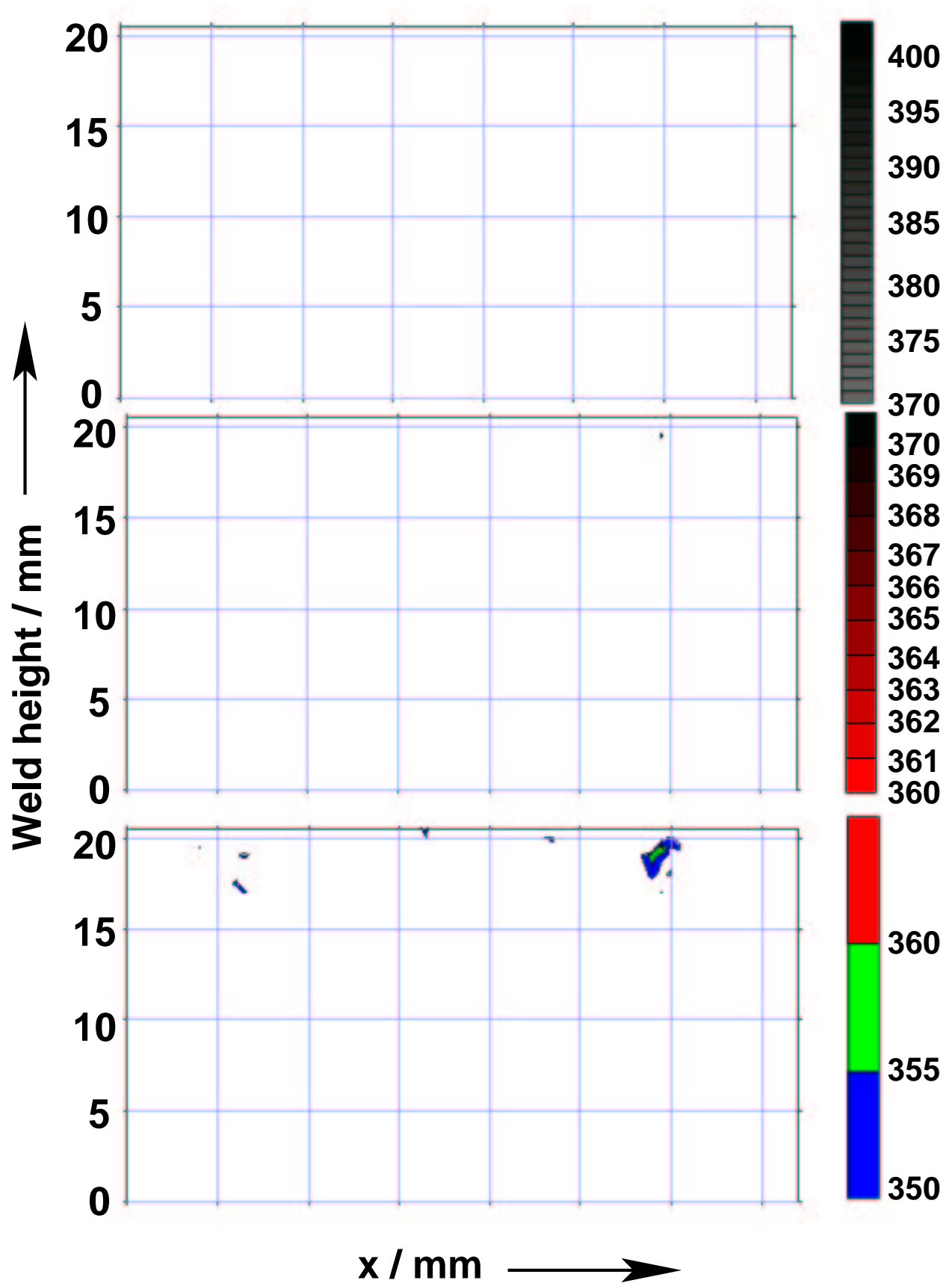
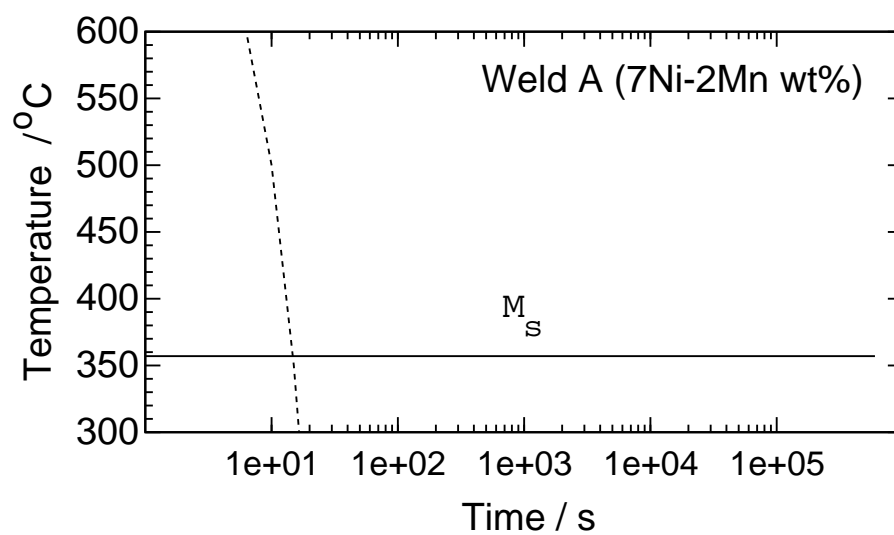
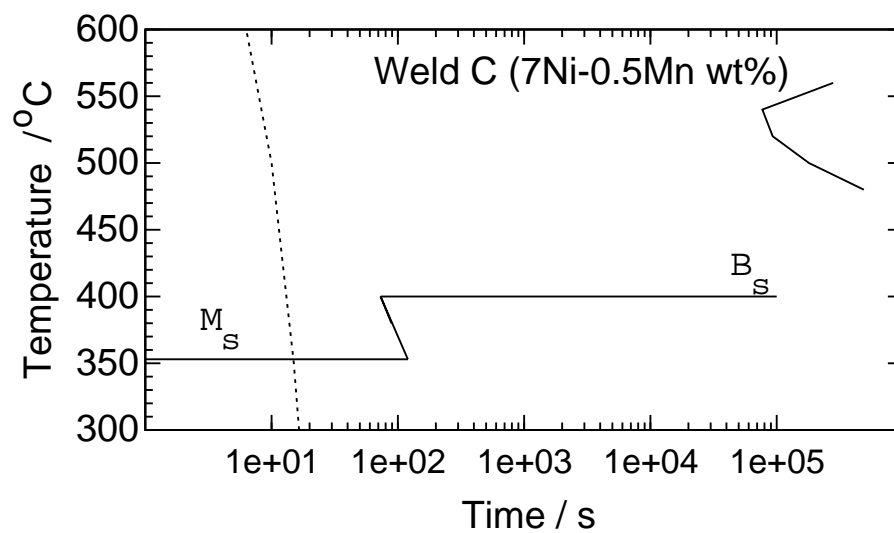


Figure 5.16: Hardness map of 7Ni-0.5Mn wt% weld.



(a)



(b)

Figure 5.17: Calculated TTT diagram of welds A and C along with cooling curve for a cooling rate of $30\text{ }^{\circ}\text{C s}^{-1}$.

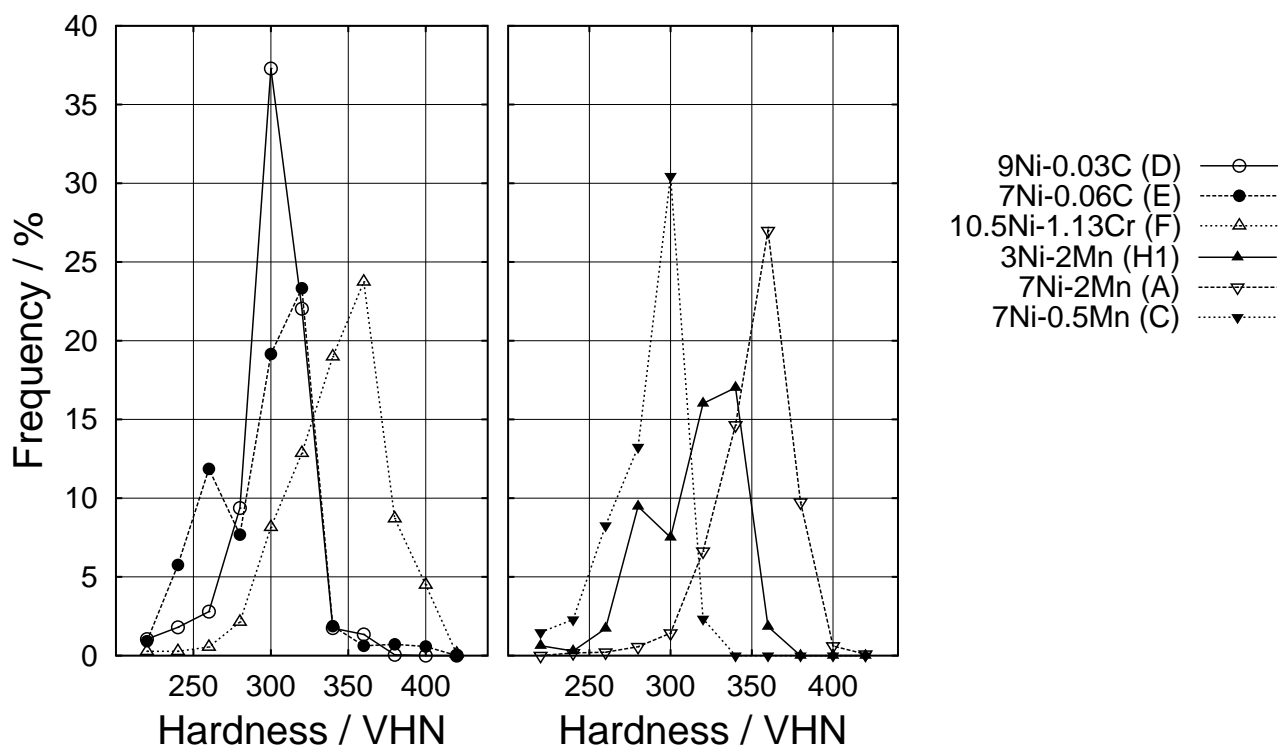
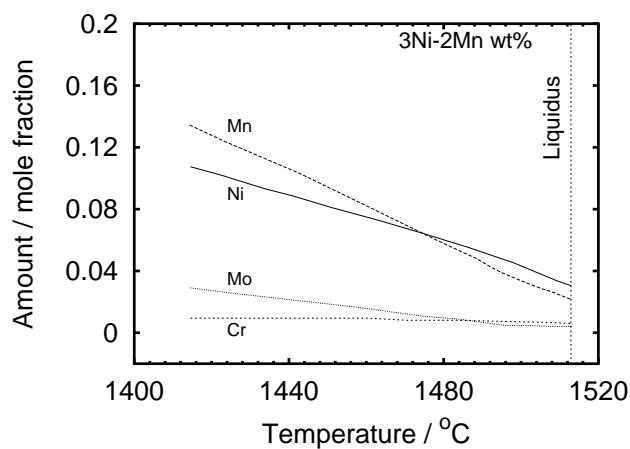
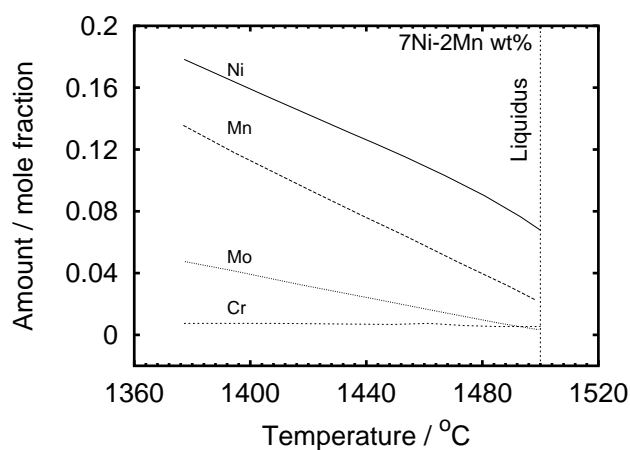


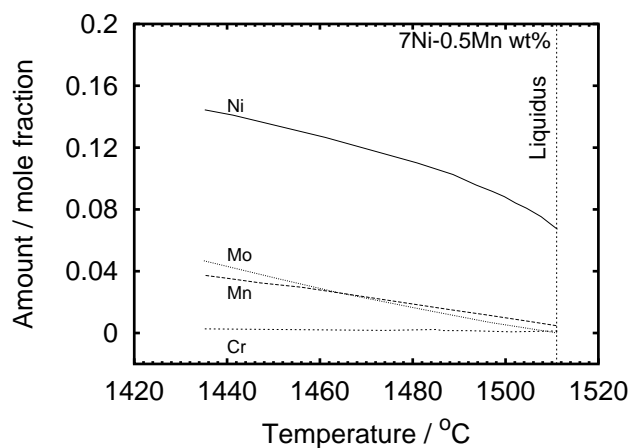
Figure 5.18: Frequency distribution of hardness in the welds. Welds D, E & F have 0.5 wt% Mn. Letters in parenthesis represent weld identifications.



(a) Weld H1, liquid solidifies to δ -ferrite

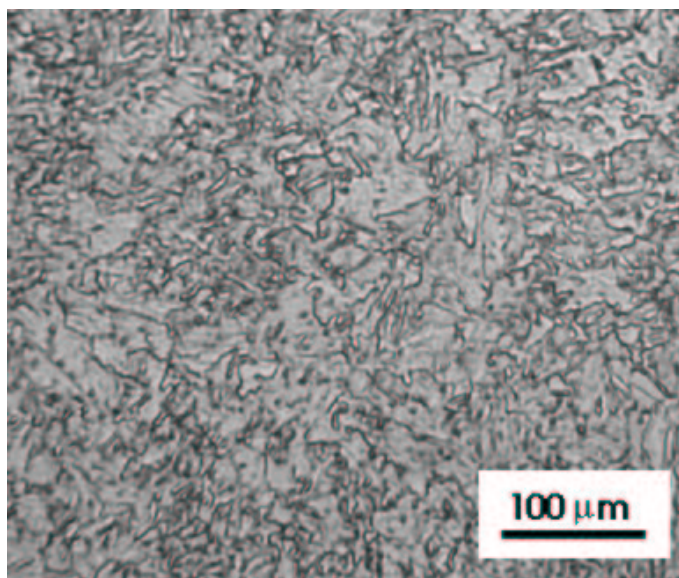


(b) Weld A, liquid solidifies to austenite

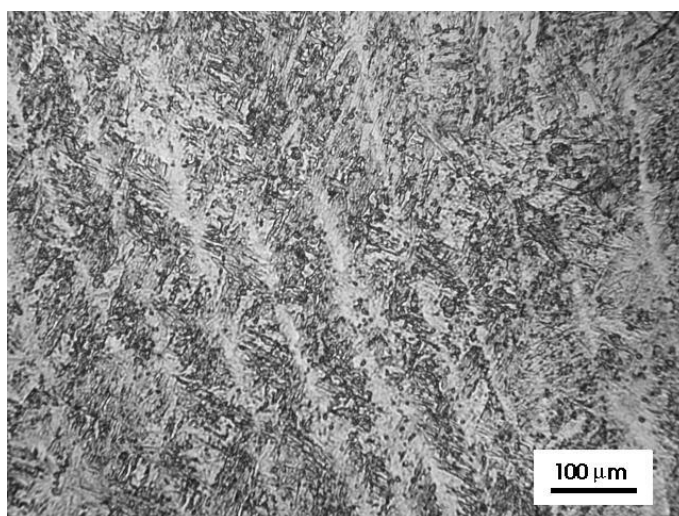


(c) Weld C, liquid solidifies to austenite

Figure 5.19: Calculated segregation of Ni, Mn, Mo and Cr during solidification of alloys. Vertical axis represents the amount of elemental concentration in the liquid.

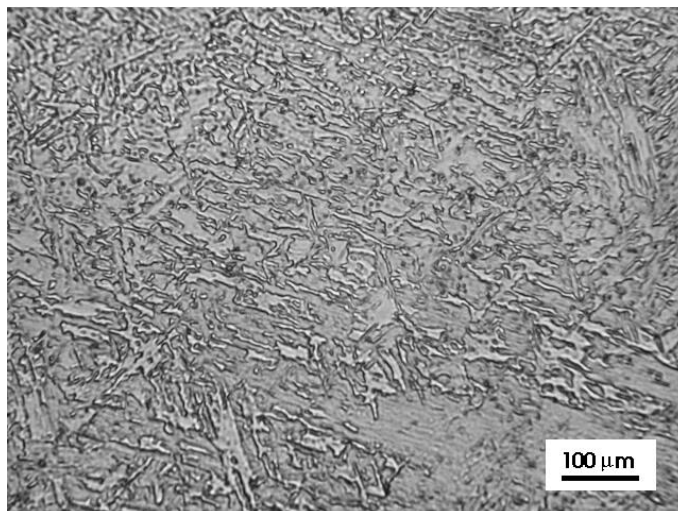


(a) H1(3Ni-2Mn), Top weld bead

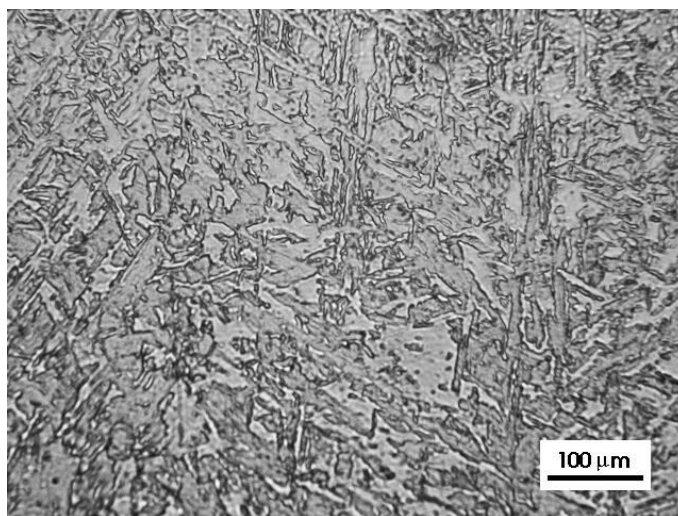


(b) Weld A (7Ni-2Mn), Top weld bead

Figure 5.20: Optical micrograph of welds H1 and A.

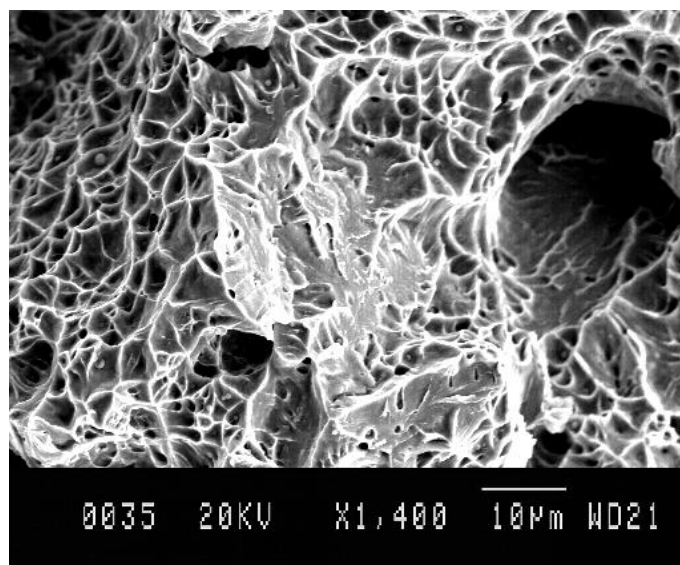


(a) 7Ni-0.5Mn, Top bead

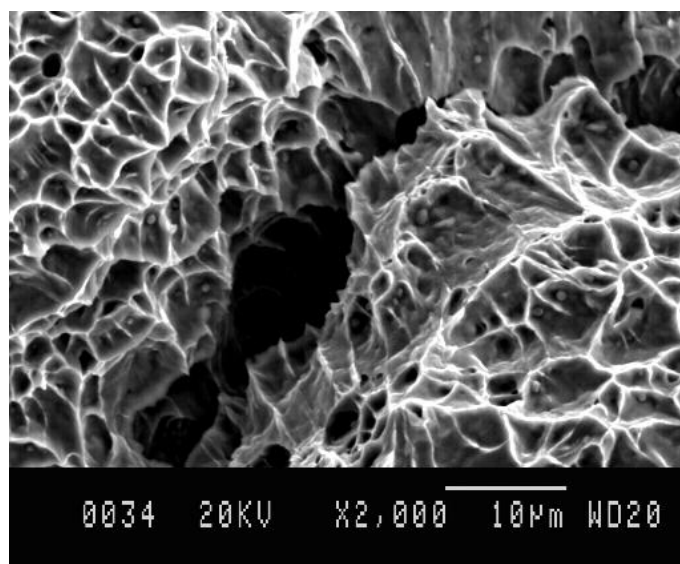


(b) 7Ni-0.5Mn, Center bead

Figure 5.21: Optical micrograph of top bead and center of weld C.

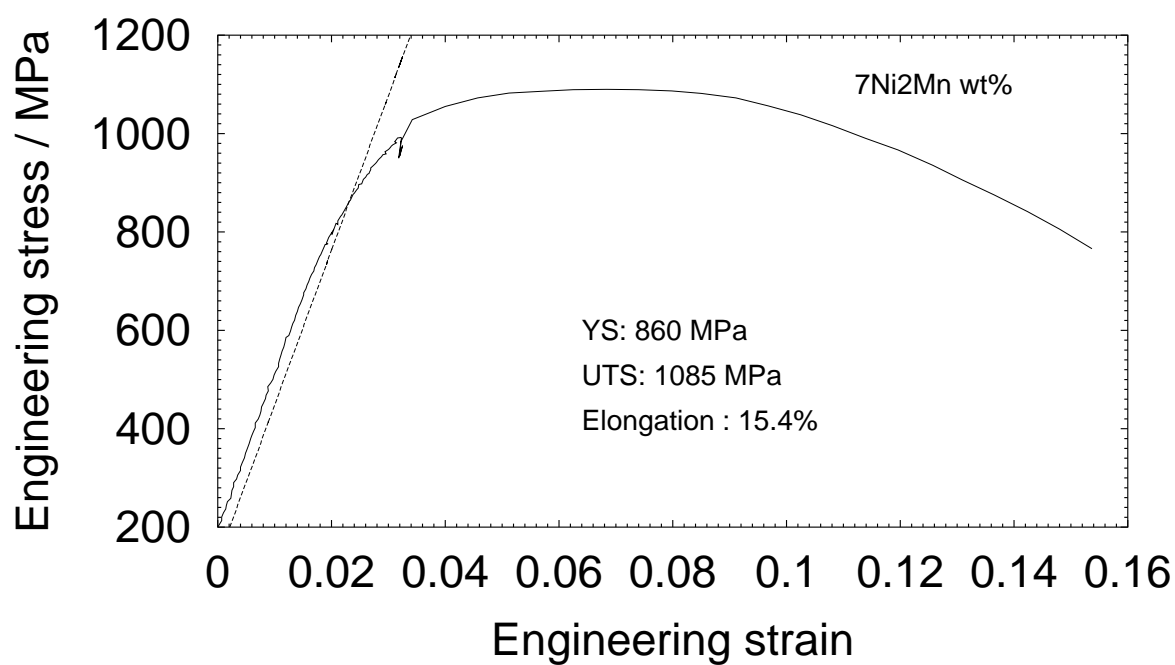


(a) Weld A

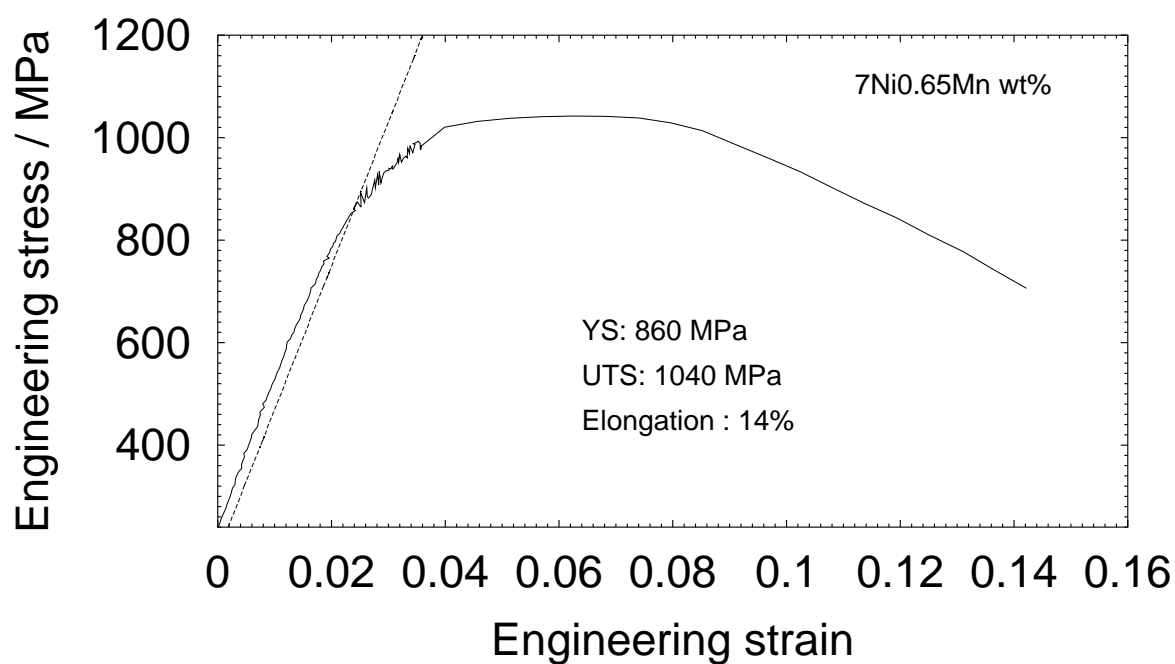


(b) Weld C

Figure 5.22: Scanning electron micrograph of Charpy test specimens fractured at -60°C .

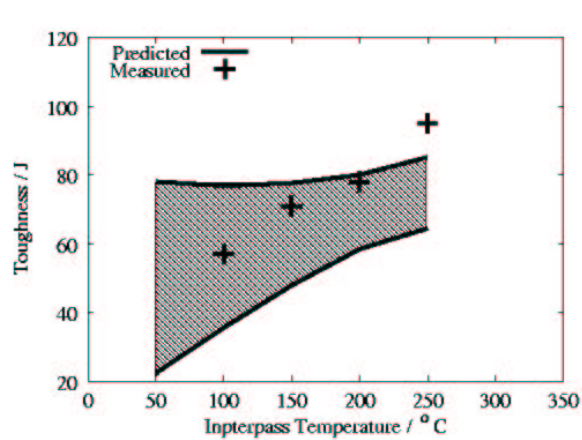


(a)

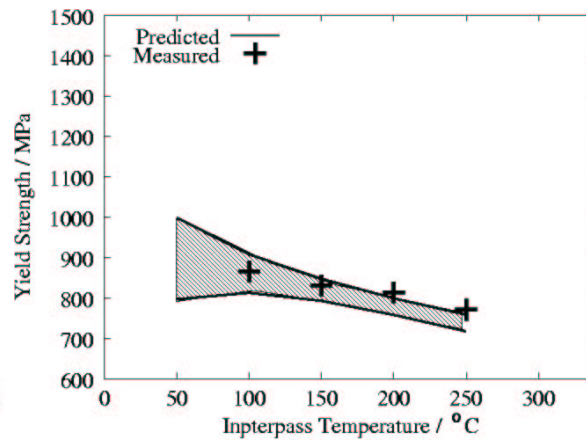


(b)

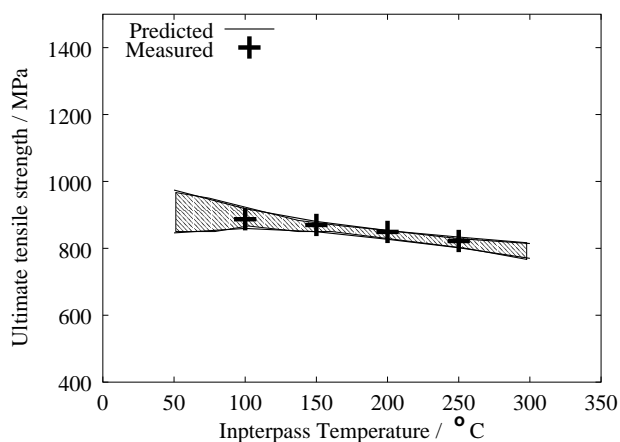
Figure 5.23: Engineering stress-strain graphs of welds A and C austenitised at 1000 °C for 15 min and water quenched.



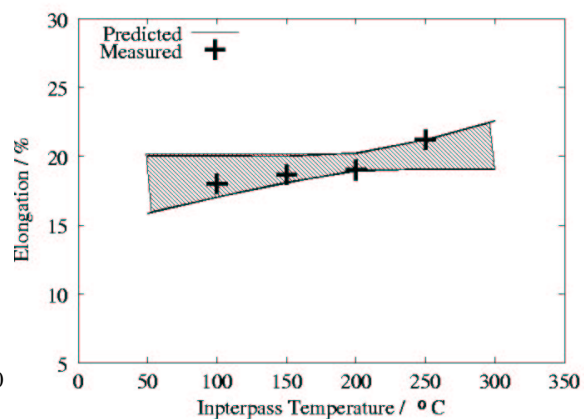
(a) Charpy toughness at -60 °C.



(b) Yield Strength



(c) Ultimate Tensile Strength



(d) Elongation

Figure 5.24: Comparison of measured and predicted mechanical properties, for composition of weld C with a heat input of 0.8 kJ mm^{-1} . The shaded bands represent the calculated values bounded by the estimated $\pm 1\sigma$ uncertainties.

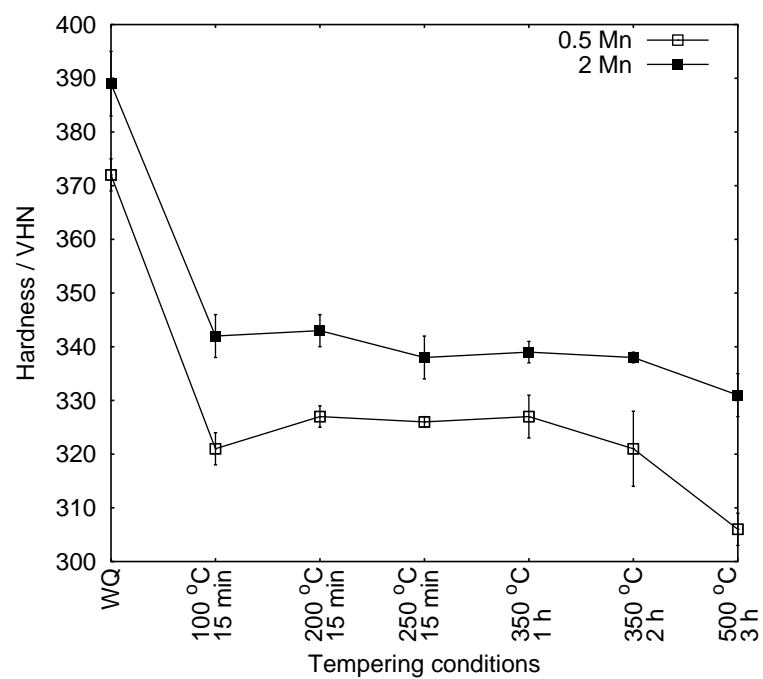
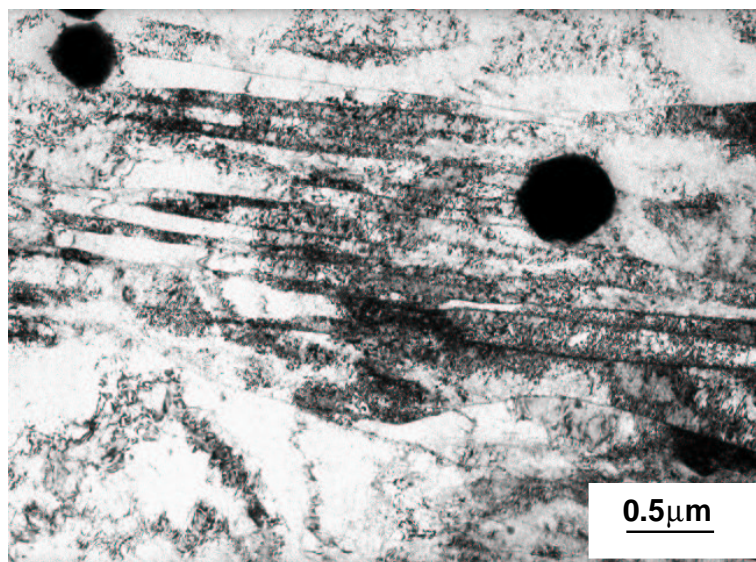
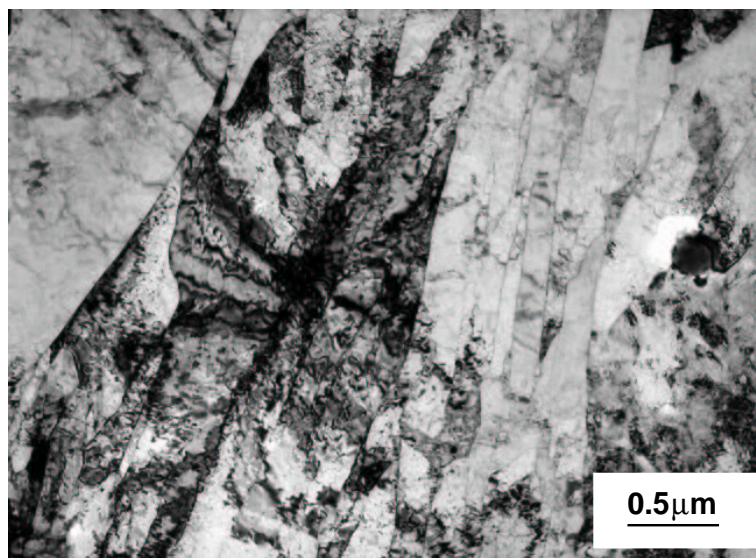


Figure 5.25: Variation in hardness of welds A and C for different tempering temperatures and time.



(a) weld A - Microstructure is highly dislocated with finer laths. Average lath thickness is $0.9 \pm 0.3 \mu\text{m}$ for six measurements done on the micrograph using a normal ruler. Also shows presence of manganese sulphide inclusions.



(b) weld C - Microstructure has less dislocation density with larger laths. Average lath thickness is $2.2 \pm 0.3 \mu\text{m}$ for five measurements.

Figure 5.26: A bright-field TEM image of the matrix, which shows the martensite laths. Tempered at 500 °C for 3 h.

Chapter 6

FERRITIC POWER PLANT STEELS

Most of the electricity produced in the world comes from fossil fuel power plant, which generate steam to drive the turbines. There are major concerns however, about the green house gases associated with such power generation [70–74]. The problem can be mitigated by improving the thermal efficiency by increasing the inlet temperature and pressure of steam which passes through the turbine (Fig. 6.1). Higher temperatures necessitate better

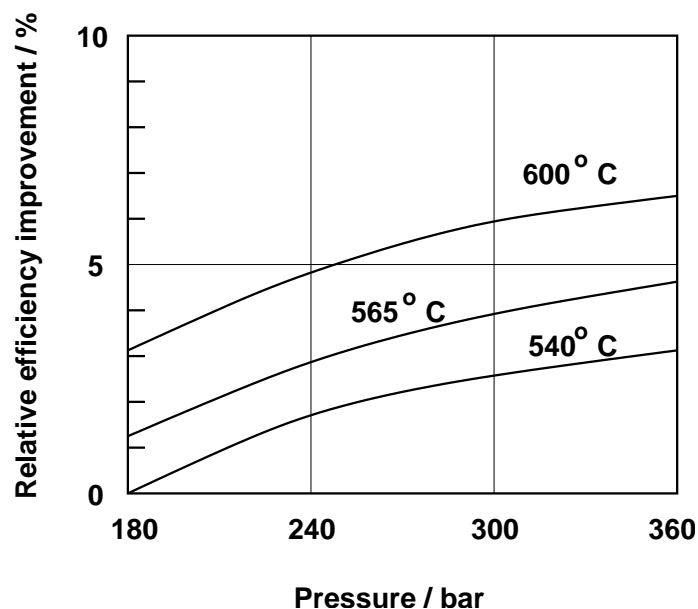


Figure 6.1: Effect of steam temperature and pressure on the relative thermal efficiency in a thermal power plant. At higher temperature and pressure, the efficiency increases relative to the one at lower temperature and pressure.

steels with greater creep and oxidation resistance. Hence the ferritic 9–12 wt% Cr steels, which are expected to serve reliably for a period of about 30 years. Ferritic steels have a low thermal expansion coefficient ($\approx 9 \times 10^{-6}/^{\circ}\text{C}$) and higher thermal conductivity than austenitic steels and hence have an advantage of resisting thermal fatigue [75]. This chapter describes the design philosophy and microstructure of ferritic steels. Austenitic steels are beyond the scope of this thesis.

6.1 Design Philosophy

The basic contribution to the creep strength of any steel comes from its alloying elements. Alloying elements determine the type of base microstructure¹ formed. Heat treatment then leads to formation of different kinds of precipitates. The strength therefore comes from dissolved alloying elements, the base microstructure, and precipitates (Fig. 6.2).

Alloying elements can be categorised as substitutional (Cr, V, Nb, Mo, W, Cu, Mn etc.) and interstitial (C, N). Chromium is particularly needed for corrosion and oxidation resistance at high temperatures in steam-containing environments [76].

Ferritic steels can be classified further into “carbon” steels (C, Mn, *etc.*), low alloy steels (0.5Mo/1Mo-2.25Cr wt%), intermediate alloy steels (5–10 wt% Cr) and high alloy steels (12 wt% Cr martensitic steels). Fig. 6.3 shows the compositions of typical heat resistant steels [28, 77]. Low alloy steels are used below and upto 565 °C. Intermediate and high alloy steels are used above 565–600 °C. Modern heat-resistant steels have 9–12 wt% Cr because of the need for corrosion and oxidation resistance.

The martensitic microstructure is a by-product of high chromium. From the Fe–Cr equilibrium phase diagram (Fig. 6.4), it is clear that the austenite phase field is

¹microstructure of the matrix, say martensite or bainite

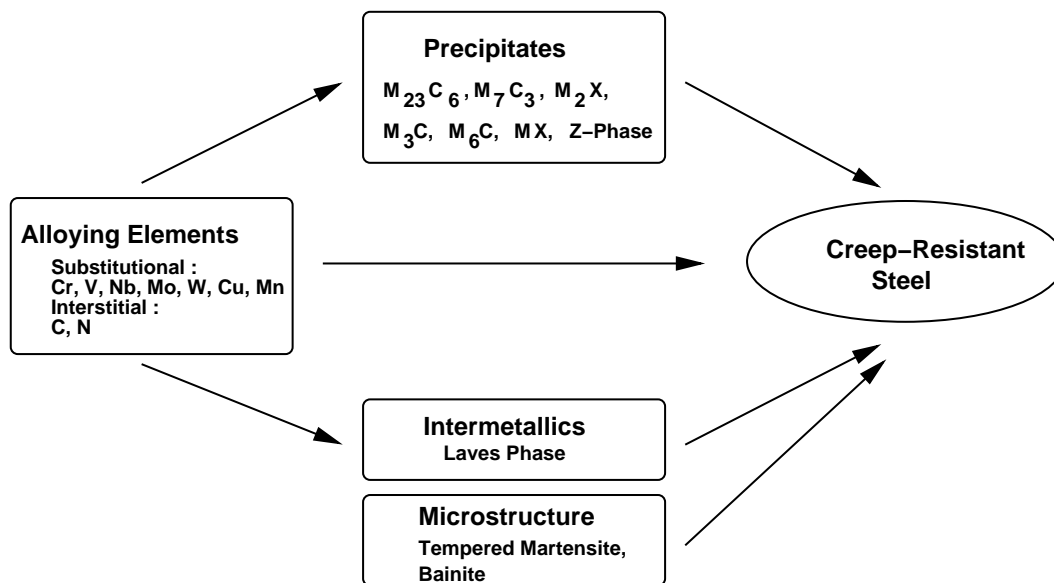


Figure 6.2: Design philosophy of a creep-resistant steel. In precipitates, ‘M’ is a combination of metal atoms such as Cr, Fe, Mo, V, Nb, and X is usually C and/or N

narrow for steels having Cr concentrations greater than 9 wt%. The presence of δ -ferrite, which occurs at high chromium concentration, in the final microstructure is considered deleterious for the creep strength and toughness [76].

In practice, the steels are used in large diameter and thick-walled pipes with critical properties being oxidation resistance, creep strength, weldability and toughness.

Chromium is an important alloying element since it improves both corrosion and oxidation resistance [78]. The concentration is usually about 2 or 9–12 wt% in ferritic steels; steels with intermediate concentrations are not common for reasons which are not clear [28]. Higher Cr contents stabilise δ -ferrite [79], so the chromium is balanced with austenite stabilising elements like Ni, Cu and Co are used.

Ni, Cu and Co are austenite stabilising elements. Nickel is known to have an adverse effect on the creep strength of high-chromium steels [28], by enhancing the coarsening rate of precipitates [80]. In a 0.1C–11Cr–2W–0.4Mo–1Cu wt% steel, it was found that for copper concentrations of 0, 1 and 2 wt%, the creep-strength dropped appreciably

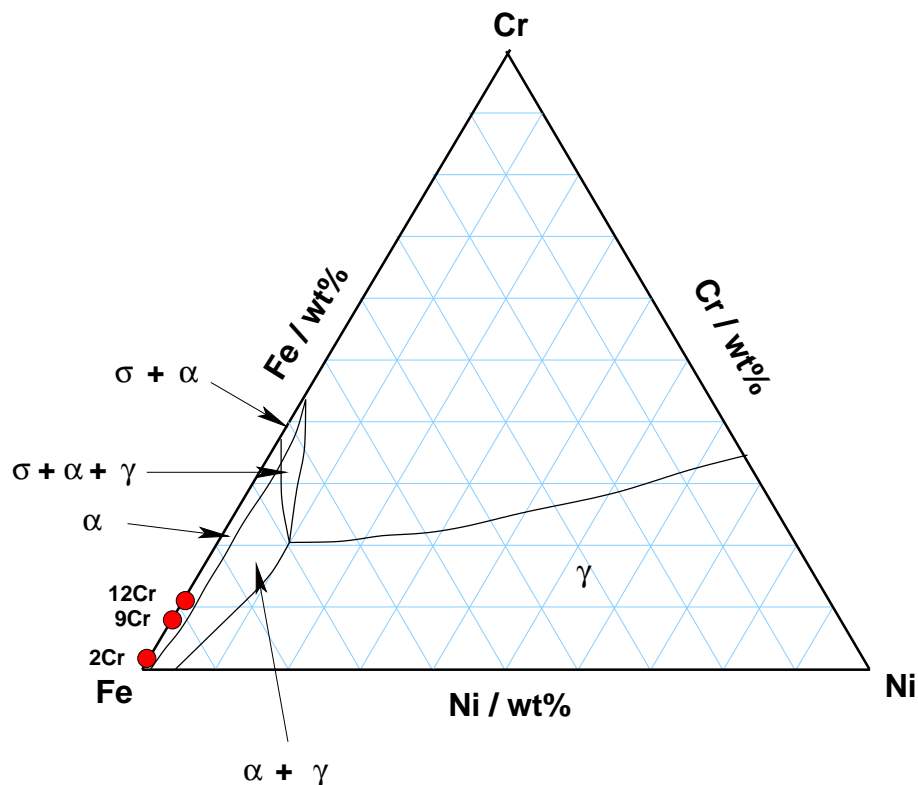


Figure 6.3: A Fe-Ni-Cr ternary diagram showing the regions where the typical ferritic heat-resistant steels lie without the presence of nickel at 800 °C. Where γ is austenite, α is ferrite and σ_{pha} is an intermetallic compound of Fe and Cr.

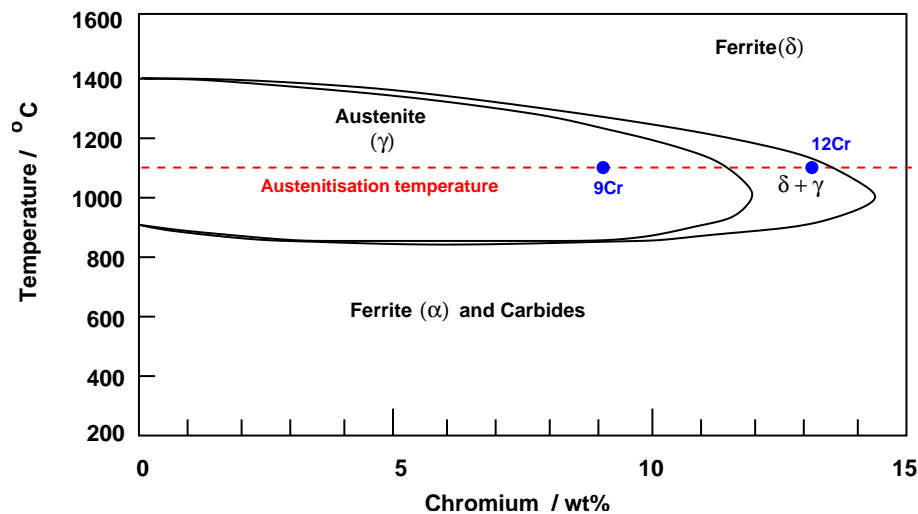


Figure 6.4: Fe-Cr equilibrium phase diagram. Austenitisation is normally performed at 1100 °C as shown by the red line.

above 0.4 wt% Ni (Fig. 6.5 [80]). The effect of Ni on a 12CrMoV steel was studied by Vodárek and Strang [81], who observed that nickel accelerated the dissolution of M_2X by stimulating M_6X which has a high solubility for nickel. Nickel also accelerates the coarsening rate of $M_{23}C_6$ [82].

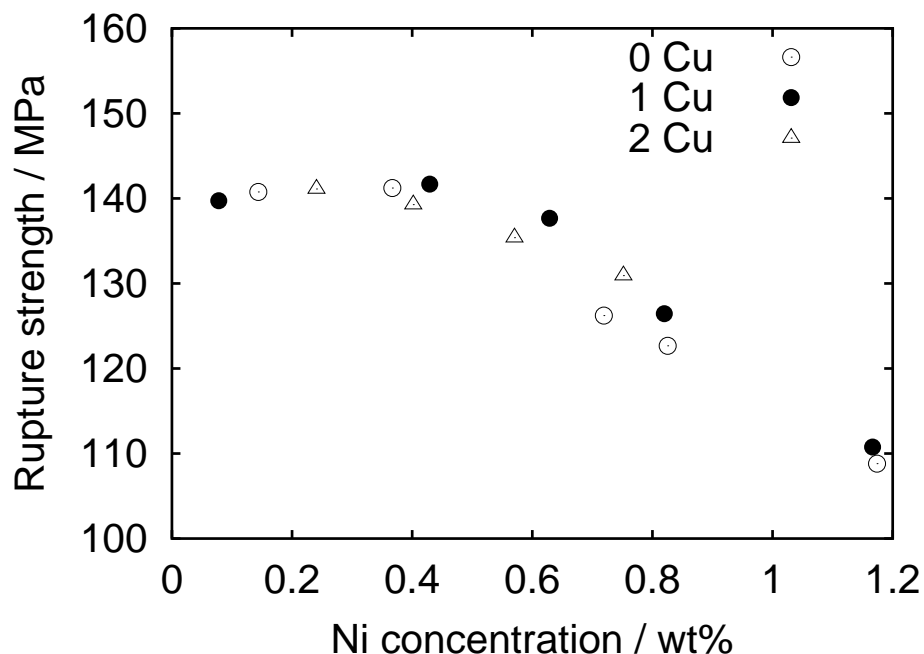


Figure 6.5: Effects of Ni and Cu on the extrapolated 10^5 h creep rupture strength of 0.1C-11Cr-2W-0.4Mo-Cu wt% steels at 600 °C.

Copper is generally used as a precipitation hardener, with copper particles forming on martensite lath boundaries [80], thereby retarding the recovery of martensite [83].

Cobalt strengthens the ferritic matrix and stabilises the fine MX precipitates [84]. It remains in solid solution in 12 wt% Cr steels [85] and enhances the creep strength. An example of this in 12CrWCoB wt% steel at 650 °C is shown in Fig. 6.6 [86].

Mo, W and Re also contribute to solution strengthening. Typical molybdenum concentrations are limited to below 1.5 wt% in order to avoid δ -ferrite [25, 87-89] and Laves phases [90]. Re is used in concentrations of about 0.5 wt% [91-93], though the mechanism by which it improves the creep strength remains uncertain.

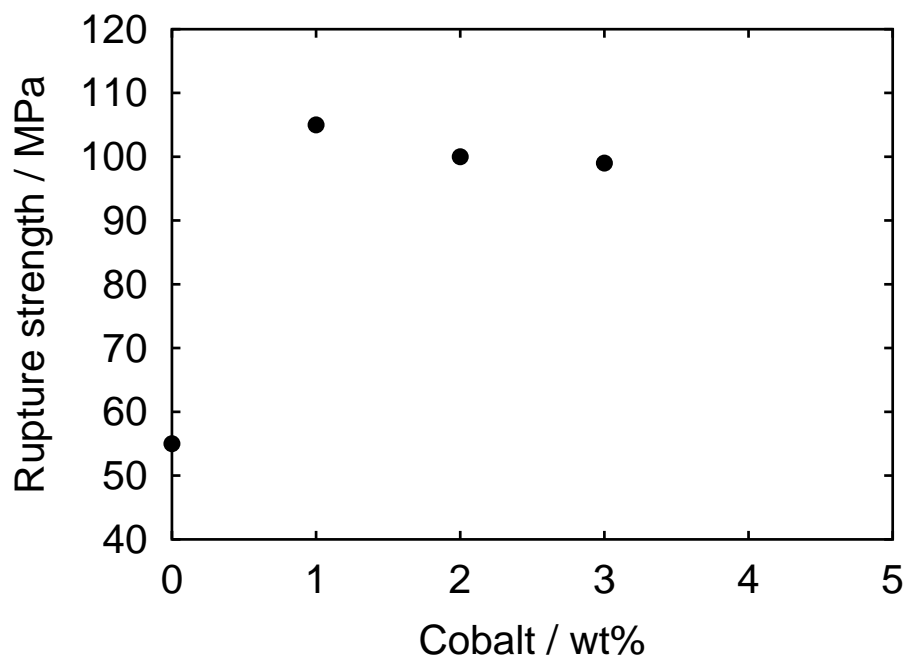


Figure 6.6: 650 °C \times 10⁵ h creep rupture strength as a function of cobalt content for a 12 wt% CrWCoB steel [86].

Both W and Mo stabilise M_2X with W being less effective than Mo for identical concentration. Tungsten is a good solid-solution strengthener and also precipitation hardens via $M_{23}C_6$ and Laves phase [94]. In general, only about 0.5 wt% of W remains in solid-solution when Laves and $M_{23}C_6$ precipitates [95]. A recently developed low-carbon alloy with 2.25Cr wt% and 1.6 wt% W is found to have excellent creep properties and weldability [96].

V, Nb, Ti, Ta and Nd combine with C and N to form carbides, nitrides or carbonitrides, which are fine and stable, thus contributing sufficiently to long-term creep strength [97–100]. Fig. 6.7 shows that an optimum combination of V and Nb is necessary in 12 wt% Cr steels to achieve the highest creep resistance [87,97]. The strengthening due to vanadium is less effective when it forms a carbide, because this then competes with molybdenum-rich carbides [101].

Ti is a strong carbide and nitride former and can improve the creep rupture strength

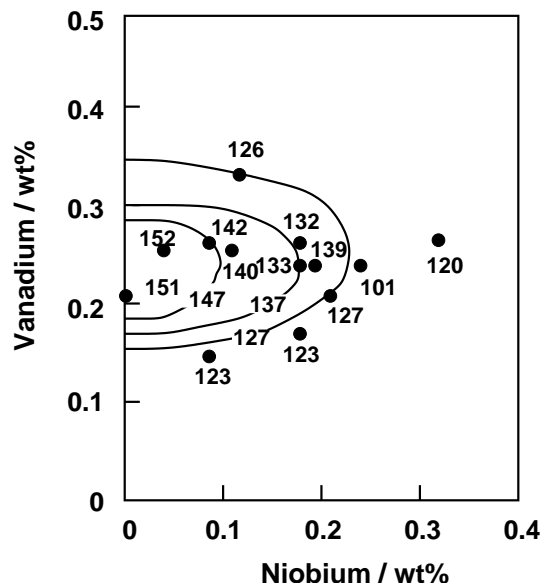


Figure 6.7: Effect of V and Nb on 12 wt% [87].

of ferritic steels. This was demonstrated by Pilling *et al.* on a 2.25Cr1Mo steel with titanium additions upto 0.038 wt% [98]. However, coarse titanium based precipitates are detrimental to creep ductility [102].

Additions of Ta and Nd to a 0.1C-11Cr-3W-3Co-V-Nb-N wt% steel reportedly increased the creep strength of weld joints [84], via stable TaN and NdN precipitates.

C and N are not only austenite stabilisers but vital in precipitation reactions. Concentrations of nitrogen are generally below 0.05 wt% since larger concentrations require special steel-making procedures [103]. Hidaka *et al.* have demonstrated that increasing nitrogen concentration in boron-containing steels decreases the creep-rupture strength (Fig. 6.8) [86]. Nitrogen in other circumstances stabilises Cr_2N , thus contributing to increase in creep-rupture strength [85].

Boron improves hardenability and enhances grain boundary strength, and hence can contribute to creep strength [28]. It also is soluble in M_{23}C_6 [104]. A recent study showed that boron improves the long term creep strength of 9Cr-3W wt% steel but large concentrations lead to the formation of borides are ineffective (Fig. 6.9) [105].

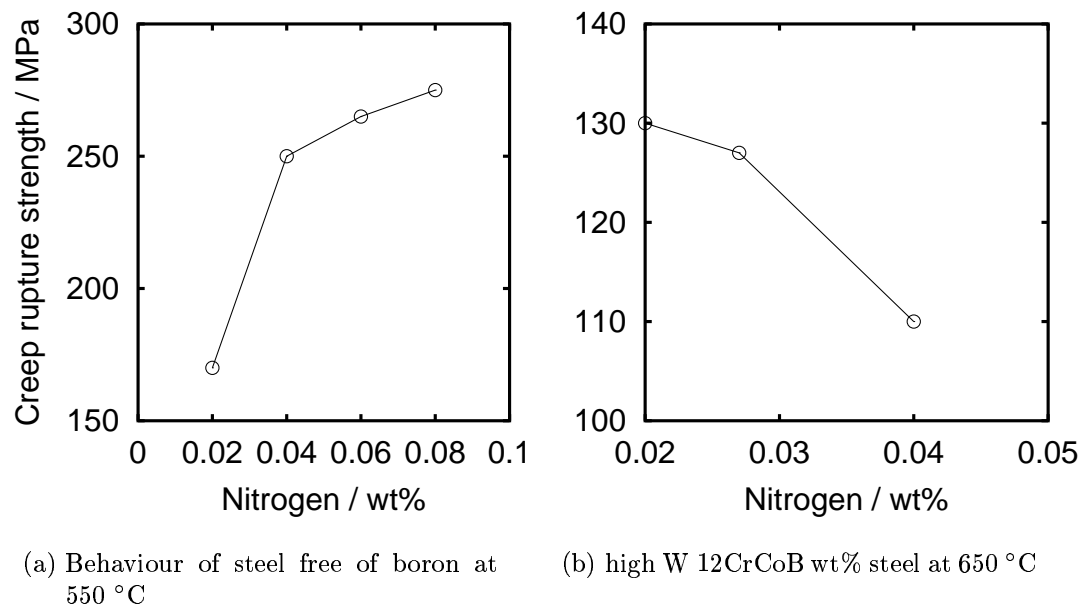


Figure 6.8: Creep rupture strength of a 12 wt% Cr steel as a function of N content (after Hidaka *et al.*)

Silicon and manganese should be minimised in order to improve creep strength [107–109]. Silicon additions to 9Cr steels have been found to increase the precipitation and coarsening of Laves phase [110,111]. Abe reports that austenite stabilising elements are added purely to combat the ferrite stabilising effect of silicon [25]. Silicon is essential for good oxidation resistance and indeed is useful in the steel-making process itself.

Fig. 6.10 shows the scheme for the design of heat-resistant steels [28].

6.2 Precipitates in Power Plant Steels

Creep resistant steels containing 9–12 wt.% Cr, used in many power plant applications have, tempered martensite microstructures containing a range of precipitates including $M_{23}C_6$, M_2X and MX . $M_{23}C_6$ precipitates are located mainly at the prior austenite and martensite lath boundaries in the microstructure, while the much finer M_2X and MX

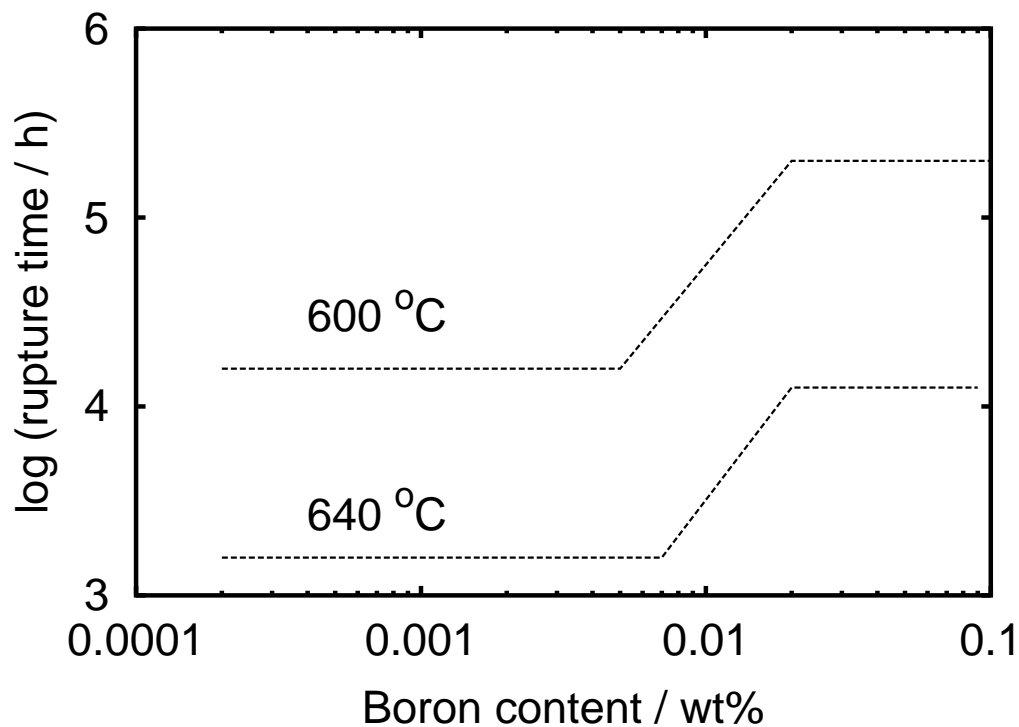


Figure 6.9: Schematic illustration of long-term creep rupture data for 10 wt% CrMoVNb Steel [106].

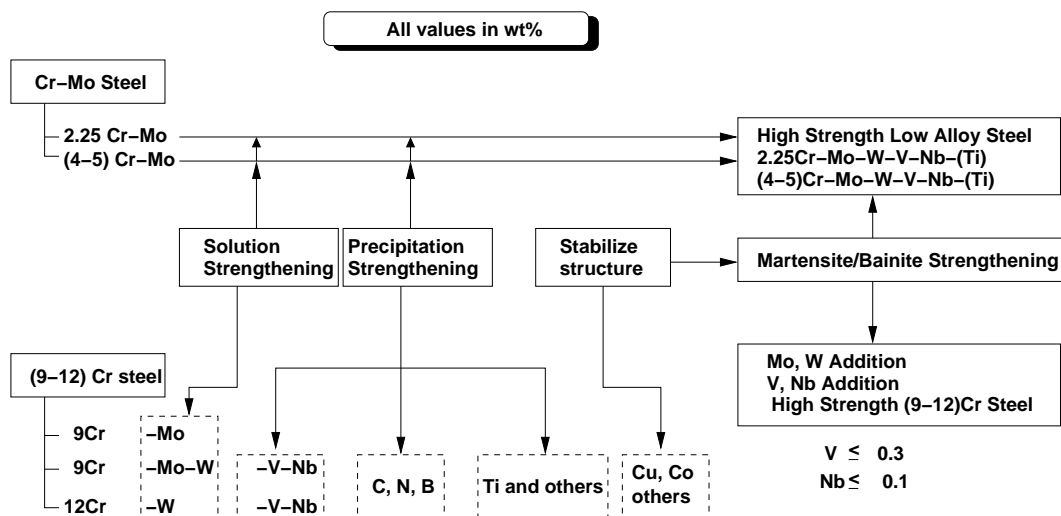


Figure 6.10: Alloy design using the various strengthening mechanisms and structural stability

phases tend to be more uniformly distributed throughout the matrix. In practice this microstructure, which is developed during the normal austenitising and tempering heat treatments, is metastable and subsequently evolves during service exposure at elevated temperatures [112].

Some of the precipitates are short lived (e.g. M_3C), others such as $M_{23}C_6$ last for a long time and some after very long periods in service (Laves phase, Z-phase).

Dissolution of the fine M_2X and MX precipitates generally occur combined with progressive coarsening of $M_{23}C_6$ grain boundary particles with increasing exposure time at temperature. Depending on the alloy composition this may also be accompanied by precipitation of additional coarse particles of M_6X , Laves and Z-phases in the matrix. In addition, reduction in the dislocation densities occur with general recovery and associated subgrain formation [112]. These processes, which are time, temperature and strain dependent, can have significant effects on mechanical properties of the alloy and lead to marked reductions in hardness, tensile and creep strengths during operation. A brief description of the characteristics of precipitates are discussed in the following subsections.

6.2.1 $M_{23}C_6$

This is a Cr-rich carbide capable of containing many metallic elements other than chromium [113].

Like all precipitates $M_{23}C_6$ carbides tend to coarsen during service, causing a deterioration in creep strength. The addition of W can reduce this tendency (Fig. 6.11) [114], by precipitating Laves phase. Laves phase is believed to have a high interfacial energy and hence solute is drawn to Laves phase in preference to $M_{23}C_6$, thus reducing the coarsening rate of the latter [25, 27].

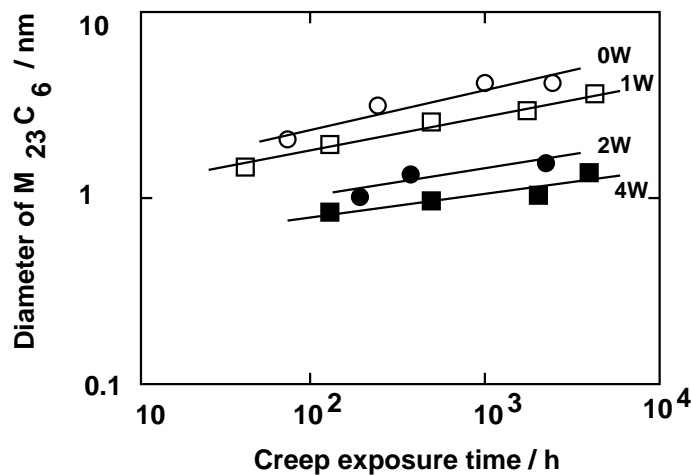


Figure 6.11: Effect of W on coarsening rate of $M_{23}C_6$ carbides during creep of 9Cr-W steel at 600 °C.

6.2.2 Laves phases

The general composition of Laves phase is Fe_2M , where the alloy content may be tungsten, molybdenum or a combination of both [115]. Vanadium, titanium, silicon and cobalt can catalyse Laves phase [110]. Whereas manganese retards the precipitation of Laves phase [116], copper seems to stimulate its nucleation [117]. Laves phase can be detrimental to creep strength if it absorbs solutes which contribute to solution strengthening, which is important for the long term creep strength coarsened microstructures.

6.2.3 M_6C

M_6C is essentially a Mo-rich carbide with a face-centered cubic lattice. In a ternary of Fe-Mo-C alloy, it exists in the composition range Fe_2Mo_4C to Fe_3Mo_3C depending on the overall Mo content (Kuo, 1956). M_6C may also take small quantities of Cr and V into solution. It often forms at grain boundaries, growing rapidly at the expense of surrounding carbides, and nucleating heterogeneously at existing particles [113].

6.2.4 M_7C_3

This is usually a Cr-rich carbide with the trigonal structure of Cr_7C_3 , having a solubility of Fe up to 60 % (although Titch Marsh, 1978 has found that the Cr:Fe ratio can be greater than 1 in 2.25Cr-1Mo-0.15C wt% steel). Mn, V and Mo are also soluble in M_7C_3 . The nucleation of M_7C_3 mostly occurs in the vicinity of cementite or at the cementite/ferrite interface [118], probably because the carbide needs a source of chromium. Cementite particles on the point of dissolving may leave chromium rich regions in which M_7C_3 can precipitate [113, 119].

6.2.5 MX

These occur as small, spherical precipitates that can contain titanium, vanadium and niobium. MX precipitates can be observed in as-quenched material when they remain undissolved during austenitisation [120]. A fine dispersion is obtained by precipitation in the martensite laths, enhancing the creep resistance of the alloy. A calculation done using MTDATA for a 9Cr-1Mo-0.2C-0.05Nb-0.03N-0.1C wt% steel allowing for M_3C , HCP_A3, M_3C_2 , M_7C_3 , $M_{23}C_6$, VN, NbC, NbN, ferrite and austenite to exist, shows that at the normal homogenisation temperature of the 9–12 wt% Cr steels, NbN does not dissolve (Fig. 6.12). The presence of NbN aids in refinement of prior austenite grains as can be seen from Fig. 6.13 [121–123].

6.2.6 Cementite

The composition of this phase is Fe_3C in the iron-carbon system. However, in alloy steels many metallic elements can substitute for iron [124].

6.2.7 M_2X

This phase often precipitates after the formation of cementite with the participation of molybdenum, chromium and vanadium [125]. X is either N or C or both. Precipita-

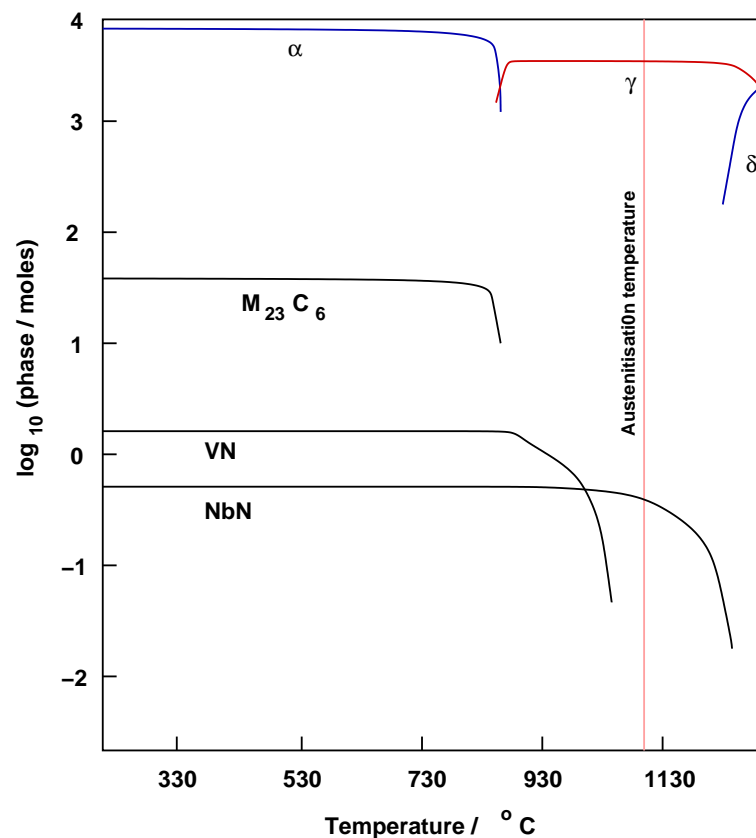


Figure 6.12: Amount of phases in a 9Cr-1Mo-0.2V-0.05Nb-0.03N-0.1C wt% steel.

tion is often accompanied by significant secondary hardening. Table 6.1 summarises the crystallographic characteristics of common precipitates along with the alloying element associated with each precipitate.

At a service temperature of 600 °C a typical 9 wt% Cr steel has $M_{23}C_6$, VN, NbC and NbN as its equilibrium precipitates. Fig. 6.14 is an isopleth of Fe-0.1C-0.2V-1Mo-0.05Nb-0.03N wt% system calculated using MTDATA to show these equilibrium precipitates.

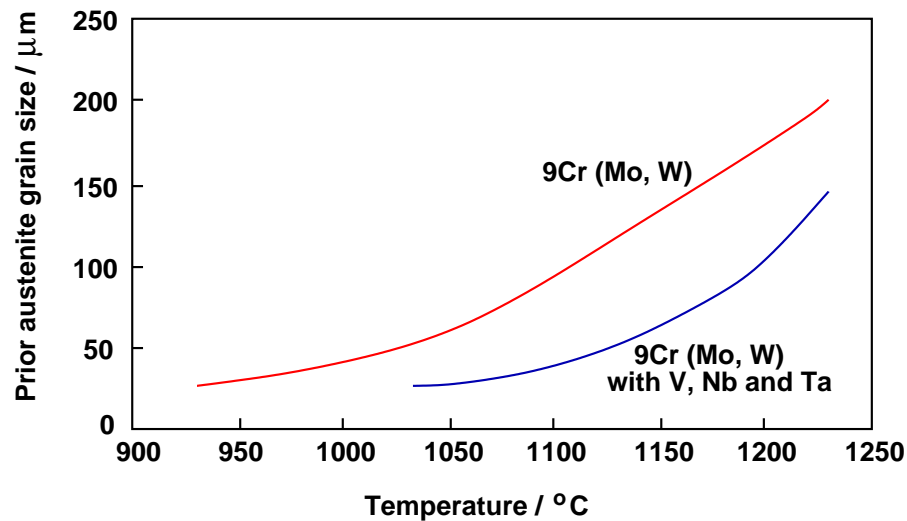


Figure 6.13: Effect of Nb, V and Ta on the prior austenite grain size of a 9Cr-Mo-W wt% alloy held for 1 h at temperature. NbN is the most stable nitride and hence should contribute maximum to the grain refinement.

6.3 Microstructure of Heat-Resistant Steels

The first solidified ingot is given a homogenisation treatment at 1050–1100 °C, which is in the austenitic region of most of the 9–12 wt% Cr steels (Fig. 6.4). When cooled from the austenitising temperature, the room temperature microstructure should consist essentially of ferrite and carbides (Fig. 6.4). But, with the high chromium concentration, the hardenability increases (Fig. 6.15 [87]), leading to a martensitic microstructure with low toughness. A tempering heat treatment is therefore implemented at 600-800 °C. During tempering, new precipitates form so that the final microstructure is tempered martensite with carbides and nitrides.

6.4 Precipitate Stability

Though the precipitates may be able to increase the creep resistance of an alloy to a considerable temperature, they tend to coarsen with increase in temperature or with

Precipitate	Structure	Lattice Parameter/Å	Most Common elements
M_7C_3	Trigonal	$a=13.982, c=4.506$	$M=Cr, Fe, Mo$
$M_{23}C_6$	FCC	$a=10.638$	$M=Cr, Fe, Mo, W; X=C$
M_6C	FCC	$a=11.082$	$M=Mo, W;$
TiC	FCC	$a=4.329$	–
NbC	FCC	$a=4.470$	–
WC	FCC	$a=4.248$	–
NbN [126]	Hexagonal	$a=2.968, c=5.535$	–
VN [126]	FCC	$a=4.09$	–
Laves phases [115]	Hexagonal	$a=4.75-4.83, c=7.69-7.77$	Fe, Cr, Mo, W
M_2X	Hexagonal	$a=2.888, c=4.559$	$M=Cr, V, Nb; X=N, C$
M_3C	Orthorhombic	$a=4.524, b=5.088, c=6.741$	$M=Fe, Cr, Mn$

Table 6.1: Summary of some of the precipitates found in power plant steels which may have an effect on the creep rupture strength.

time leading to a decrease in the creep resistance. The contribution of the diffusive flux and the rate of solute absorption can be derived as discussed from the following section.

6.4.1 The stability parameter

Consider a particulate phase θ in a ferritic matrix α . Let $c^{\alpha\theta}$ be the concentration of solute in ferrite (α) that is in equilibrium with precipitate, θ and $c^{\theta\alpha}$ be the concentration of the solute in the precipitate that is in equilibrium with ferrite. If we consider the precipitate to be spherical then the interface is curved and so the equilibrium concentrations become a function of the radius of curvature given by $c_r^{\alpha\theta}$ and $c_r^{\theta\alpha}$ respectively, where r is the radius of the particle. This is known as the Gibbs-Thompson capillarity effect. This accounts for the cost of creating an interface as the particle grows.

It can be shown that $c_r^{\alpha\theta} > c^{\alpha\theta}$, the inequality becoming greater as $r \rightarrow 0$. In other words, the solute concentration near the small particle will be greater than that near the larger particle, thus setting up the gradient which makes the smaller particle to dissolve

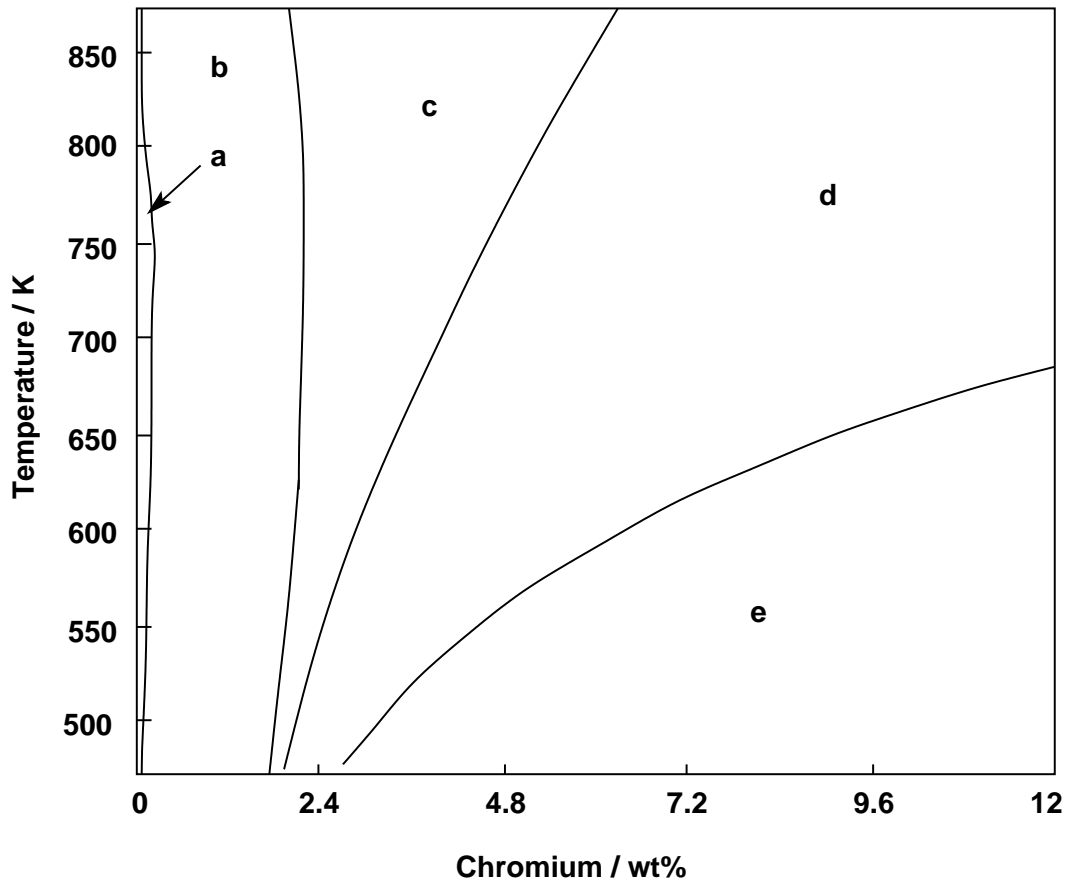


Figure 6.14: Isopleth of Fe-0.1C-0.2V-1Mo-0.05Nb-0.03N wt% steel for varying Cr concentrations with increase in temperature between 473 K (100 °C) and 873 K (600 °C). Regions of the plot showing a) Ferrite + VN + Mo₂C + VC; b) Ferrite + VN + Mo₂C + M₂₃C₆ + NbC; c) Ferrite + VN + M₂₃C₆ + NbC; d) Ferrite + VN + M₂₃C₆ + NbC + NbN; e) Ferrite + VN + M₂₃C₆ + NbN.

and the larger particle to grow (Fig. 6.16 [127]). This is the process of coarsening, driven by the interfacial energy σ_{int} .

The concentration difference $c_r^{\alpha\theta} - c^{\alpha\theta}$ driving the diffusion flux can be given by:

$$c_r^{\alpha\theta} - c^{\alpha\theta} = \frac{\sigma_{int} V^\alpha}{k_{bolt} T r} \times \frac{c^{\alpha\theta} (1 - c^{\alpha\theta})}{c^{\theta\alpha} - c^{\alpha\theta}} \quad (6.1)$$

where k_{bolt} is the Boltzmann constant, T the absolute temperature and V^α the molar volume of ferrite. This flux feeds the growth/dissolution of the particle and hence should match the absorption or desorption of the solute at the interface:

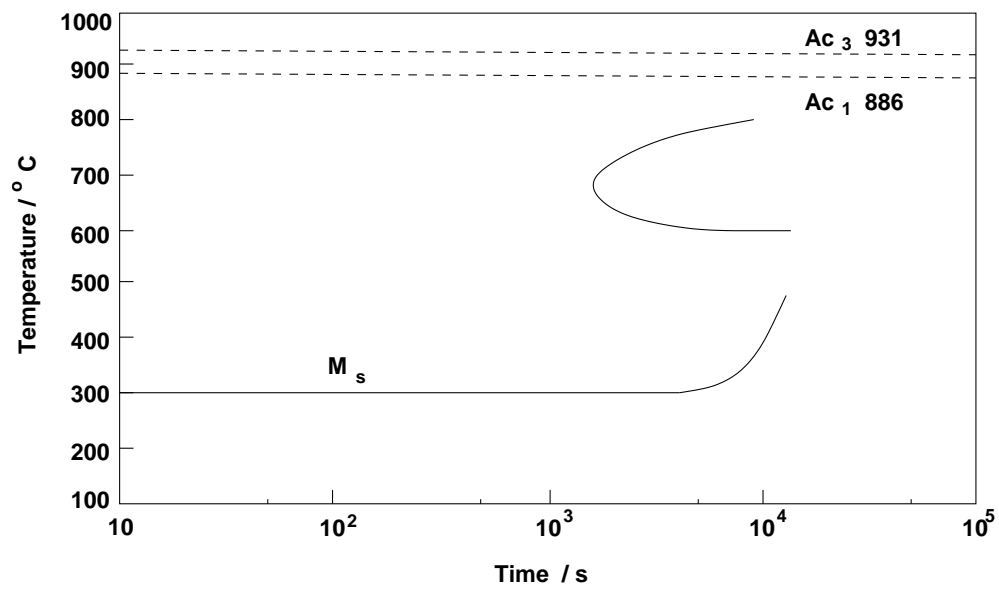


Figure 6.15: Continuous-Cooling Transformation (CCT) diagram of 12Cr-1Mo-1W-V-Nb wt% Steel.

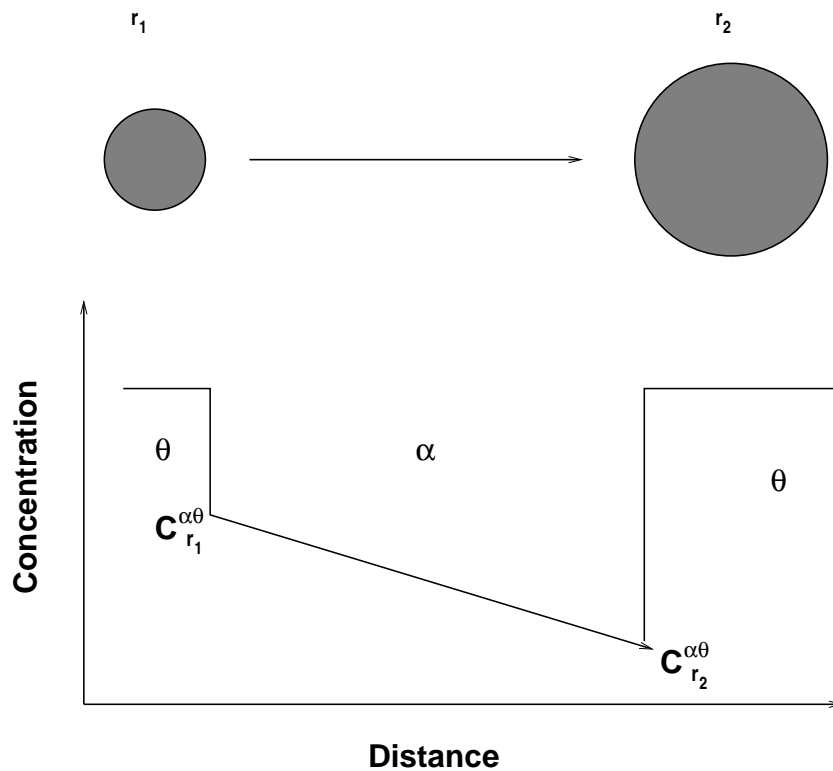


Figure 6.16: An illustration of the capillarity effect driving coarsening

$$\underbrace{D(c_r^{\alpha\theta} - c^{\alpha\theta})}_{\text{measure of flux}} \propto \underbrace{v(c^{\theta\alpha} - c^{\alpha\theta})}_{\text{rate of solute absorption}} \quad (6.2)$$

where D is the diffusivity and v is the interfacial velocity. Now comparing Eq. 6.1 and Eq. 6.2 we get

$$\frac{v}{D}(c^{\theta\alpha} - c^{\alpha\theta}) \propto \frac{\sigma_{int} V^\alpha}{k_{bolt} T r} \times \underbrace{\frac{c^{\alpha\theta}(1 - c^{\alpha\theta})}{c^{\theta\alpha} - c^{\alpha\theta}}}_{\text{stability parameter}} \quad (6.3)$$

From the above equation it is clear that the rate of solute absorption is proportional to the *stability parameter*, which gives the direct measure of coarsening rate. The interfacial velocity v can be deduced as

$$v \propto D \frac{\sigma_{int} V^\alpha}{k_{bolt} T r} \times \underbrace{\frac{c^{\alpha\theta}(1 - c^{\alpha\theta})}{(c^{\theta\alpha} - c^{\alpha\theta})^2}}_{\text{Instability}} \quad (6.4)$$

The Eq. 6.4 deals with just only one solute but Venugopalan and Kirkaldy [128] generalised the theory to deal with many solutes, assuming that the effects of the different fluxes could be combined into a single, effective diffusion coefficient D_{eff} by treating the fluxes as a combination of parallel electrical conductors. And hence the Eq. 6.4 can be rearranged as follows:

$$\frac{1}{v} \propto \frac{1}{D_i} \times \frac{(c_i^{\theta\alpha} - c_i^{\alpha\theta})^2}{c_i^{\alpha\theta}(1 - c_i^{\alpha\theta})} \quad (6.5)$$

where i represents a particular solute. In a multicomponent alloy, the right hand side of Eq. 6.5 is replaced by a summation

$$\frac{1}{v} \propto \frac{1}{D_{eff}} \quad \text{where} \quad \frac{1}{D_{eff}} = \sum_i \frac{1}{D_i} \times \frac{(c_i^{\theta\alpha} - c_i^{\alpha\theta})^2}{c_i^{\alpha\theta}(1 - c_i^{\alpha\theta})} \quad (6.6)$$

6.5 Development of Heat-Resistant Steels

The heat-resistant steels have been developed to have better creep-resistance by the addition of alloying elements. As can be seen from the Fig. 6.17, addition or reduction

in alloying element has resulted in a better rupture strength. EM12, Tempaloy F-9 and T91 are modified 9 wt%Cr steels whose strength have been enhanced by the addition of carbo-nitride forming elements like vanadium and niobium. In this category, NF616 has the highest strength whose design was based on reduction of molybdenum by 0.5 wt% and addition of 1.8 wt% tungsten, and this has shown to have a 30% increase in 10^5 h creep-rupture strength at 600 °C [129]. Due to oxidation and corrosion this category of steels are limited to service below 625 °C.

In the 12 wt% Cr category, HT91 has been used in Europe for extensive periods for superheater tubes, headers and steam pipes. However, because of high carbon content they had poor weldability and also did not have good creep-resistance. But HCM12, with lower carbon content with additional tungsten and niobium had better creep resistance. However, with a disadvantage of poor toughness due to δ -ferrite. The toughness was improved by the addition of copper which suppressed formation of δ -ferrite in HCM12A. Also reduction in molybdenum and addition of tungsten has resulted in higher creep-rupture strength.

Most of the fossil fired power plant in the world are still constructed from low alloy steels like 2.25Cr-1Mo wt%. HCM2S in this category has good weldability and does not require preheating. Addition of tungsten, vanadium and niobium has further increased the creep-strength.

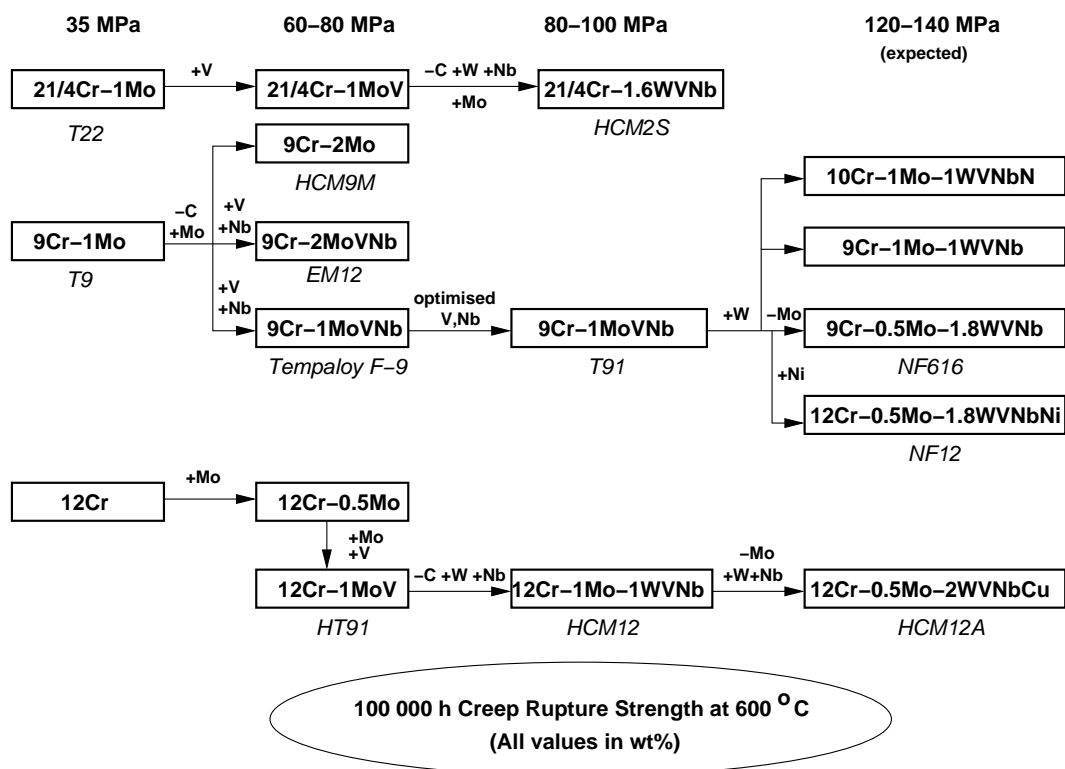


Figure 6.17: Evolution of ferritic heat-resistant steels.

Chapter 7

THE HYBRID MODEL

Neural network models have been successful in the past in the design of creep-resistant steels and weld deposits. However, it has always been difficult, whether using neural networks or other methods, to identify what contributes to creep rupture strength and by how much. In this project, a different approach was adopted to attempt a non-linear factorisation of the long-term creep-rupture strength. This was done by including the equilibrium precipitate fractions and the chemical composition of the residual ferrite in the analysis.

This chapter details the creation of such a *hybrid model*. A hybrid model is one that takes into account the advantage of known physical relationships but which implements them into an empirical framework capable of dealing with complexity. The model itself has rupture time and temperature, composition, heat treatment, precipitate fractions and wt% of dissolved solutes as inputs. By contrast, an *ordinary model* can be thought of as the one having all the inputs other than precipitate fractions and dissolved solutes. The precipitate fraction and wt% dissolved solutes for the hybrid model were estimated using a computer program, Metallurgical and Thermodynamic Data Bank (MTDATA) [69], that is based on CALPHAD (CALculation of PHase Diagrams) method. The following section describes the phase stability calculations used.

7.1 Phase Stability Calculations

7.1.1 System

A solution contains a set of chemical entities known as components; in the present case this includes C, Si, Mn, P, S, Cr, Mo, W, Ni, Cu, V, Nb, Al, N, B, Co, Ta, O and Re. Given these components, a number of phases are then selected in order to investigate those which should be stable under given conditions of temperature and concentration.

7.1.2 Source

Using the system defined, MTDATA [69] determines the compositions and fractions of the phases which lead to an overall minimisation of Gibbs free energy, i.e., to equilibrium. The calculations exploit thermodynamic databases, which contain information about heat capacities, entropy at 298 K and enthalpies of formation. In this case, databases *PLUS* and *SUB_SGTE* were used.

7.1.3 Selection of phases

From the system defined MTDATA computes for all the equilibrium phases. This included M_2X , cementite, M_7C_3 , $M_{23}C_6$, M_6C , Laves phases, NbC, NbN, VN and ferrite. Z-phase was not allowed to exist due to the absence of appropriate thermodynamic database. All other phases were classified as absent. This minimises the computing time.

7.1.4 Calculation of equilibrium precipitates

Since there were some 5420 separate sets of experimental data included in the creep database, the MTDATA program was linked to the database using the *application module* facility of MTDATA serving a FORTRAN computer program which accesses also the creep database. The required phase fractions and compositions could therefore be generated automatically, rather than feeding them individually into MTDATA. The documentation

to the program can be found in the Appendix V.

7.2 Database and Model Construction

The database consists of the precipitate fractions and solutes obtained from the phase stability calculations along with other variables specified earlier. The spread of the data for composition and heat treatment for the 5420 experiments can be found elsewhere in [130], but for the precipitates and solutes, which are of importance here, is presented in Figs 9.3 & 9.4 (Appendix II). The minimum, maximum, mean and standard deviation of the data for these variables are listed in table 9.4 (Appendix II).

Each input variable used in creating the model has an influence on the creep-rupture strength. The parameter σ_w indicates the importance of an input in explaining the variation in the output. Figs 7.1, 7.2 & 7.3 compare the values of σ_w of the inputs for the top four models. A high value of σ_w indicates an important variable, but it can be seen from the Figs 7.1, 7.2 & 7.3 that different models can assign varying significance to the same input. In such cases, it is possible that a committee of models can make more reliable predictions than an individual model.

An optimum committee consisting of 14 models, ranked using the lowest test error, Fig. 7.4, was used to make predictions. The perceived noise level for this committee was found to be $0.016 (\pm 1\sigma)$. The model perceived noise, σ_ν in the creep-rupture stress is illustrated in Fig. 7.5. As expected, σ_ν decreases as the fitting function becomes more flexible with larger numbers of hidden units. By contrast, Fig. 7.6 shows the test error at first decreases and then levels out. A comparison between the predicted (using committee model) and measured values is illustrated in Fig. 7.7. A description of the neural network analysis has already been presented in chapter 4.

The procedure for the factorisation of the creep-rupture strength is illustrated in the

flow chart of Fig. 7.8; it begins with the calculation of phase-fractions and compositions which together with the average composition and temperature are fed into the creep-rupture neural network model. The neural network model is then interrogated to study the influence of each parameter in order to factorise the strength.

It is emphasised that the set of inputs to the neural network are not necessarily independent. For example, the chromium concentration cannot be varied without at the same time influencing the $M_{23}C_6$ carbide. These dependencies were always taken into account in creating the inputs. Note also that the factorisation is non-linear and does not assume any particular relationship between the total creep-rupture strength and its components. This is illustrated with a couple of case studies in the next chapter.

7.3 Predictability of the Model

Though the model is capable of predicting the creep-rupture strength for shorter times, the calculations are performed only for 10^5 h. This is to ensure that the predicted rupture strength corresponds to the one when all precipitates approximate the equilibrium state, which is what MTDATA calculates.

Increase in the number of inputs necessarily does not contribute to any improvement in the accuracy of prediction. However, some authors like Meyer and Gutte have argued that including the equilibrium phase fractions as inputs actually is advantageous in improving the prediction of creep-rupture stress [131]. But, this argument is flawed because the equilibrium phase information is implicit in the average chemical composition and heat-treatment variables. Therefore, a properly constructed network should show no difference in the accuracy of prediction with or without equilibrium phase fractions. Fig. 7.9 compares calculated creep rupture stress for a selection of alloys (composition listed in table 7.1), as a function of time. Notice that in this case, the hybrid model has

been used for estimating even for times much lower than 10^5 h, where precipitation is not expected to be at equilibrium. Nevertheless, the non-linearity inherent in the neural-network method allows the hybrid model to estimate the rupture stress to the same level of accuracy as the ordinary model. This is because it incorporates all the variables of the ordinary model (composition, rupture time, temperature and heat treatment).

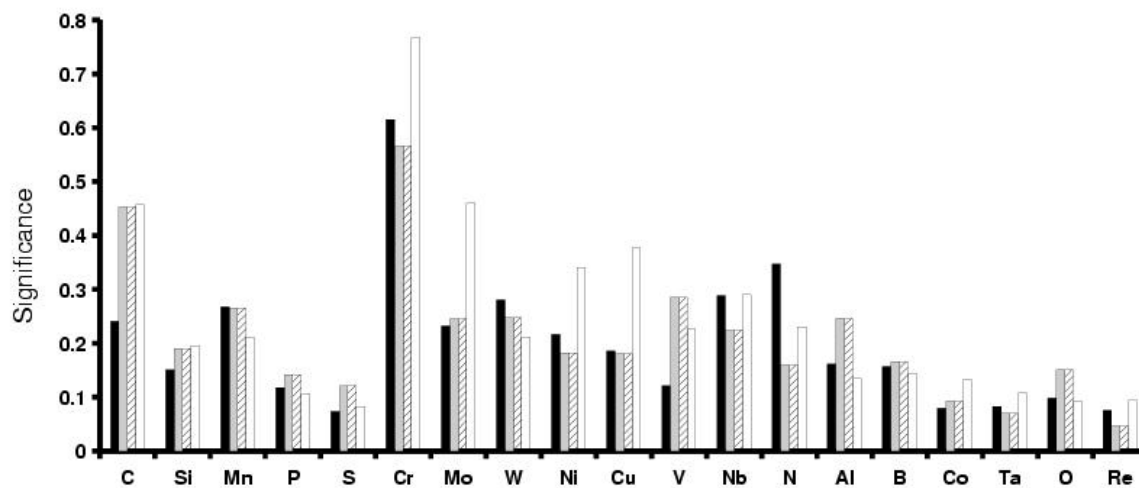
	2.25Cr-Mo	NF616	HCM12A
C	0.12	0.106	0.12
Si	0.29	0.04	0.04
Mn	0.5	0.46	0.63
P	0.018	0.008	0.013
S	0.018	0.001	0.001
Cr	2.25	8.96	10.75
Mo	0.96	0.47	0.39
W	0.01	1.87	1.92
Ni	0.027	0.06	0.28
Cu	0.05	—	0.9
V	0.01	0.2	0.21
Nb	0.005	0.069	0.04
N	0.0099	0.051	0.062
Al	0.004	0.007	0.001
B	—	0.001	0.001
Co	0.05	0.015	—
Ta	—	—	—
O	0.01	0.01	
Re	—	—	—

Table 7.1: Composition of 2.25Cr-1Mo wt%, NF616 and HCM12A.

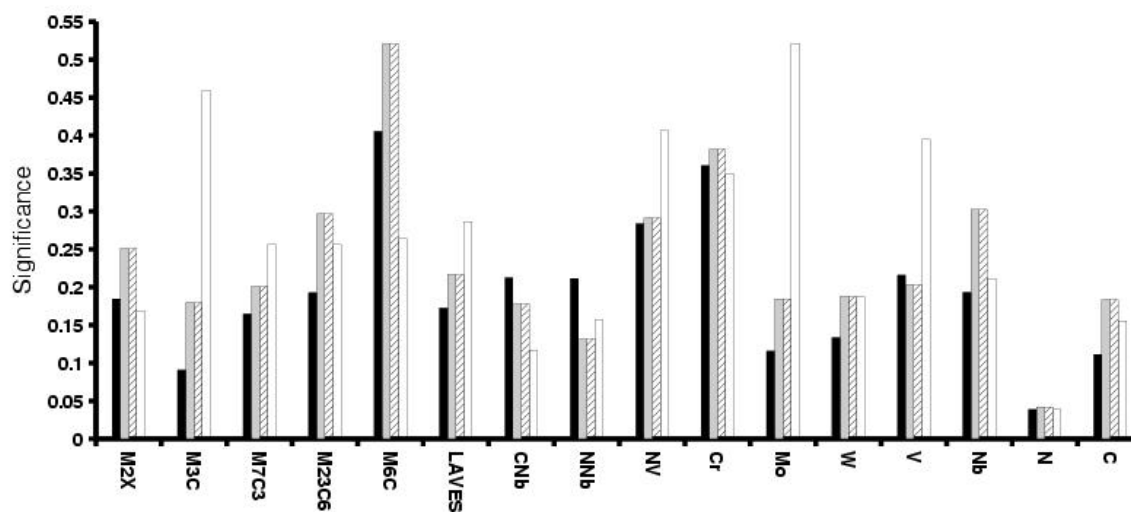
Our aim in increasing the number of variables was not to increase the accuracy of creep-rupture stress estimation, but rather to reveal the effects of individual phases on the stress, i.e., to deconvolute the components of the creep-rupture stress. One further difference which emerges from our aim is that the solution strengthening components are also examined.

7.4 Summary

A neural network was created after training a dataset containing 5420 data-lines with 53 input variables. The network consisted of 14 models to form a committee, with a maximum perceived noise level of ± 0.016 (1σ). The input variables included composition, heat treatment parameters, precipitate fractions and dissolved solutes. Though the models are capable of extending their predictability for lower times, it is emphasised that all the predictions made using the models were resorted to 10^5 h, so that precipitates have evolved to equilibrium. The aim of this hybrid model was to deconvolute the influence of precipitates and dissolved solutes on the creep–rupture strength, and not to increase the accuracy of its prediction. The application of this model is described in the following chapter.



(a)



(b)

Figure 7.1: Influence of alloying elements, precipitates and dissolved solutes on the creep-rupture strength of ferritic-steels. The four bars with different colours represent the significance of the input as seen by each of the four best models.

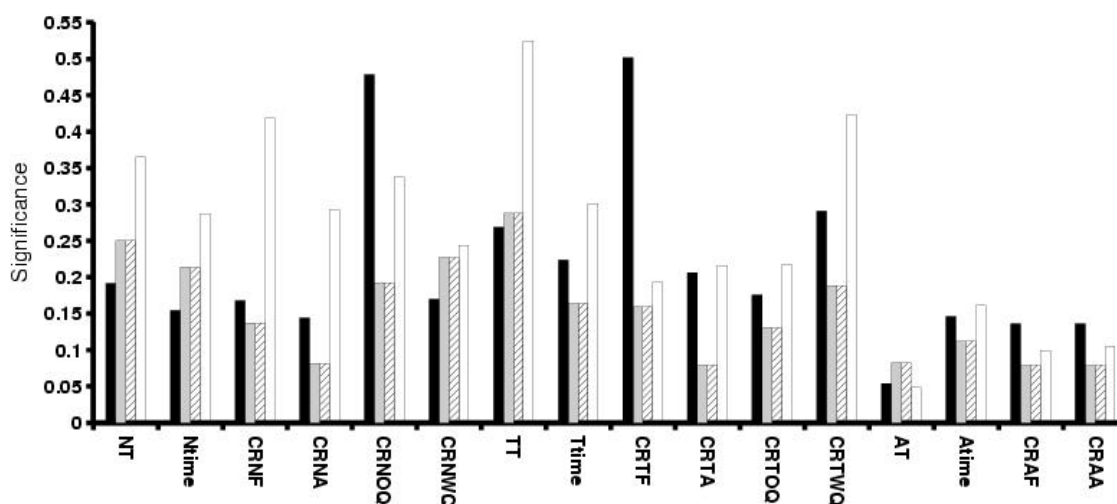


Figure 7.2: Influence of heat treatment parameters on the creep-rupture strength of ferritic-steels. NT:Normalising Temperature; Ntime: Normalising time; CRNF, CRNA, CROQ and CRWQ are Cooling Rate after Normalising in Furnace, Air, Oil and Water respectively; TT: Tempering Temperature; Ttime: Tempering time; CRTF, CRTA, CRTQ and CRTWQ are Cooling Rate after Tempering in Furnace, Air, Oil and Water respectively; AT: Annealing Temperature; Atime: Annealing time; CRAF and CRAA are Cooling Rate after Annealing in Furnace and Air respectively.

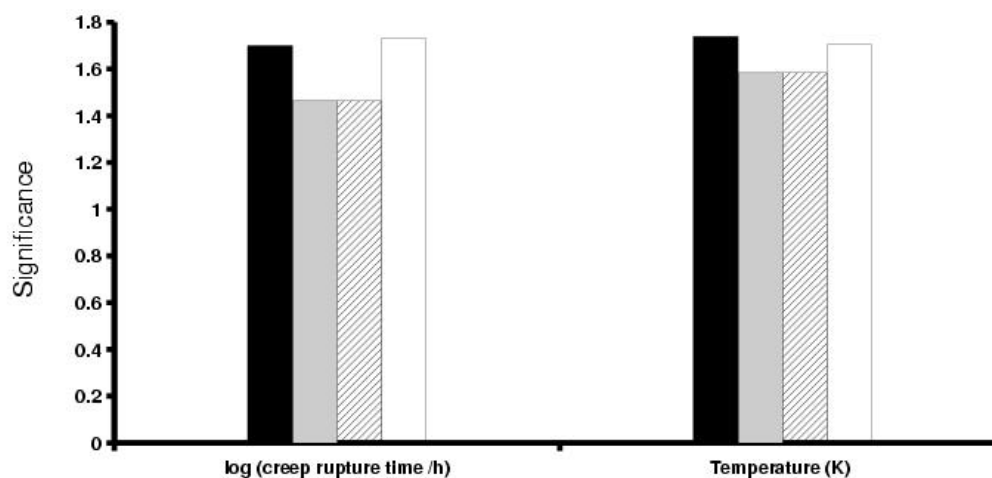


Figure 7.3: Influence of rupture time and service temperature on the creep-rupture strength of ferritic-steels.

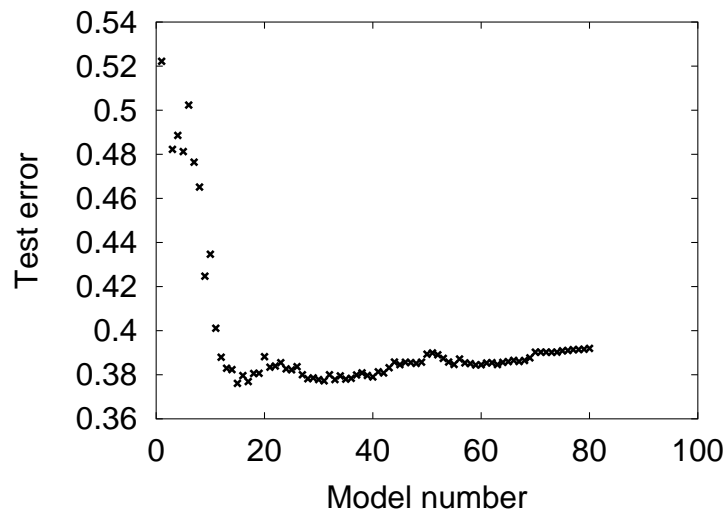


Figure 7.4: Variation in test error with the number of models in the committee.

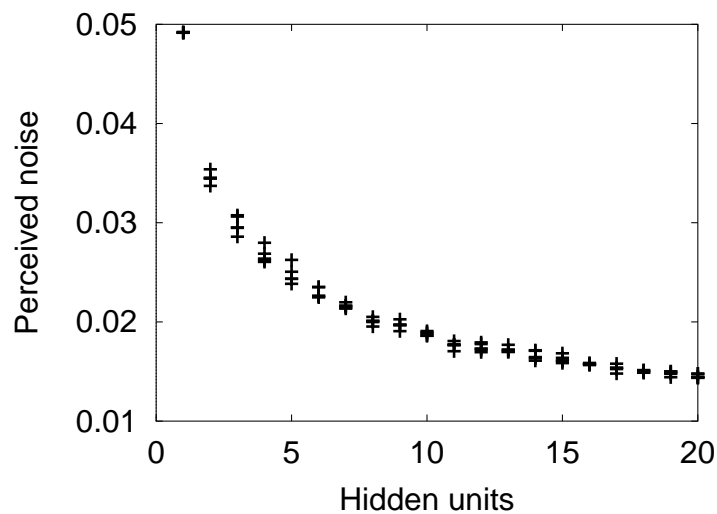


Figure 7.5: Variation in σ_ν as a function of the number of hidden units. Several values are presented for each set of hidden units because the training for each network started with a variety of random seeds.

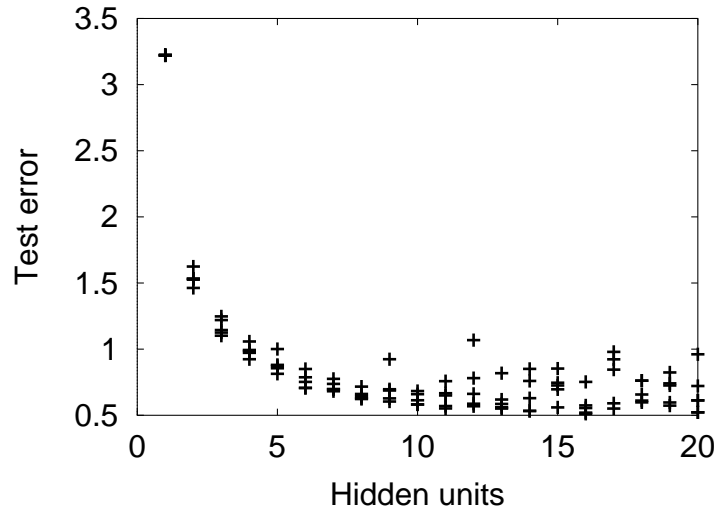
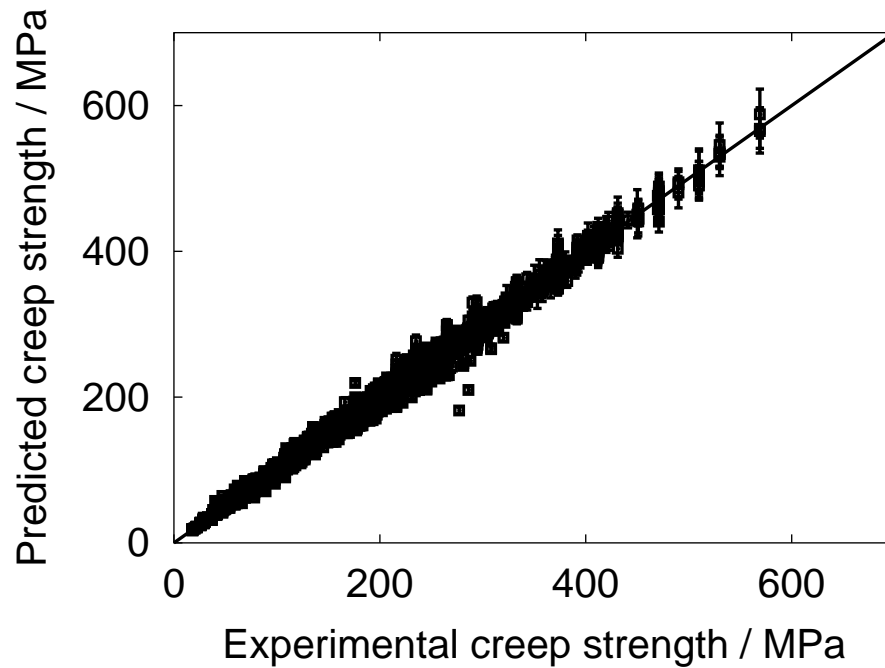


Figure 7.6: Test error as a function of the number of hidden units.



(a)

Figure 7.7: Comparison between the calculated and measured creep–rupture strength for 5420 separate experiments. The calculations were done using the complete dataset following a retraining procedure once the appropriate set of models which form the committee were selected.

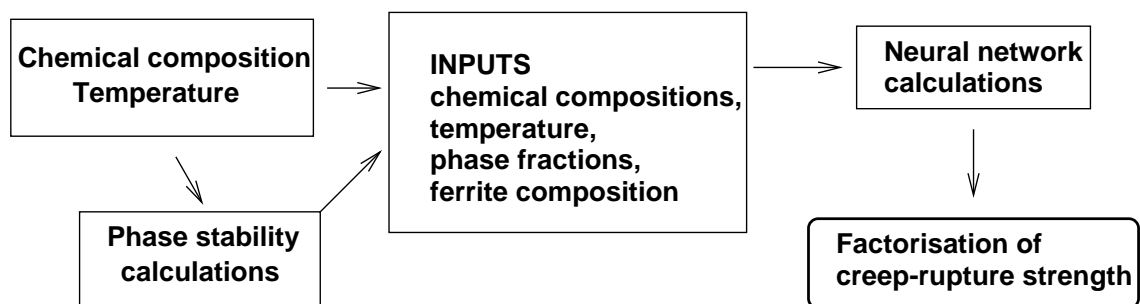


Figure 7.8: Flow-chart showing the method for factorising creep-rupture strength.

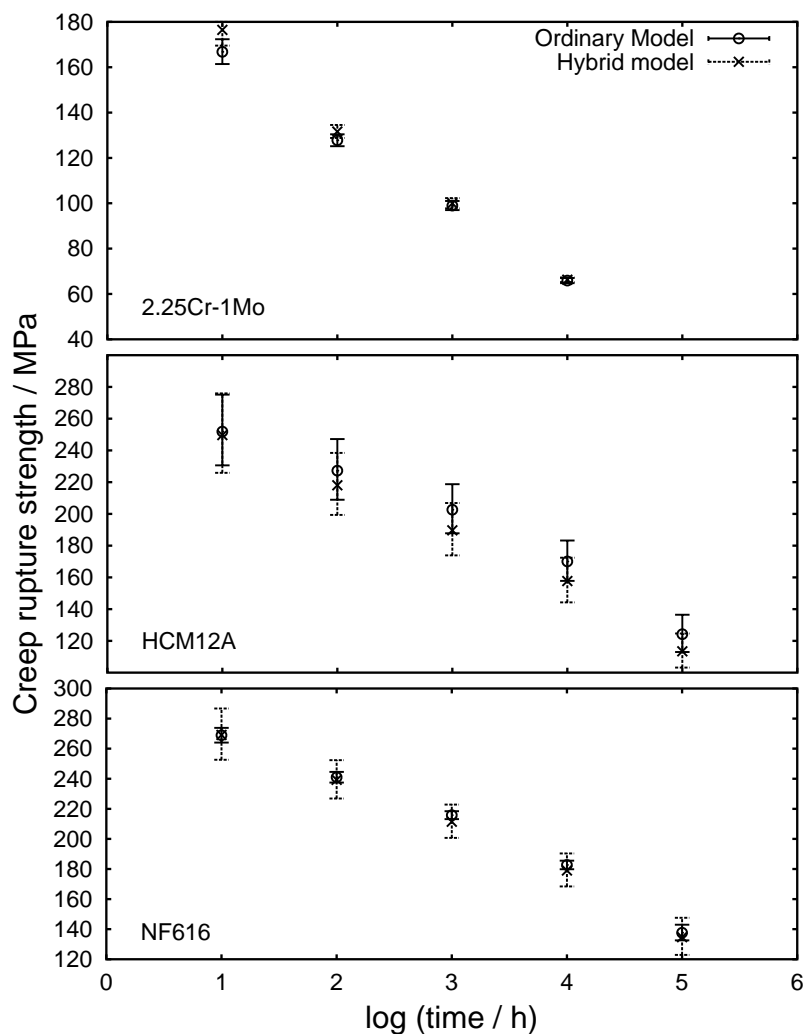


Figure 7.9: Comparison of predictability of a hybrid model and an ordinary model. Creep strength was estimated at 600 °C. Composition of the alloys is listed in table 7.1. 2.25Cr–1Mo wt% was normalised at 920 °C for 1 h and cooled in air, followed by a tempering treatment at 640 °C for 1.5 h with subsequent air cooling. NF616 and HCM12A were normalised at 1070 °C for 1 h and cooled in air, tempered at 770 °C for 1 h and cooled in air.

Chapter 8

FACTORISATION OF THE CREEP STRENGTH OF $2\frac{1}{4}\text{Cr}-1\text{Mo}$, NF616 and HCM12A

The steels used in power plants have considerably evolved with better properties like good creep resistance, better corrosion and high temperature oxidation resistance. $2\frac{1}{4}\text{Cr}1\text{Mo}$ has been one of the most widely used heat resistant steels. The creep-resistance in this steel is thought to be due to molybdenum carbide. But yet, not much has been known about the amount of its contribution to the total creep-strength of the alloy.

Further, the most recent class of tungsten alloyed high chromium steels like NF616 and HCM12A have even better creep-resistance than $2\frac{1}{4}\text{Cr}1\text{Mo}$ steel. Again, it is not known how much of the total strength contribution comes from each of the precipitates, dissolved solutes and microstructure.

In this chapter, case studies of three heat-resistant steels are presented, with the aim of quantifying the contributions to the creep-rupture strength due to precipitates, dissolved solutes and microstructure. One of the steels was selected for study because it is a well-established material, whereas the other two are modern variants which are the subject of much discussion.

8.1 Case Study: $2\frac{1}{4}\text{Cr}1\text{Mo}$ Steel

$2\frac{1}{4}\text{Cr}1\text{Mo}$ heat-resistant steels are widely used in power plant with steam temperatures upto a temperature of $565\text{ }^{\circ}\text{C}$ [98, 132]. They are not suitable for higher steam-temperatures because both the creep and oxidation resistance becomes inadequate. For example, at $600\text{ }^{\circ}\text{C}$ and 10^5 h , the creep rupture strength is only 35 MPa [26].

The calculations presented here are for a steel of typical composition (table 7.1); the austenitisation temperature was 1343 K for 1 h followed by tempering at 1043 K for 1 h . In all cases the sample was assumed to have been cooled in air from the heat treatment temperature. Fig. 8.1 shows the results for at $550\text{ }^{\circ}\text{C}$, 10^5 h creep-rupture time, as a function of the molybdenum concentration. It is interesting that within the shaded regions, the only parameter which varies significantly with the total molybdenum concentration is the amount of molybdenum in solution in the ferrite. Therefore, by comparing the dissolved molybdenum data in the shaded region with corresponding calculations of the creep-rupture strength in the lower half of the diagram it is possible to estimate the contribution of dissolved molybdenum to the creep-rupture strength at $550\text{ }^{\circ}\text{C}$ and 10^5 h . This turns out to be $\Delta\sigma_{\text{Mo}_{ss}} = 22\text{ MPa/wt\%}$.

Note that this is not the same as solid-solution strengthening as measured in ordinary tensile tests, but rather some complex mechanism by which dissolved molybdenum influences creep deformation. There is diffusion and dislocation climb involved in creep processes whereas tensile deformation involves essentially the glide of dislocations. It is expected that the effect of a solute on tensile and creep deformation should show some correlation but for the reasons described, the effects will not be identical. A study is presented in Appendix III, where the hot-strength is compared with the creep-strength of $2\frac{1}{4}\text{CrMo}$ steel.

For the specific composition of $2\frac{1}{4}\text{CrMo}$ steel given in table 7.1, *i.e.* 0.96 wt\% of total molybdenum and $\text{Mo}_{ss} = 0.32\text{ wt\%}$, the contribution of the latter to the creep-

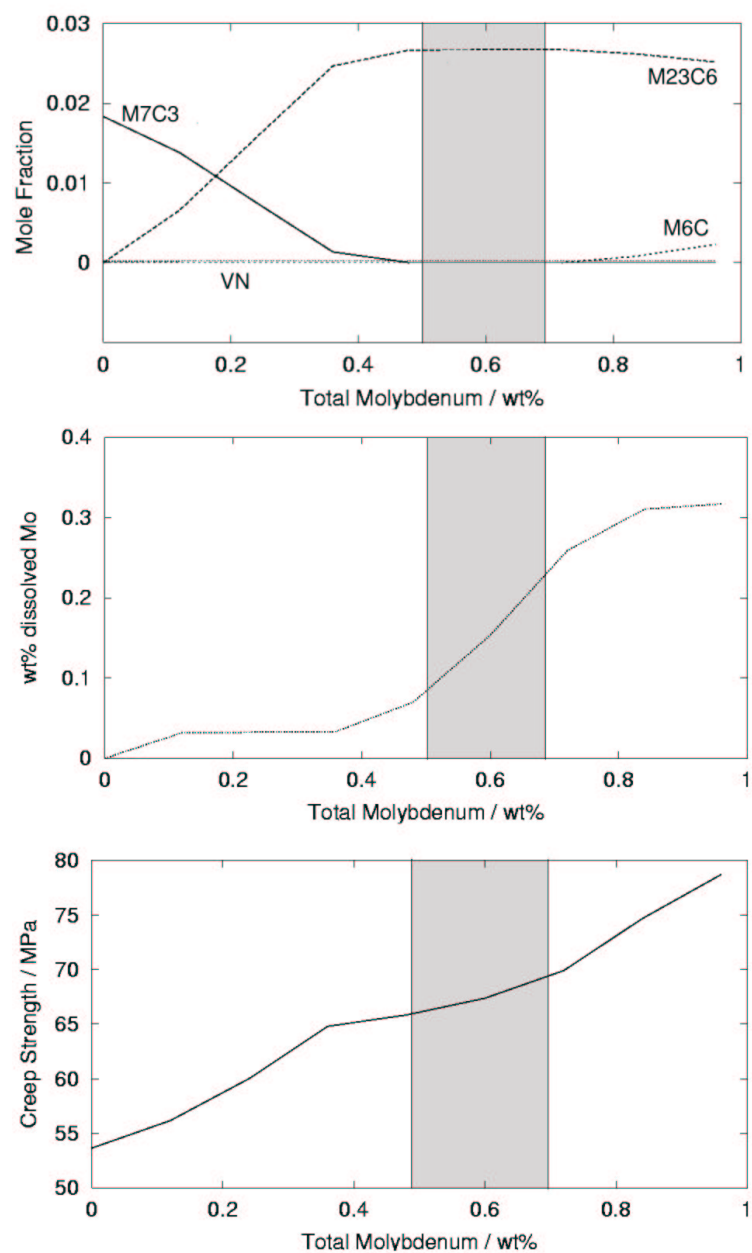


Figure 8.1: The shaded regions represent total molybdenum concentrations where only the amount of molybdenum in solution is changing significantly. The calculations are for $2\frac{1}{4}\text{CrMo}$ steel at $550\text{ }^{\circ}\text{C}$ for creep-rupture time of 10^5 h .

rupture strength is about 7 MPa. Similar calculations gave the contribution of dissolved molybdenum to the creep–rupture strength at 600 °C and 10⁵ h to be 15 MPa/wt% (this compares with 22 MPa/wt% at 550 °C). Therefore, as expected, the creep–strengthening effect of a unit concentration of dissolved molybdenum decreases as the temperature increases. However, the actual contribution in the 2 $\frac{1}{4}$ CrMo steel considered does not decrease significantly because the amount of molybdenum in solution increases. The results are summarised in table 8.1.

Temperature / °C	$\Delta\sigma_{Mo_{ss}}$ / MPa wt% ⁻¹	Mo _{ss} / wt%	$\Delta\sigma_{Mo_{ss}} \times Mo_{ss}$ / MPa
550	22	0.32	7.0
600	15	0.43	6.3

Table 8.1: Summary of the effect of molybdenum dissolved in ferrite on the 10⁵ h creep–rupture strength of 2 $\frac{1}{4}$ Cr1Mo steel.

It was not possible to do the same kind of analysis for the effect of chromium because there was no domain in which the effect of dissolved chromium could be studied in isolation. However, it is clear from Fig. 8.2 that even in ordinary tensile deformation the effect of chromium in solid–solution becomes negligible at elevated temperatures as illustrated from the work of Leslie [34].

The effect of vanadium is particularly interesting, as illustrated in Fig. 8.3, bearing in mind that vanadium has a strong affinity for nitrogen. As the total vanadium concentration is increased beyond 0.005 wt%, V_{ss} does not change, neither does NbN, but the amount of VN increases at the expense of M₂X (Cr₂N). In spite of the latter, the creep–rupture strength increases indicating that VN is a better creep–strengthenener than M₂X. It is legitimate therefore to attribute the increase in creep–strength (Fig. 8.3) due to the addition of vanadium, to vanadium nitride alone. The contribution is of course, a complex term due to formation of VN, solution strengthening from V_{ss} and a loss due to Cr₂N dissolution, but the net effect in this alloy is a gain of 4.8 MPa at 550 °C and of 2 MPa at 600 °C.

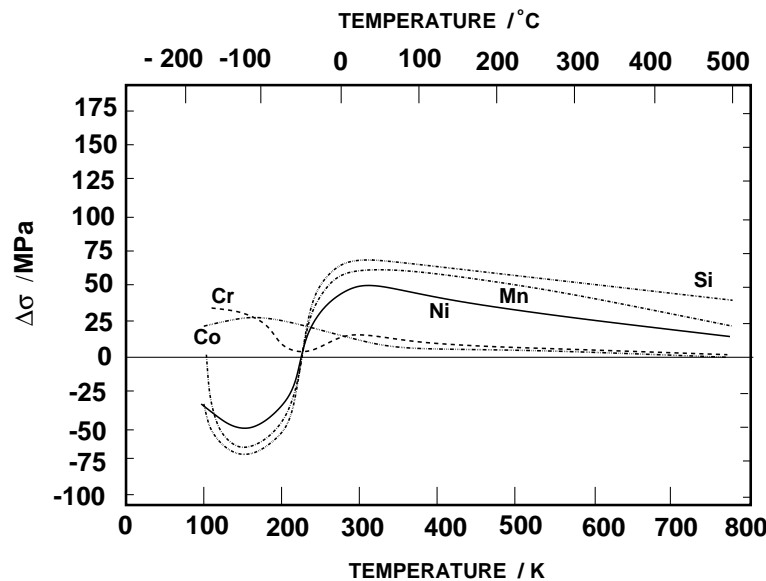


Figure 8.2: Solid-solution hardening and softening in iron-base alloys, adapted from Leslie [34].

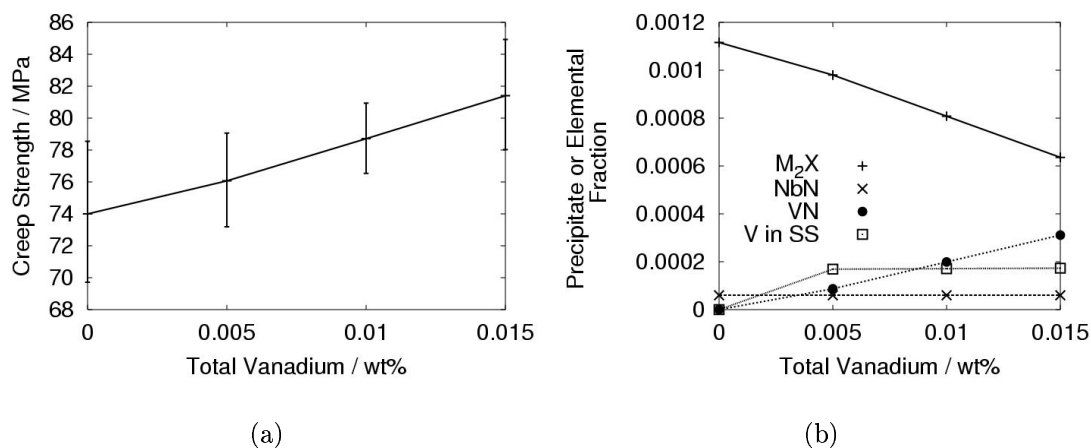


Figure 8.3: Precipitate fractions, and creep strength, as a function of total vanadium concentration, of $2\frac{1}{4}\text{Cr}1\text{Mo}$ steel for a creep-rupture time of 10^5 h at 550°C .

The influence of precipitates on the creep-strength can in principle be deduced as follows. The key elements to consider with respect to precipitation are chromium, molybdenum and vanadium. Vanadium can be ignored in this analysis because total effect of vanadium has been identified separately. The solid-solution strengthening ef-

fect of chromium has been shown to be negligible and therefore its entire contribution must be attributed to precipitate strengthening. Molybdenum does cause a solid-solution strengthening, but this has been quantified and therefore can be excluded from its contribution due to precipitation. Therefore the contribution due to precipitates resulting from Cr and Mo can be calculated as the increase in creep-rupture strength on adding $2\frac{1}{4}$ Cr and 1 Mo wt% to the Cr- and Mo-free alloy less the solid-solution strengthening due to Mo.

Fig. 8.4 illustrates the variety of contributions to the creep-rupture strength; the diameters of the pie-charts have been scaled to reflect the 10^5 h creep-rupture strength at the appropriate temperature. The term microstructure excludes the precipitation and is intended to refer to cell boundaries and lath boundaries. It is particularly noticeable that the role of precipitate strengthening as a proportion of the total strength decreases sharply as the temperature is increased. This is hardly surprising, given the smaller equilibrium fraction of precipitates at higher temperatures and their greater coarsening rates, information which is implicit in neural network analysis.

It is noteworthy that the degree of factorisation illustrated in Fig. 8.4 is far from complete. Ideally, it would be desirable to know the contributions from each of the variety of precipitates present in the microstructure. For example, it is commonly stated that in $2\frac{1}{4}$ Cr1Mo steels, it is the Mo_2C which is the most important precipitate to resist creep deformation. It has not been possible to prove this with the present analysis because of the fraction of Mo_2C cannot be varied independently without altering all the other precipitates. We should not be disheartened with this negative conclusion because it proves that it is not even experimentally possible to obtain this information, other than by direct characterisation of precipitate-dislocation interactions.

Components	Strength Contributions / MPa	
	550 °C	600 °C
Molybdenum in solid solution	6.97 (9 %)	6.32 (21 %)
Total Vanadium	4.78 (6 %)	2.07 (6 %)
Precipitates	17.78 (23 %)	3.21 (11 %)
Fe, microstructure and other SSS	49.08 (62 %)	18.89 (62 %)
Total strength at temperature	78.69	30.49

Table 8.2: Creep-rupture strength contributions from different components of $2\frac{1}{4}\text{CrMo}$ steel. Numbers in brackets represent percentage strength contributions. Note that some molybdenum goes into solution and is a major component of rupture strength at 600 °C.

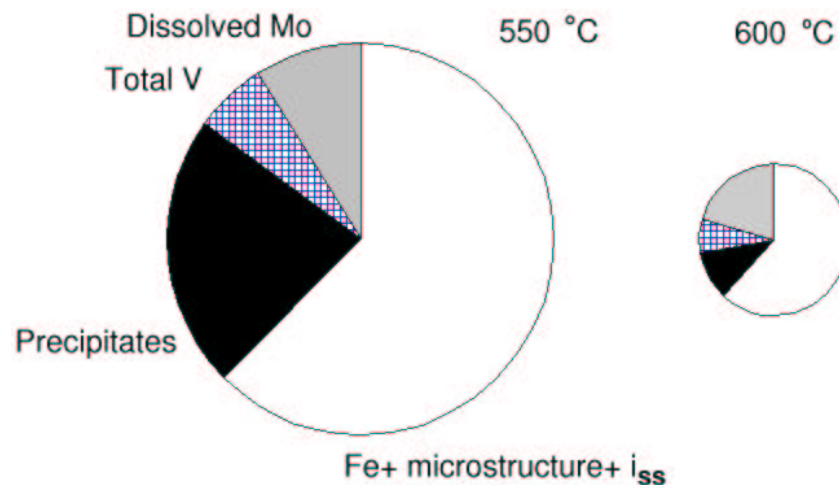


Figure 8.4: Pie charts showing the factorisation of the 10^5 h creep-strength of $2\frac{1}{4}\text{CrMo}$. The diameters of the pie charts have been scaled to reflect the 10^5 h creep-rupture strength at the appropriate temperature. The term i_{ss} represents the contributions to the creep-rupture strength due to dissolved solutes other than molybdenum and vanadium.

8.2 Case Study: NF616 Steel

NF616 is a high-chromium creep-resistant martensitic steel intended for service at a temperature of 600 °C. It comes under the category of tungsten-alloyed high-chromium

steels. Its chemical composition is listed in table 7.1. The analysis presented here is when the alloy is normalised at 1343 K for 1 h followed by air cooling to ambient temperature, tempering at 1043 K for 1 h followed by air cooling. Notable features about NF616 include its tungsten and vanadium concentrations, and the presence of Laves phase in the microstructure. At 600 °C after 10^5 h the creep rupture strength of NF616 is predicted to be 133 ± 5 MPa, which correlates well with the measured value of 135 MPa [26, 75].

Fig. 8.5 shows an interesting synergistic effect between tungsten and vanadium in NF616, whereby the strengthening effect of V depends on the W concentration. It has been verified using MTDATA that this synergy cannot be explained on the basis of variations in the equilibrium phase-fractions or phase compositions. The reasons are not clear but it is speculated that they could be related to phenomena such as diffusion. In any event, the creep-rupture strength of the 0.2V–1.84W alloy is calculated to be 133 MPa whereas the removal of W gives the strength of 0.2V–0W to be 91 MPa. Therefore, the total contribution of W to the 10^5 h creep-rupture strength is $133 - 91 = 42$ MPa (table 8.3). Given this value and Fig. 8.5, and the creep-rupture strength for a 0V–1.84W (31 MPa) alloy and 0.2V–1.84W (133 MPa) alloy, the total contribution of V equals $133 - 42 - 31 = 60$ MPa (table 8.3). The total effect of Mo was obtained similarly. There is no significant effect of niobium on the creep-rupture strength at 600 °C (Fig. 8.10). Another observation is that the location of NF616 on the contour plot shown in Fig. 8.11 indicates optimum design.

The contribution of vanadium can be further factorised because there is a regime of alloy composition where the vanadium in solid-solution, V_{ss} , varies independently of other variables (Fig. 8.8). The results from this factorisation are also presented as contributions due to V_{ss} and VN in table 8.3. It is evident that VN plays a major role in the creep properties of NF616. This agrees with studies made by Mimura *et al.*, that vanadium additions are aimed at precipitation strengthening in NF616 [75]. Similarly, W_{ss} can be estimated using Fig. 8.5 & 8.6 so that the contribution from Laves phase amounts to

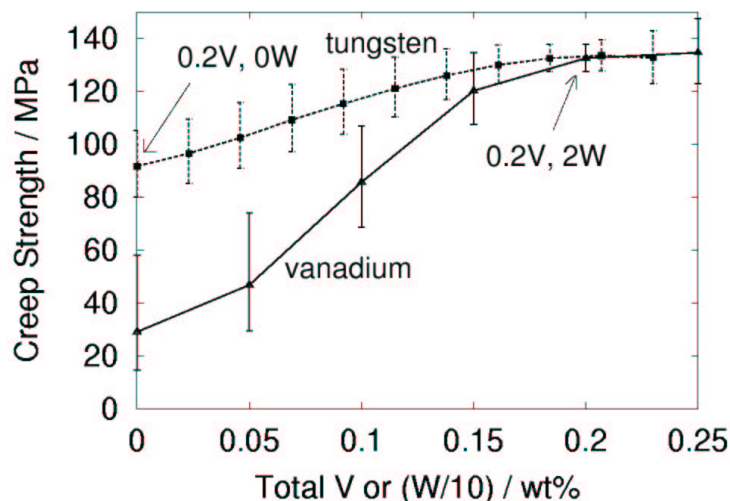


Figure 8.5: Synergistic effect of tungsten and vanadium on the creep-rupture strength of NF616.

	Strength / MPa	Percentage
Creep Rupture Strength	133.0	100
Fe + microstructure + i_{ss}	18.9	14
Total from tungsten	42.0	32
Total from vanadium	60.0	45
Total from molybdenum	12.0	9
Total from V_{ss}	13.0	-
Total from VN	47.0	-
Total from W_{ss}	16.7	-
Total from Laves phase	25.3	-

Table 8.3: Creep-rupture strength contribution from the individual components to the total creep strength of NF616.

25.3 MPa. This agrees qualitatively with claims in the literature that Laves phase makes an important contribution to the strength of NF616.

It is reasonable to assume that the contribution to the creep-rupture strength from iron and the microstructure should be similar to that of $2\frac{1}{4}\text{Cr1Mo}$ steel. The pie-chart in Fig. 8.12 gives summary of the contributions made by the different components of NF616 to its 10^5 h creep-rupture strength at 600°C .

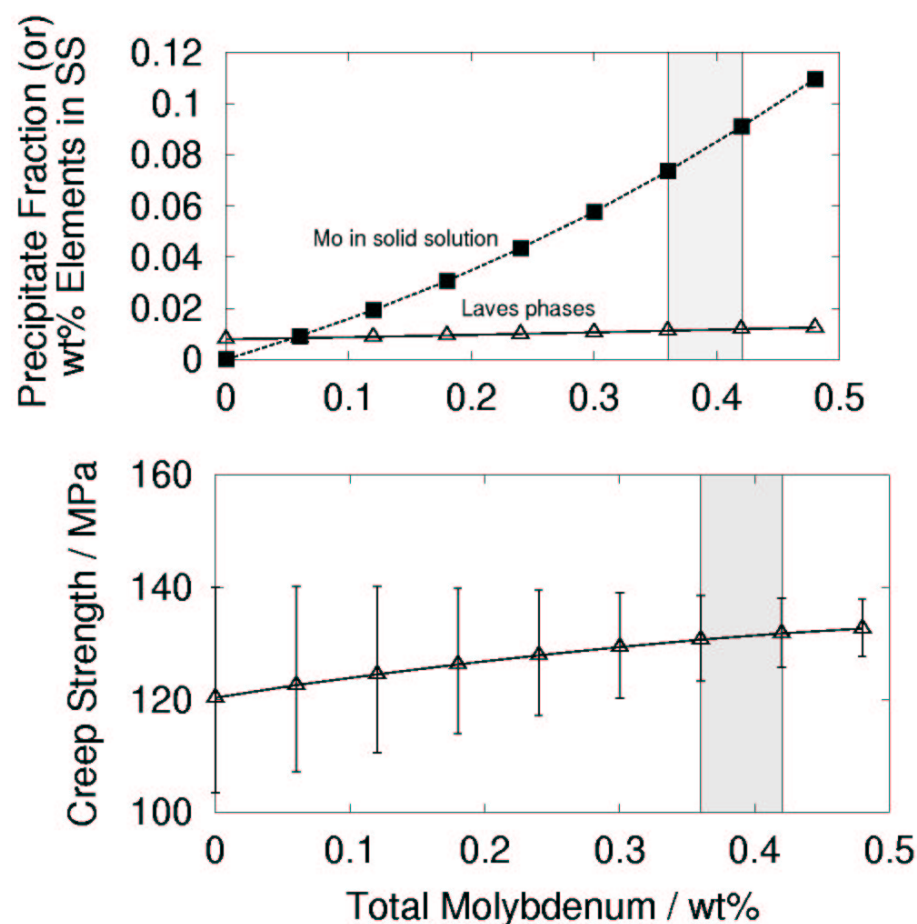


Figure 8.6: Precipitate fractions, and 10^5 h creep strength of NF616 at 600 °C.

8.3 HCM12A

HCM12A is a high-chromium creep-resistant martensitic steel intended for use in the temperature range of 600 °C as a power plant material. Its chemical composition is given in table 7.1.

The alloy is categorised as a tungsten alloyed heat-resisting steels with a notably low molybdenum content than its predecessor HCM12 [26]. Alloying with tungsten can result in formation of Laves phases which might hinder the coarsening of $M_{23}C_6$ [114,133].

A higher chromium concentration increases the tendency to form a stable δ -ferrite,

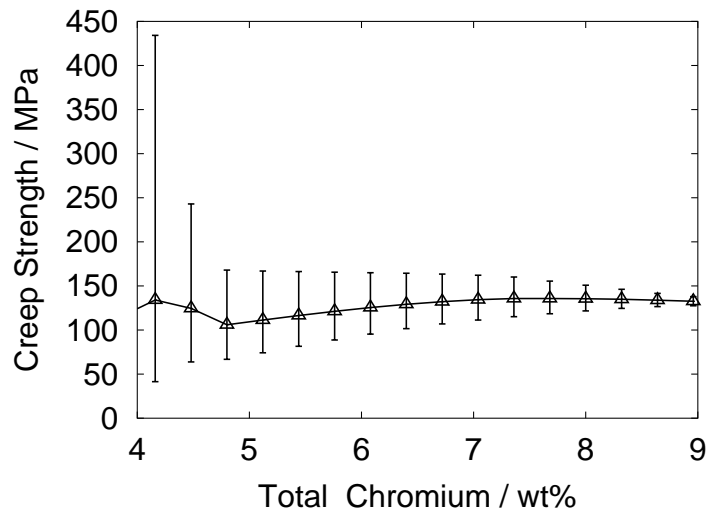


Figure 8.7: 10^5 creep-rupture strength is not significantly influenced by the presence of chromium at 600 °C.

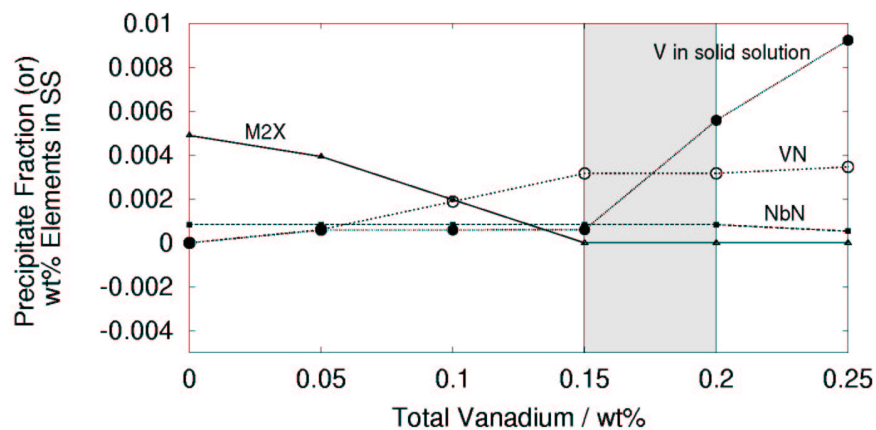


Figure 8.8: Precipitate fractions and wt% of vanadium in solid solution of NF616 at 600 °C. Note that over the concentration range 0.15–0.2 wt% it is only the amount of vanadium in solution that varies significantly. This domain can therefore be used to estimate $\Delta\sigma_{ss}^V$.

thus decreasing the toughness (Fig. 6.4). Addition of copper decreases the formation of this δ -ferrite.

Published calculations of the phase diagram of HCM12A [90] indicate the presence of M_2X (identified in CALPHAD notation as HCP_A3) as an equilibrium phase at the temperature of interest. However, investigation revealed that the prediction of M_2X is

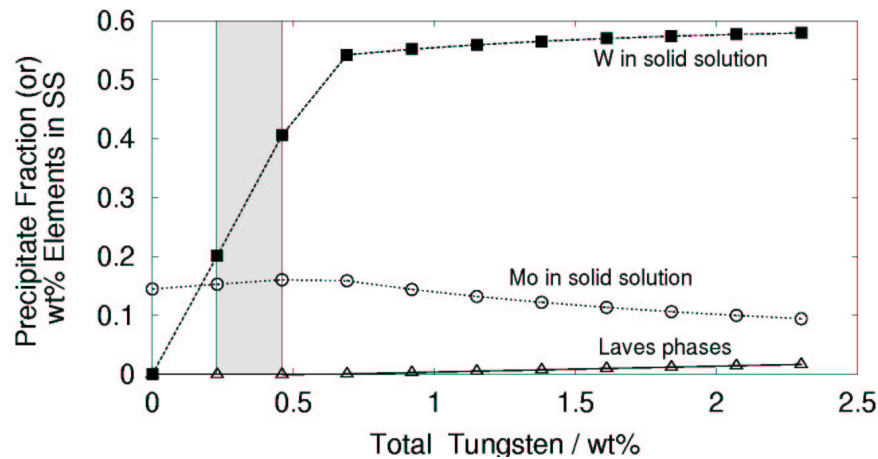


Figure 8.9: Precipitate fractions, and creep strength of NF616 after 10^5 h at 600 °C. Note that over the concentration range 0–0.5 wt% it is only the amount of tungsten in solution that varies significantly. This domain can therefore be used to estimate $\Delta\sigma_{ss}^W$.

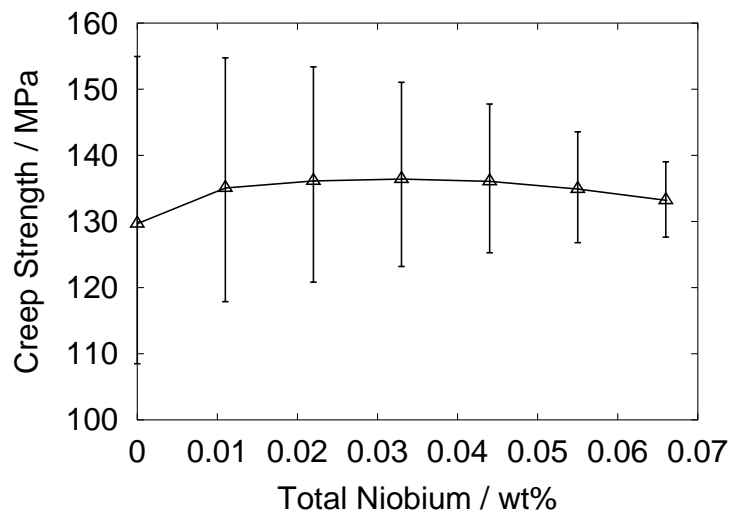


Figure 8.10: Precipitate fractions, and creep strength of NF616 after 10^5 h at 600 °C.

an artifact since FCC (face-centered cubic) or copper as a phase is excluded when conducting calculations below Ae_1 temperature. This is acceptable for most steels, but not for HCM12A which contains copper, which precipitates as an FCC phase. Excluding FCC in the computation results incorrectly in HCP_A3 copper. Various phases existing

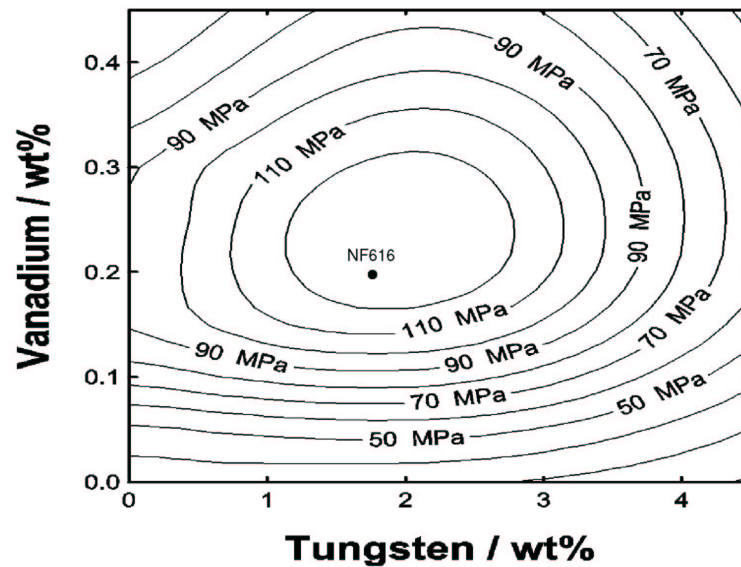


Figure 8.11: Contour plot showing the variation in creep-rupture strength at 600 °C, when concentrations of both vanadium and tungsten are varied simultaneously. Note that the domain where NF616 is present is optimum with 133 MPa.

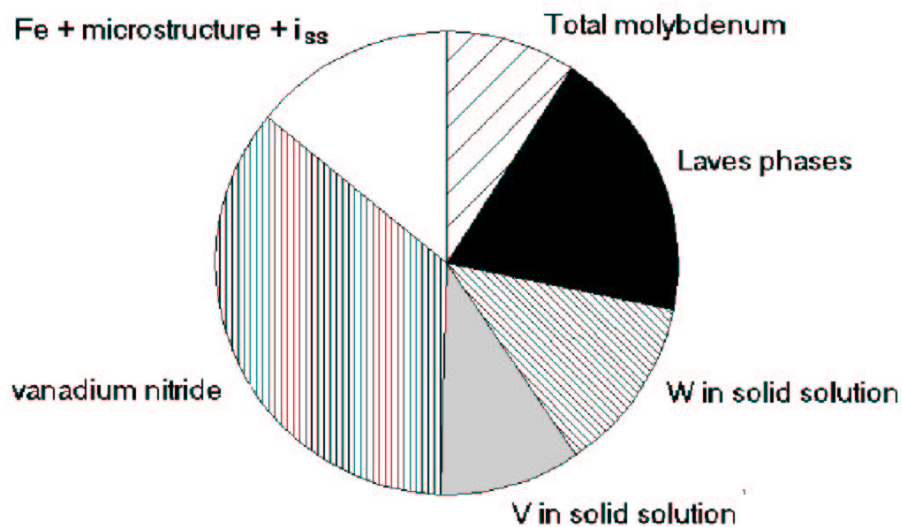


Figure 8.12: Pie charts showing the factorisation of the 10^5 h creep-strength of NF616. The term i_{ss} represents the contributions to the creep-rupture strength due to dissolved solutes other than molybdenum, vanadium and tungsten.

in HCM12A at different temperatures are shown in Fig. 8.13. The FCC was therefore included in the calculations.

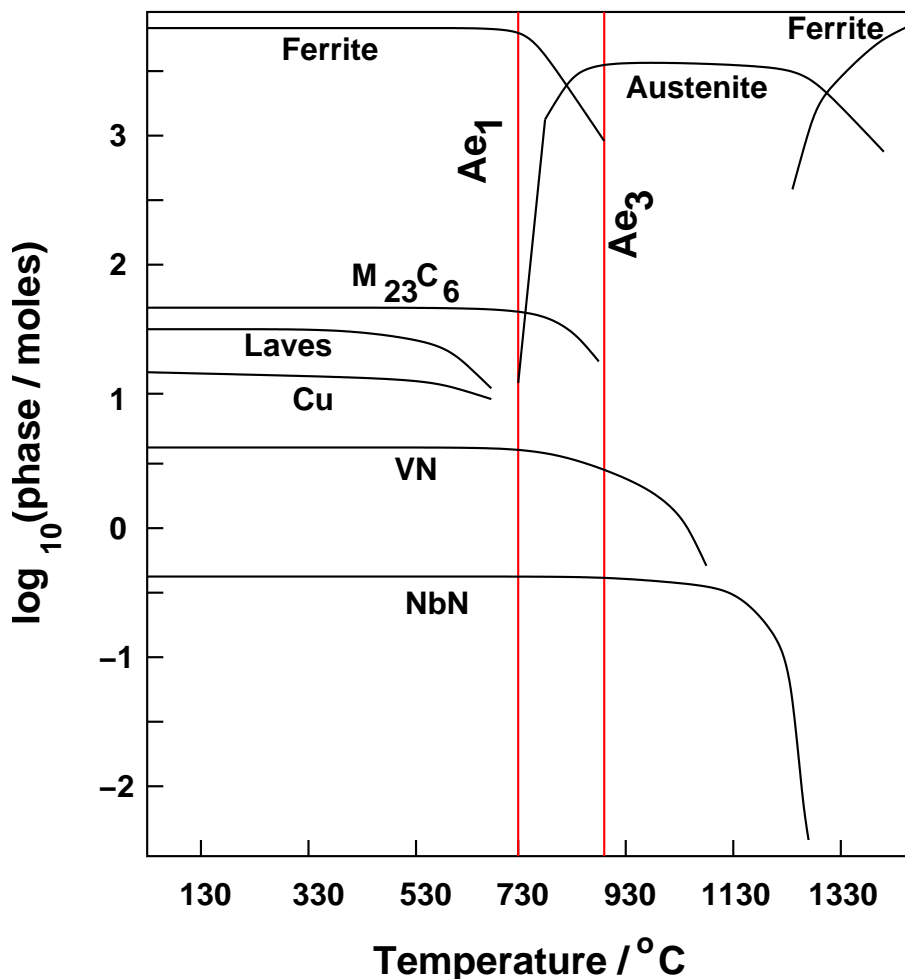


Figure 8.13: Phases existing at various temperatures in HCM12A.

The analysis here is presented for an alloy normalised at 1070 °C for 1 h and tempered at 770 °C for 1 h. In both cases the cooling to room temperature is assumed to be in air. After 10^5 h it is expected to have a creep strength of 120–140 MPa at 600 °C [26]. Calculations using artificial neural network models (described in chapter 4) predicted a 10^5 h rupture strength of 123 ± 10 MPa at 600 °C. The models in combination with thermodynamics were used here for factorisation of creep-rupture strength of HCM12A at 600 °C after 10^5 h.

8.3.1 Components of Creep Strength

Calculations show that vanadium somewhat influences the strengthening contribution of tungsten. At zero concentration of vanadium, the contribution to strength by tungsten reduces (Fig. 8.14).

This influence need not be just due to the presence of vanadium in solid solution or its carbide. Studies have shown that the presence of strong nitride or carbide forming elements like vanadium can interact with interstitial elements like carbon and nitrogen to cause exaggerated solid solution strengthening [134]. The absence of vanadium neither affects Laves phase fractions, wt% of dissolved tungsten or dissolved molybdenum, but only eliminates vanadium nitride and dissolved vanadium (table 8.4) and the exaggerated solid solution strengthening.

	0.2 wt% V	0 wt% V
Mole fraction of precipitates		
M ₂₃ C ₆	3.14×10^{-2}	3.147×10^{-2}
Laves	1.087×10^{-2}	1.023×10^{-2}
NbN	4.80×10^{-4}	4.81×10^{-4}
M ₂ X	0	6.91×10^{-3}
VN	4.46×10^{-3}	0
Dissolved Solutes / wt%		
W _{ss}	0.596	0.653
V _{ss}	0.0064	0

Table 8.4: Phase fractions in absence and presence of vanadium in HCM12A base composition. W_{ss} and V_{ss} denote dissolved tungsten and vanadium concentrations respectively.

However, M₂X rich in chromium and nitrogen appears on removal of vanadium (table 8.4). But, calculations show that mole fraction of M₂X is constant even with variation of tungsten concentration, thus having no effect on tungsten's strength contribution. Hence it would be appropriate to calculate the strength contribution due to tungsten in the absence of vanadium, which clearly removes the synergic strengthening effect due to vanadium that is added implicitly to that of tungsten. Thus, tungsten contributes

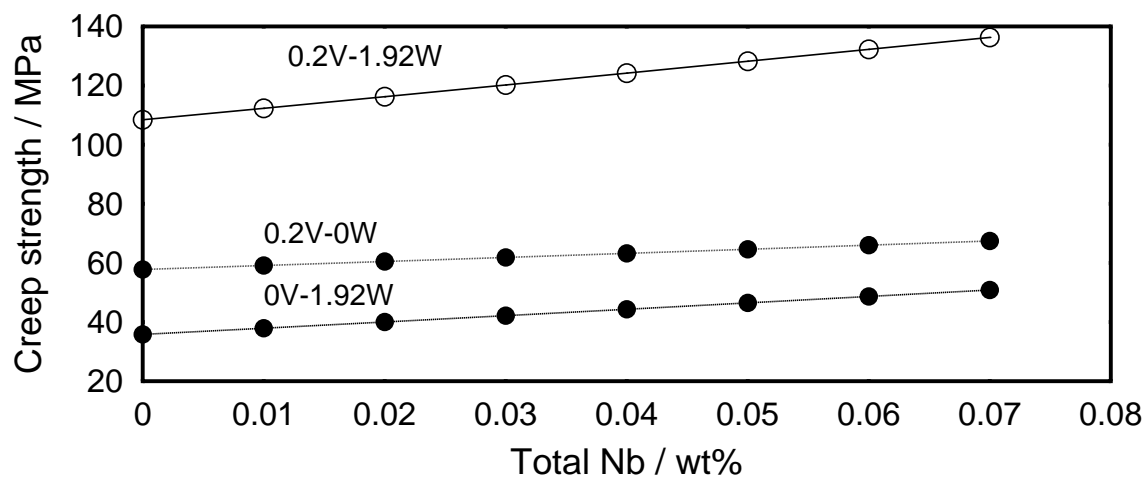
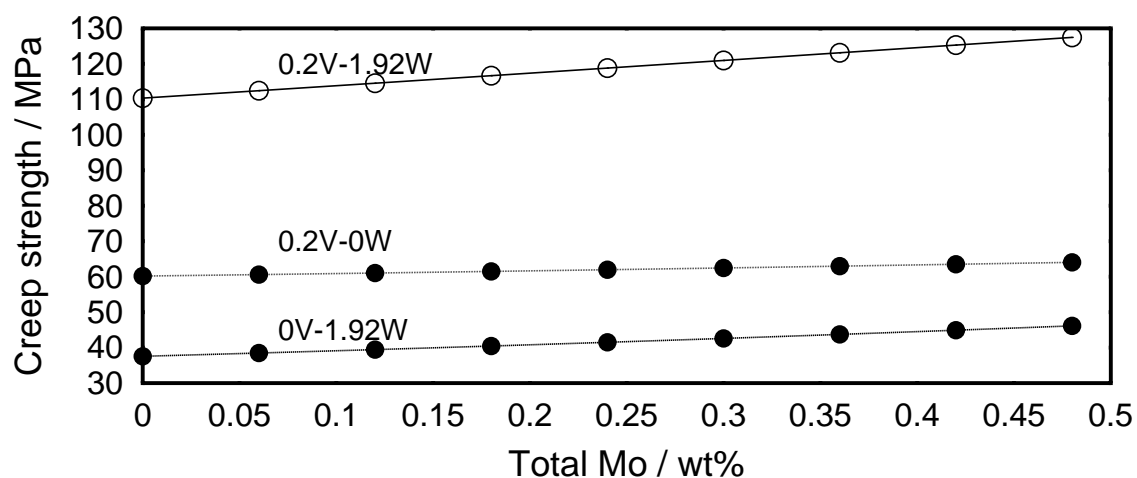
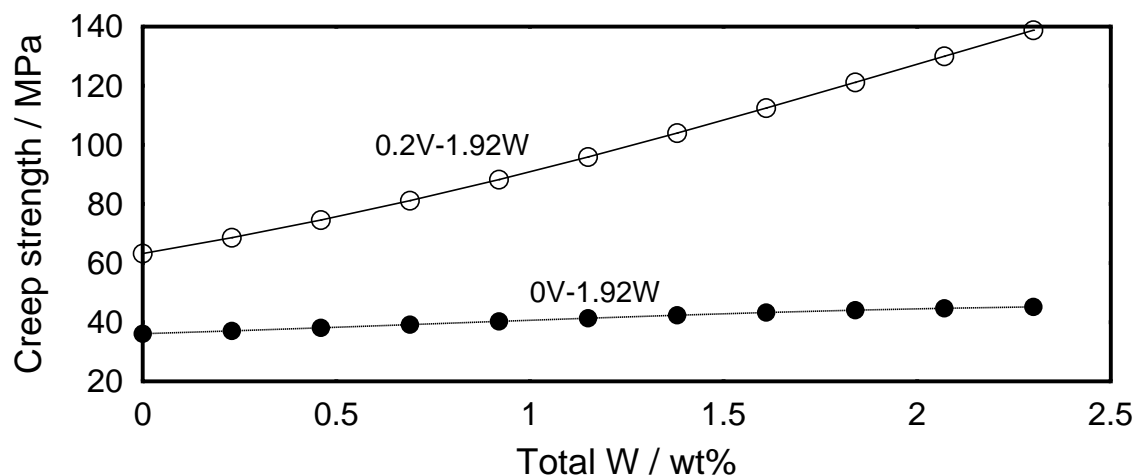


Figure 8.14: Influence of vanadium and tungsten on strength contribution of other alloying elements in HCM12A

8.42 MPa in total at zero concentration of vanadium. Since dissolved tungsten is the only component varying in the shaded region of Fig. 8.15, 3.72 MPa of the 8.42 MPa can be attributed to solution strengthening from tungsten. Hence, the remaining 4.6 MPa comes from Laves phases and dissolved molybdenum.

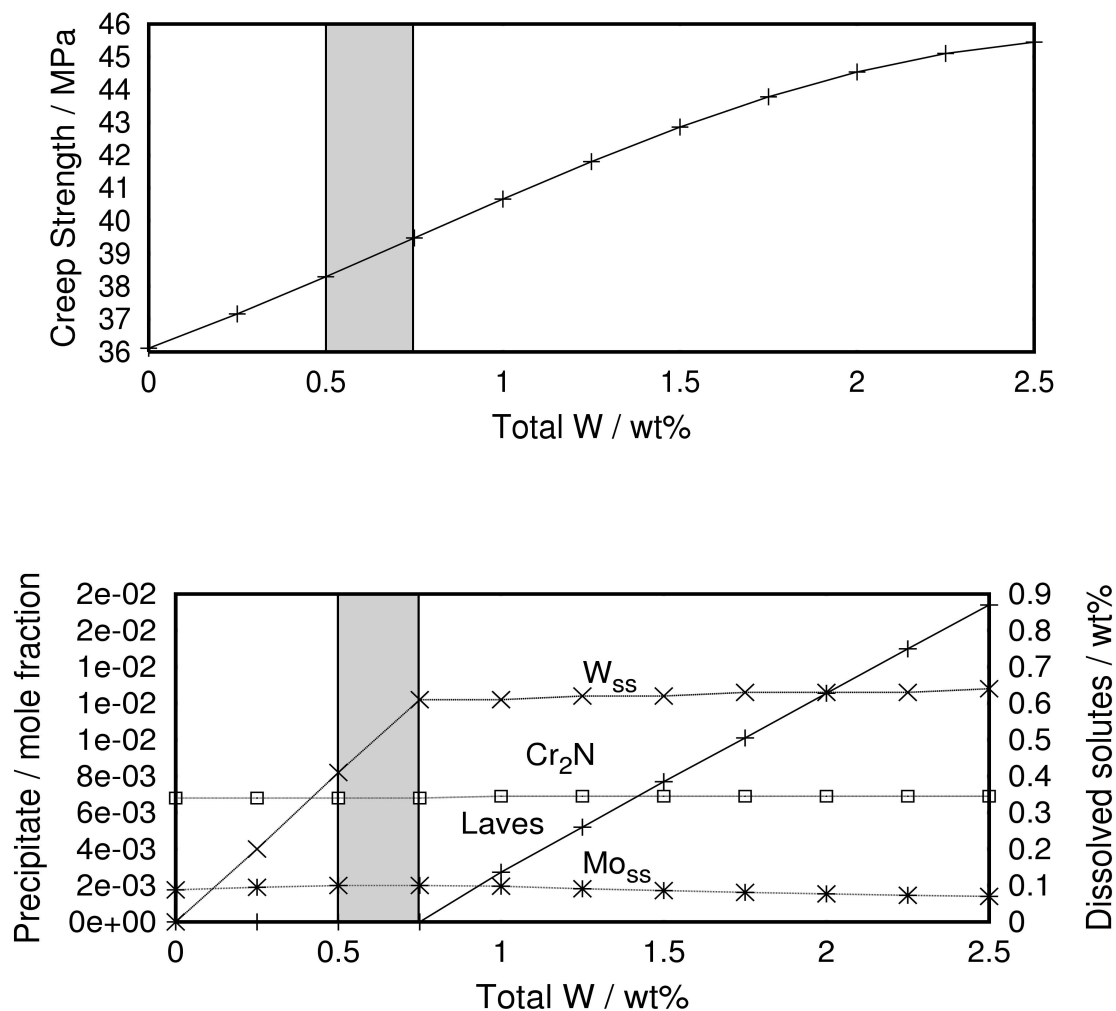


Figure 8.15: Effect of tungsten and its precipitates on creep strength at zero vanadium concentration. W_{ss} and Mo_{ss} are concentrations of dissolved tungsten and molybdenum in ferrite respectively.

Similarly, vanadium and tungsten influence the strength contribution of niobium and molybdenum (Fig. 8.14). Thus, the contribution to strength due to niobium should be:

$$\begin{aligned}\sigma_{Nb} &= \sigma_{Nb|V,W} - \sigma_{Nb|V=0,W} - \sigma_{Nb|V,W=0} \\ &= 14.68 - 6.17 - 6 = 2.51 \text{ MPa}\end{aligned}\quad (8.1)$$

where $\sigma_{Nb|V,W}$, $\sigma_{Nb|V=0,W}$ and $\sigma_{Nb|V,W=0}$ are the strength contributions due to niobium at 0.2V-1.92W wt%, 0V-1.92W wt% and 0.2V-0W wt% respectively. Calculations for molybdenum after removing the effect of vanadium and tungsten give 2.29 MPa.

The presence of dissolved vanadium and its nitride contributes 78.8 MPa to the total strength. It should be noted that the total strength of HCM12A is a synergic effect of both tungsten and vanadium, whereas the individual contributions of W, Nb and Mo are always small. The individual contributions of dissolved vanadium or vanadium nitride could not be separated because other factors did not remain constant (Fig. 8.16).

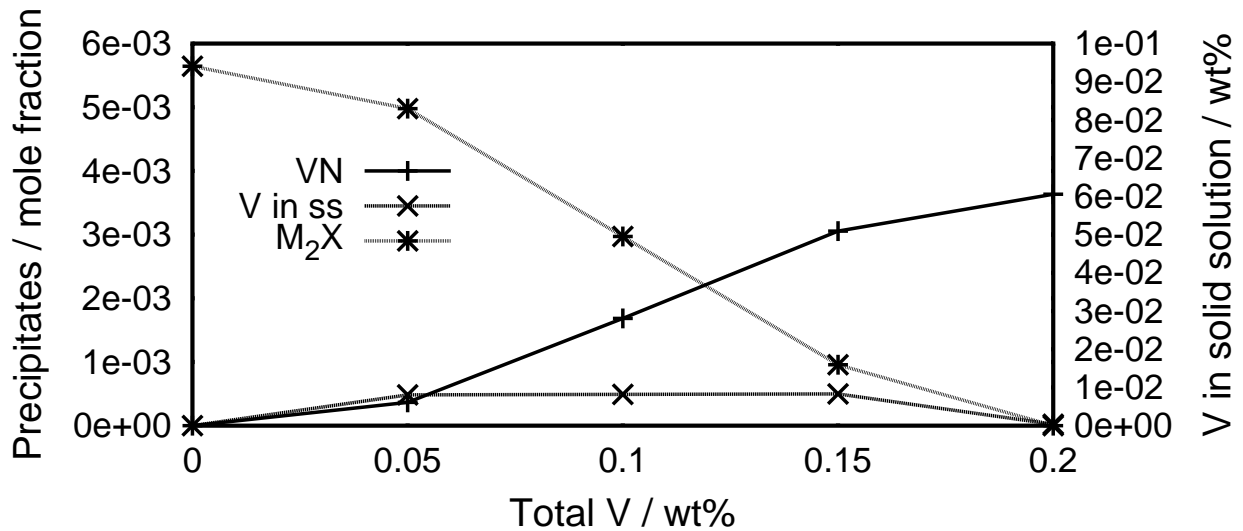


Figure 8.16: Phase fractions of VN and M₂X and wt% of dissolved vanadium.

It has long been known that chromium hardly contributes to any strengthening at 600 °C (Fig. 8.2). Chromium is added to the steel mainly for corrosion resistance and hardenability [135].

Having calculated the contributions due to all the alloying elements, the remaining contribution to strength of HCM12A comes from Fe and microstructure ($123-92.02=30.98$ MPa). Table 8.5 gives the summary of strength contribution from each component.

	Strength contribution	
	MPa	Percentage
Total vanadium	78.8	64
Fe and microstructure	30.9	25
Dissolved tungsten	3.7	3
Laves phase and dissolved molybdenum	4.6	4
Total niobium	2.5	2
Total molybdenum	2	2

Table 8.5: Strength contribution from the components

The pie chart in Fig. 8.17 summarises the strength contributions from individual components in the alloy.

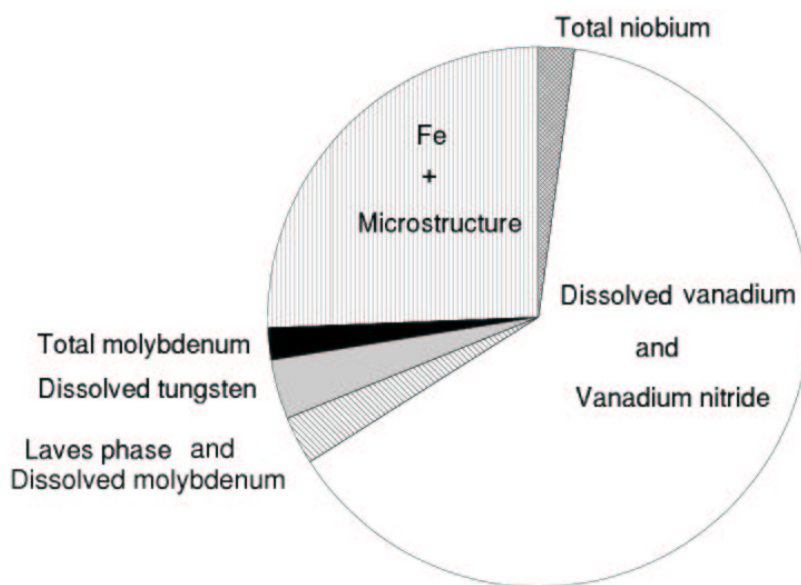


Figure 8.17: Pie-chart showing strength contribution from various components of HCM12A. The total strength of HCM12A is 123 MPa at 600 °C after 10^5 h.

8.4 Summary

A combination of neural network models to predict the mechanical properties and phase stability calculations to identify the phases, were used in factorising the creep strength of the heat-resisting steels, $2\frac{1}{4}\text{Cr1Mo}$, NF616 and HCM12A. The factorisation was non-linear.

In the case of $2\frac{1}{4}\text{Cr1Mo}$ steels, the proportion of contribution to 10^5 h creep-rupture strength from dissolved solutes increased at 600°C in comparison with 550°C .

For the high chromium heat-resisting steels, NF616 and HCM12A, vanadium is a strong contributor to the creep-strength at 600°C . In this tungsten alloyed steels Laves phase contributes more to the creep-strength than dissolved tungsten as expected [90].

Copper is added to HCM12A for improving the toughness. The contribution from the inherent strength of iron along with the microstructure is comparatively less than from other components.

All the other precipitates must play a significant role during the early stages of creep life but it cannot be addressed here, since the calculations rely on equilibrium.

Chapter 9

SUMMARY AND FUTURE WORK

The subject of welding is challenging because of its complexity and because its applications are in the majority of cases, safety critical. An important parameter which features in structural integrity at ambient temperatures is toughness, which can be paraphrased as the ability of the material to avoid brittle fracture. In the context of long term service at elevated temperatures of the kind typical in power plant, it is creep which frequently controls the life of components.

The research presented in this thesis deals with both these aspects from the point of view of welding alloys. Research has been in progress over many years to try and improve the toughness and strength of best available commercial alloy, but without much success.

At the beginning of this project, two welds A and B with large concentrations of nickel were manufactured in the hope that the nickel enhances toughness. The high nickel concentration should also lead to a microstructure which is predominantly martensitic, but the martensite was expected to be safe given that the alloy design allowed for a low carbon concentration. It was anticipated that any retained austenite would assist in blunting cracks. Unfortunately, these qualitative ideas based on experience failed, leading to strong but brittle weld metals.

As a consequence, a number of neural network models based on a Bayesian framework were implemented; a careful study of these models revealed that nickel is only beneficial in large concentrations when the manganese concentration is kept low. This

demonstrated the power of the method to assimilate the simultaneous effect of large numbers of variables, a feat which is hard to achieve when making qualitative judgements about complex phenomena.

At manganese concentrations, nickel was found theoretically to have a pronounced detrimental effect on toughness. These trends are new revelations and caused considerable excitement. To validate them experimentally, a weld "C" was designed and manufactured and proved to have much better toughness than previous attempts with high nickel concentrations.

Since toughness should strictly be compared at similar strength, comparisons were made which demonstrated that an enhancement of toughness was indeed obtained following the prediction of the models. Retained austenite fractions were measured and shown not to be capable of explaining the large enhancement of toughness in weld C.

The best explanation seems to be associated with transformation temperatures, which were measured using dilatometry. It seems that the high Ac_1 temperature of weld C leads to the elimination of regions with excessive hardness in multirun weld deposits; by contrast, a combination of high manganese and nickel gives particularly high hardness "hot-spots" which must be detrimental to toughness. High-resolution hardness maps confirms this hypothesis.

One effect of a high Ac_1 temperature is that it causes larger tempered regions in the underlying regions when a weld bead is deposited as a part of a multirun weld. Furthermore, tensile tests performed on fully martensitic samples of high and low-Mn welds gave identical stress-strain curves showing that there is no fundamental effect of manganese which alters the strain-hardening behaviour.

It would be interesting to make a similar weld which also contains cobalt to raise the Ac_1 temperature of a high-Mn weld, to see if the toughness can be improved.

Neural network models have been successful in the past in the design of creep-resistant steels and weld deposits. However, it has always been difficult, whether using

neural networks or other methods, to identify what contributes to creep rupture strength and by how much. In this project, a different approach was adopted to attempt a non-linear factorisation of the long-term creep-rupture strength. This was done by including the equilibrium precipitate fractions and the chemical composition of the residual ferrite in the analysis.

It was demonstrated using case studies based on classic steels (2.25Cr-1Mo, NF616 and HCM12A) that it is frequently possible to identify the roles of particular phases or components in solution, and that the results are physically reasonable.

It would be useful in future work to incorporate in the neural network, a kinetic theory so that the evolution of precipitates with time is included enabling the short-term creep strength also to be factorised. The process can then be used effectively in alloy design.

The tendency for coarsening of precipitates can also be studied in principle in the context of creep-rupture strength but there is a need for multicomponent and multiphase coarsening theory before such an exercise can be implemented in practice.

APPENDIX I

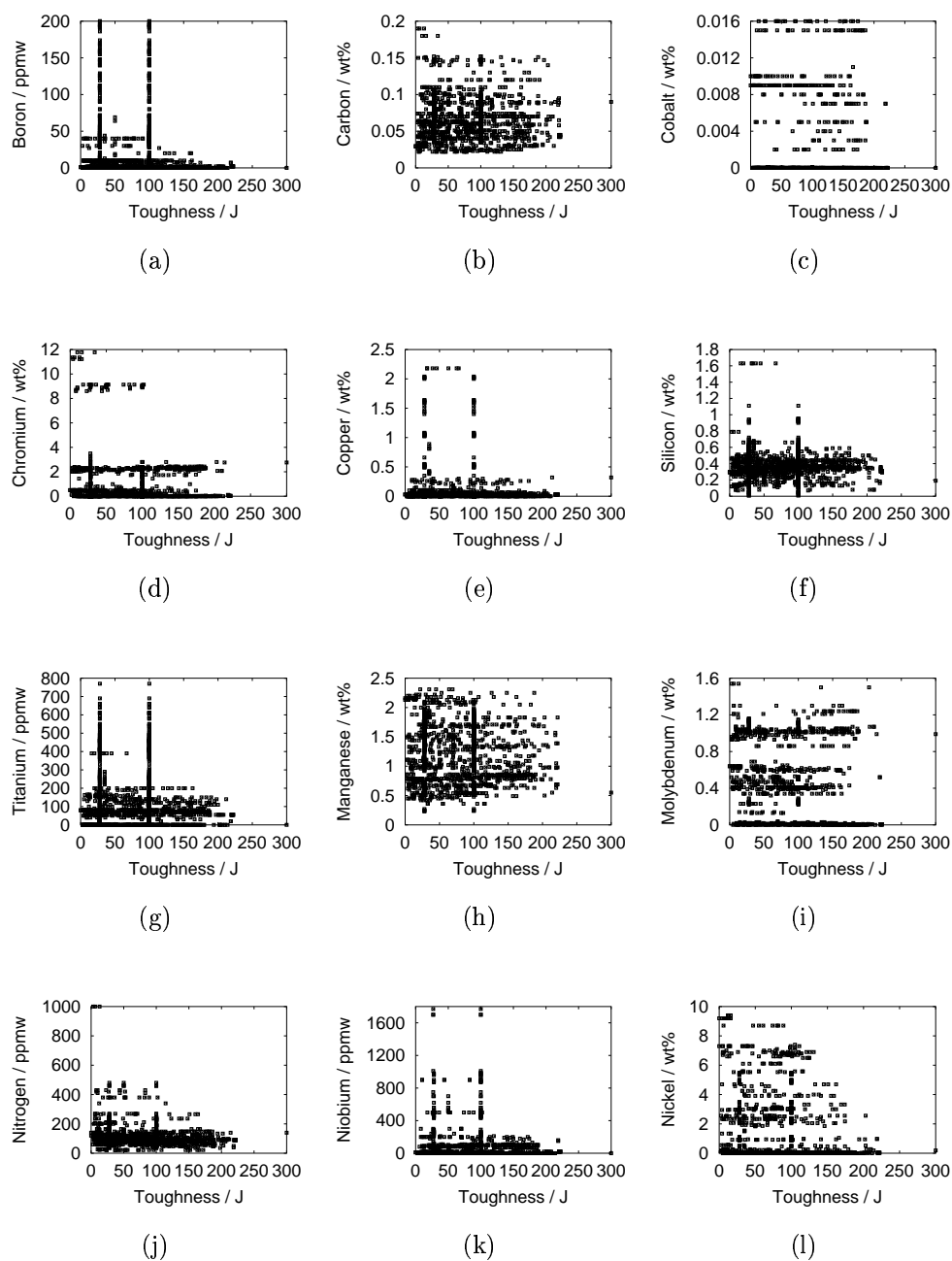


Figure 9.1: The one-dimensional distribution of data

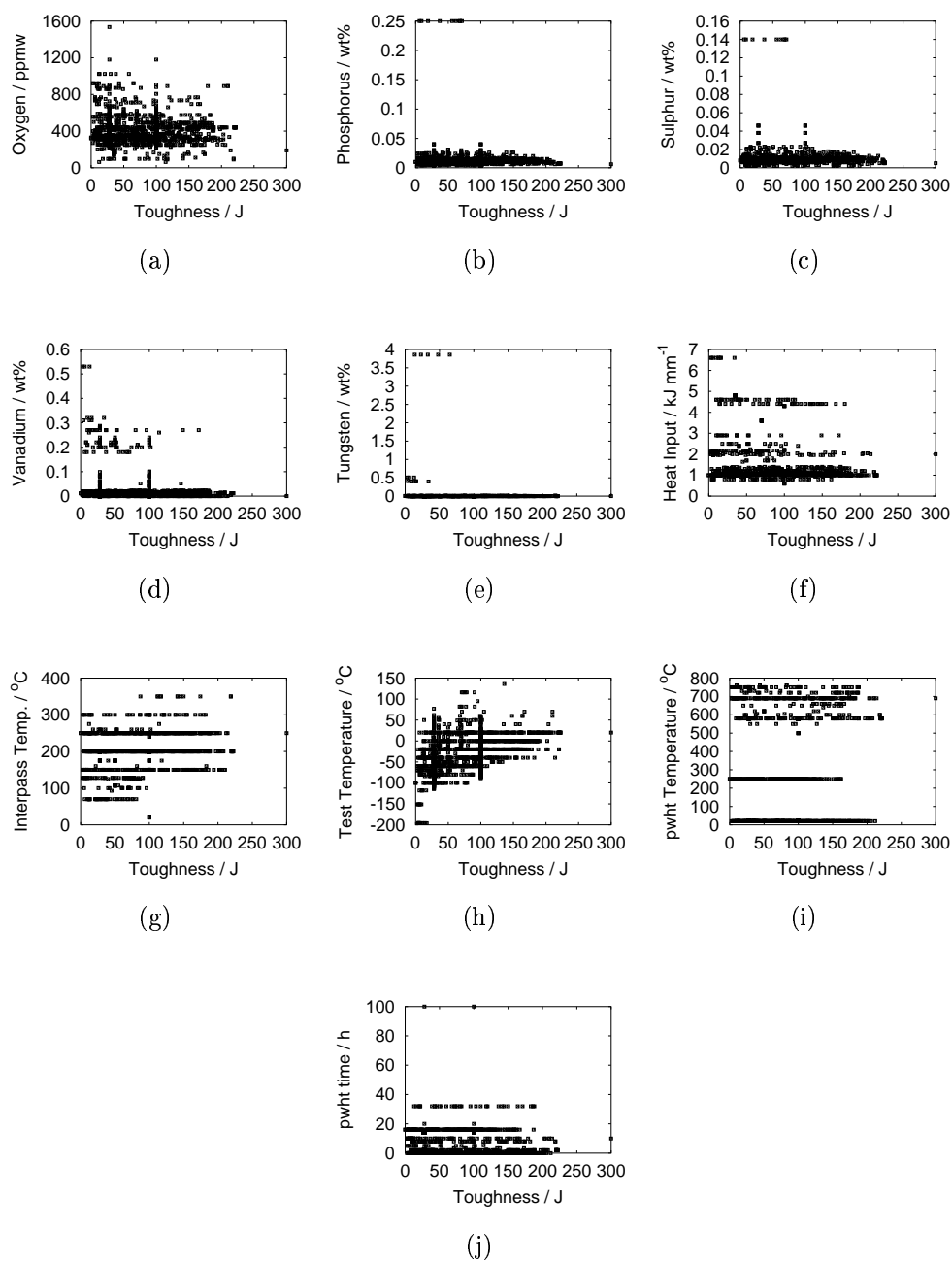


Figure 9.2: The one-dimensional distribution of data

Input variables		Minimum	Maximum	Mean	Std. Deviation
All elements in wt% unless otherwise specified					
1	Carbon	0.02	0.19	0.07	0.021
2	Silicon	0.01	1.63	0.4	0.13
3	Manganese	0.23	2.31	1.2	0.42
4	Sulphur	0.002	0.14	0.0078	0.008
5	Phosphorus	0.003	0.25	0.01	0.014
6	Nickel	0	9.4	0.6	1.6
7	Chromium	0	11.78	0.5	1.4
8	Molybdenum	0	1.54	0.2	0.34
9	Vanadium	0	0.53	0.01	0.045
10	Copper	0	2.18	0.06	0.22
11	Cobalt	0	0.016	0.0007	0.0027
12	Tungsten	0	3.8	0.008	0.2
13	Oxygen / ppm	63	1535	406.2	112.3
14	Titanium / ppm	0	770	100.03	135.4
15	Nitrogen / ppm	21	1000	98.3	67.8
16	Boron / ppm	0	200	13.8	34.3
17	Niobium / ppm	0	1770	39.3	136.8
18	HI ^a / kJ mm ⁻¹	0.6	6.6	1.19	0.7
19	IT ^b / °C	20	350	200.19	31.23
20	pwhtT ^c / °C	20	760	185.36	257.24
21	pwhtt ^d / h	0	100	2.7	6.13
22	Test temperature / °C	-196	136	-44.25	36.13

Table 9.1: Input variables used to train the models for establishing a network of composition, heat treatment and welding parameters with toughness, yield strength, ultimate tensile strength and toughness.

^aHeat input

^bInterpass temperature

^cpost-weld heat treatment temperature

^dpost-weld heat treatment time

APPENDIX II

Spread of Inputs for the Creep–Rupture Strength Hybrid Model

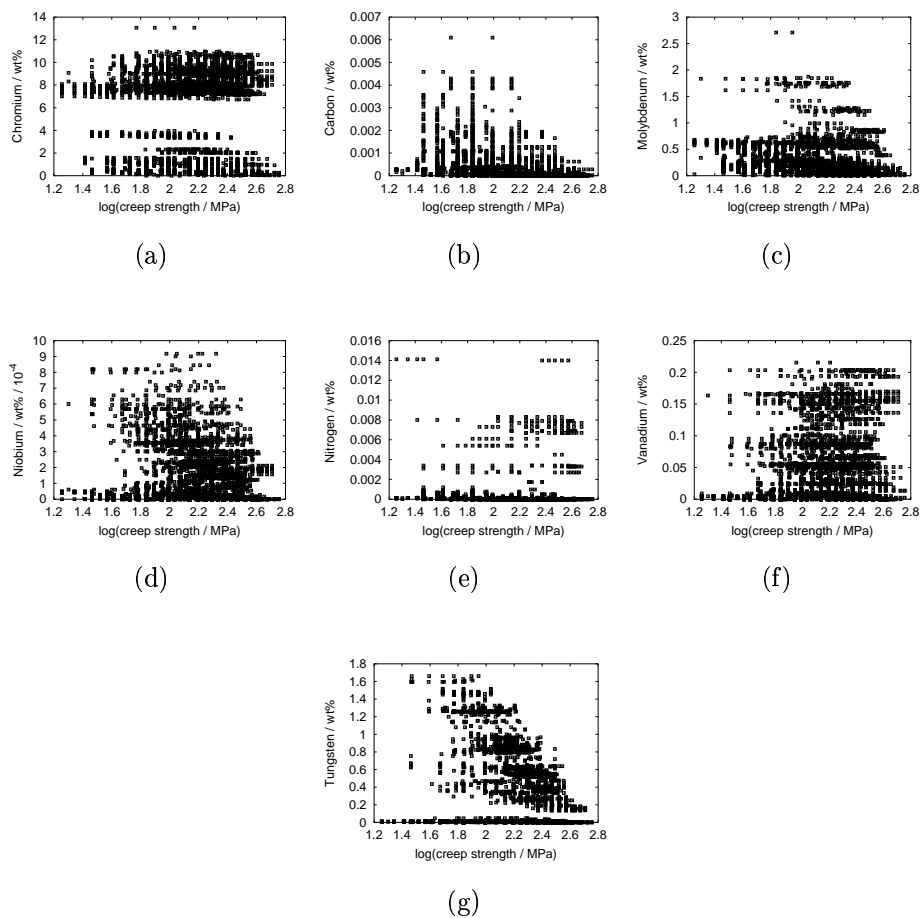


Figure 9.3: Spread of wt% of solid solution strengthening solutes.

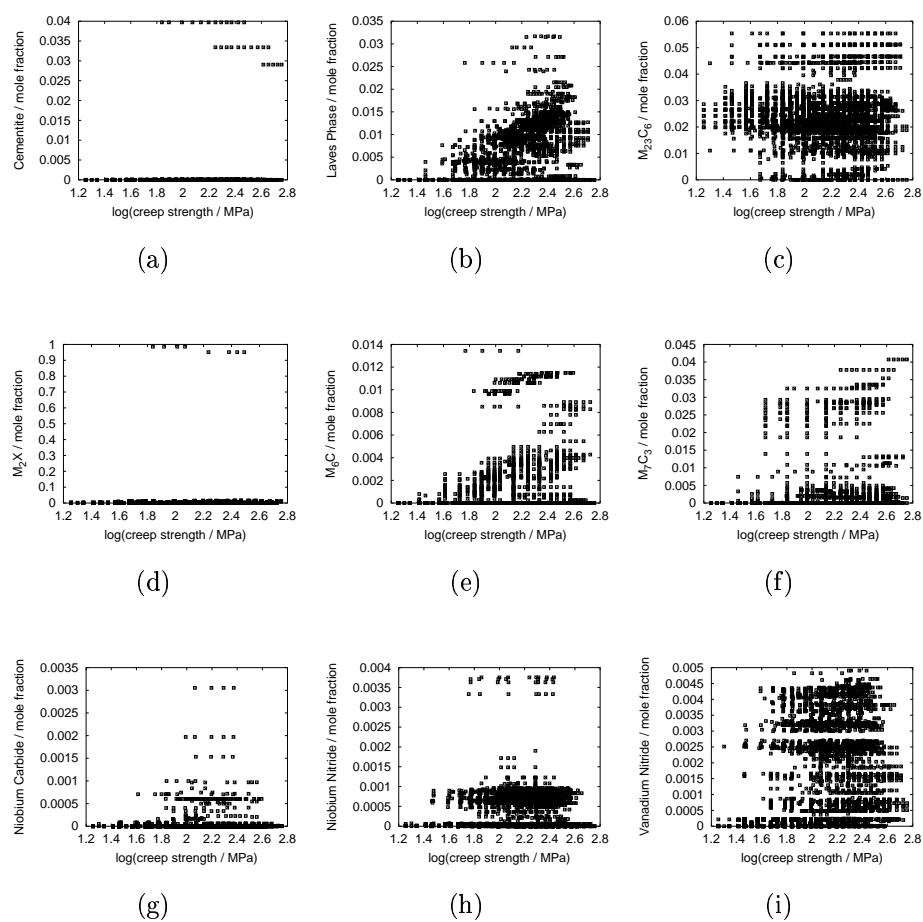


Figure 9.4: Spread of precipitate mole fraction.

Input component	Minimum	Maximum	Mean	Standard Deviation
log (creep rupture time /h)	-1.77	5.28	3.06	1.11
Temperature (K)	723	1023	861.4	65.1
wt% of elements				
Carbon	0.004	0.48	0.1219	0.056
Silicon	0.01	0.86	0.2678	0.1848
Manganese	0.01	0.92	0.5196	0.1087
Phosphorus	0.001	0.029	0.0126	0.0062
Sulphur	0.0005	0.02	0.0076	0.0049
Chromium	0.59	14.72	6.5537	4.1291
Molybdenum	0.04	2.99	0.7236	0.4204
Tungsten	0.01	3.93	0.6427	0.8566
Nickel	0.01	2	0.1822	0.2296
Copper	0.003	1.56	0.1104	0.2231
Vanadium	0.01	0.3	0.1275	0.1035
Niobium	0.001	0.312	0.0294	0.0372
Aluminium	0.001	0.1651	0.0280	0.0235
Nitrogen	0.001	0.057	0.0098	0.0097
Boron	0	0.051	0.0009	0.0029
Cobalt	0	3.09	0.0554	0.3257
Tantalum	0	0.1	0.0002	0.0045
Oxygen	0.003	0.035	0.0099	0.002
Rhenium	0	1.69	0.0057	0.0807

Table 9.2: Service time and temperature along with chemical composition.

Input component	Minimum	Maximum	Mean	Std. Deviation
Normalising Temperature (K)	1123	1473	1268.5	71.8
Normalising Time (h)	0.17	33	2.43	4.55
CR of Normalise in furnace (0 or 1)	0	1	0.042	0.20
CR of Normalise in air (0 or 1)	0	1	0.74	0.44
CR of Normalise for oil quench (0 or 1)	0	1	0.15	0.36
CR of Normalise for water quench (0 or 1)	0	1	0.06	0.24
Tempering Temperature (K)	823	1323	998.87	73.32
Tempering time (h)	0.5	83.5	4.81	11.24
CR of Temper in furnace (0 or 1)	0	1	0.056	0.229
CR of Temper in air (0 or 1)	0	1	0.89	0.3
CR of Temper for oil quench (0 or 1)	0	1	0.031	0.174
CR of Temper for water quench (0 or 1)	0	1	0.013	0.115
Annealing temperature (K)	300	1023	461.54	282.62
Annealing Time (h)	0.5	90	4.38	11.01
CR of anneal in furnace (0 or 1)	0	1	0.127	0.333
CR of anneal in air (0 or 1)	0	1	0.873	0.333

Table 9.3: Heat treatment parameters. CR represents Cooling Rate.

Input component	Minimum	Maximum	Mean	Standard Deviation
All units in mole fraction				
M ₂ X	0	0.9857	0.0034	0.0436
Cementite	0	0.0397	0.0002	0.0026
M ₇ C ₃	0	0.0407	0.0013	0.0055
M ₂₃ C ₆	0	0.0554	0.0235	0.0099
M ₆ C	0	0.0134	0.0006	0.002
Laves phases	0	0.0317	0.0037	0.0056
Niobium carbide	0	0.0031	0	0.0002
Niobium nitride	0	0.0038	0.0003	0.0004
Vanadium nitride	0	0.0049	0.0015	0.0015
wt% of solid solution strengthening elements				
Chromium	0.0009	13.0613	5.2916	3.7615
Molybdenum	0.003	2.7086	0.274	0.3038
Tungsten	0	1.6607	0.2647	0.3963
Vanadium	0	0.2154	0.0422	0.0549
Niobium	0	0.0009	0.0001	0.0002
Nitrogen	0	0.0141	0.0003	0.0013
Carbon	0	0.0061	0.0003	0.0006
Output variable				
Creep strength / MPa	18.0	568.9		
log(Creep strength / MPa)	1.255	2.755	2.1447	0.2825

Table 9.4: Equilibrium precipitate fractions and wt% solid solution strengthening elements used as inputs. The output is stated in the last two rows, both as creep-rupture strength and its logarithm; only the latter is used in the developement of the model, the former is simply there for illustration.

APPENDIX III

Hot Strength vs Creep Strength of $2\frac{1}{4}\text{Cr}-1\text{Mo}$ Weld Metals

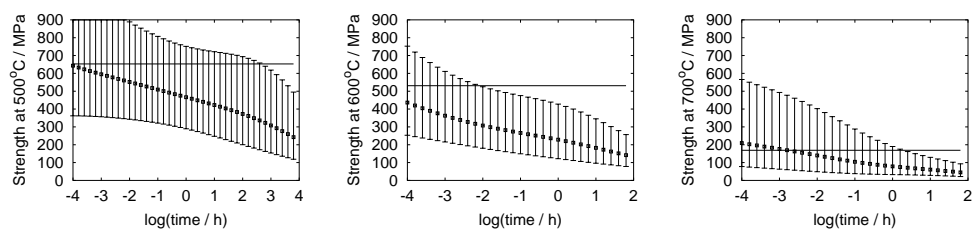
A tensile test is carried out over a perceptibly short period of time, at strain rates where the measured properties are not strain-rate sensitive. A creep test, on the other hand, is all about time-dependent strain.

It is nevertheless possible that the creep models reported in this thesis could be used to estimate the hot-tensile strength. After all, a creep test conducted at a sufficiently high stress may have a short enough duration to give results which are comparable to those from a hot-tensile test. The work presented in this appendix was conducted to examine this very possibility.

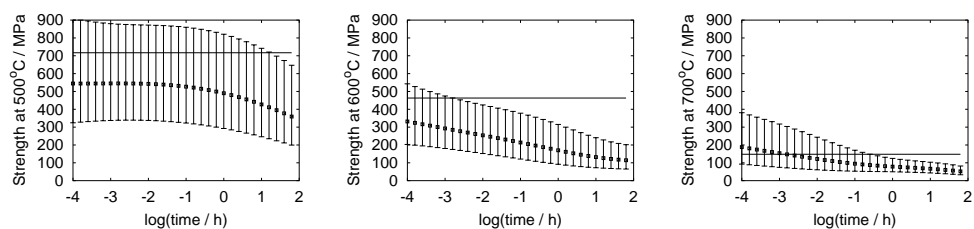
The creep model described in chapter 7 was used to predict the hot-strength of $2\frac{1}{4}\text{Cr}-1\text{Mo}$ submerged-arc weld metals whose compositions are given in table 9.5. The welding parameters used are as shown in table 9.6.

The results presented in Fig. 9.5 show that for 500 °C and 600 °C, the creep rupture stress always falls below the measured hot strength, even when the test period is 10^{-4} h, a time period not far from that required to conduct a tensile test. This might be expected since the strain rates involved in creep-rupture tests are typically 10^{-8} – 10^{-5} s^{-1} [4], compared with 3×10^{-3} s^{-1} for a tensile test. The yield strength is expected to decrease at low strain rates [4]. However, the general trend is inconsistent with the results for 700 °C where the hot-strength is constantly below the rupture strength.

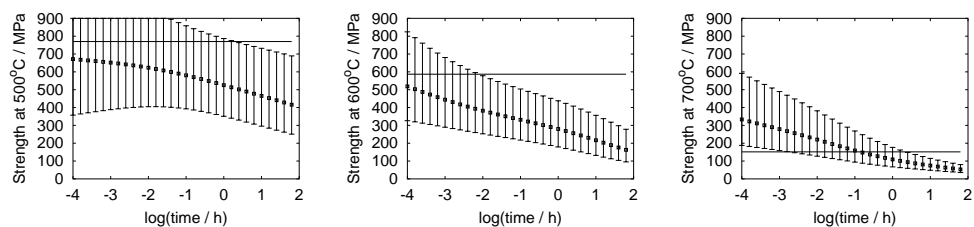
Perhaps a better procedure would be to include hot-strength in the creep rupture model in future work.



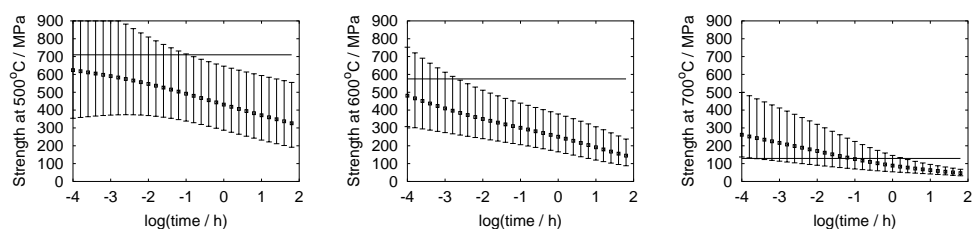
(a) Composition A



(b) Composition B



(c) Composition C



(d) Composition D

Figure 9.5: Comparison of hot strength (horizontal line) and creep strength

All values in wt. %

	A	B	C	D
C	0.07	0.06	0.12	0.1
Si	0.35	0.58	0.3	0.3
Mn	0.96	0.64	0.92	0.87
S	0.016	0.022	0.007	0.008
P	0.014	0.015	0.012	0.016
Ni	0.04	0.33	0.16	0.17
Cr	2.26	2.33	2.8	2.75
Mo	0.94	1.03	1.05	1.05
V	0.035	0.02	0.03	0.03
Al	0.004	0.008	0.019	0.021
B	0.0002	0.0006	0.0007	0.0003
Sn	0.006	0.011	0.015	0.015
W	0.05	0.06	0.09	0.09
Cu	0.04	0.24	0.29	0.24

Table 9.5: Composition

	Current / Amp	Voltage / V	Interpass Temperature / °C
A	350	28	300–350
B	450	30	300–350
C	550	28	300–350
D	450	30	300–350

Table 9.6: Welding parameters

	500 °C	600 °C	700 °C
A	653	531	169
B	717	463	148
C	770	587	152
D	710	575	129

Table 9.7: Measured 0.2% proof strength in MPa at a strain rate of $3.3 \times 10^{-3} \text{ s}^{-1}$.

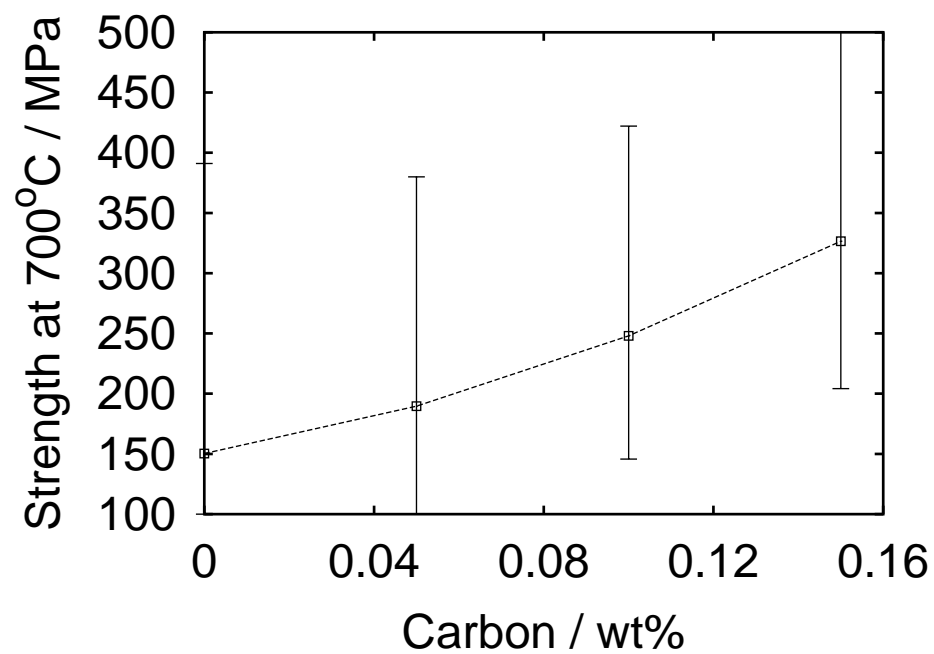


Figure 9.6: Influence of carbon concentration on the creep-strength of welds C and D.

APPENDIX IV

The role of the A_{e1} temperature in determining the creep-rupture strength

It has been suggested that the creep-rupture strength should correlate with the A_{e1} temperature of the steel concerned. A higher A_{e1} temperature is proposed to lead to a stronger steel during creep deformation [26].

The suggestion is that for a given absolute tempering temperature, a higher A_{e1} implies a lower homologous tempering temperature, where the latter is the tempering temperature divided by the A_{e1} temperature. But this is not soundly based since the A_{e1} temperature does not determine the tempering response. It has therefore been suggested [127] that the observed correlation is not sensible, but comes about from a neglect in the analysis of many other variables which control creep.

To test the hypothesis on a much larger database, the steels described in tables 9.8-9.9 were studied theoretically. Their equilibrium transformation temperatures were calculated using MTDATA; the steels were chosen because they all had similar creep rupture strength.

A plot (Fig. 9.7) of A_{e1} vs Creep strength shows that even with increasing A_{e1} temperature the effect on creep strength is zero, thus proving that equilibrium transformation temperatures do not affect creep properties.

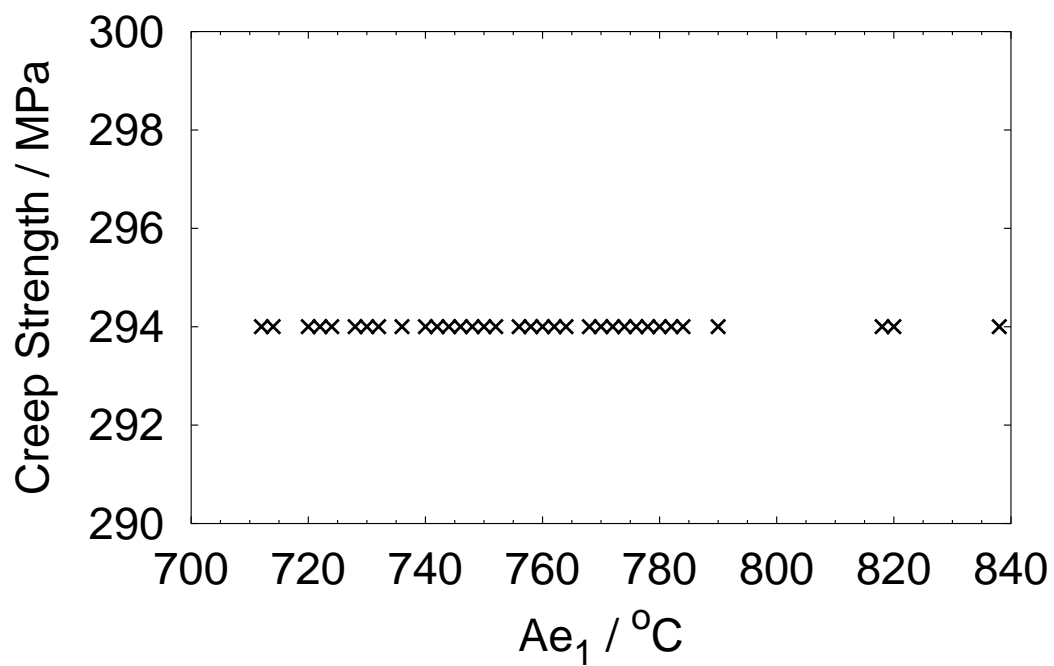


Figure 9.7: Figure showing that there is no explicit correlation between calculated A_{e1} temperature and experimental creep strength of steels.

	1	2	3	4	5	6	7	8	9	10
log (Rupture time / h)	4.31	4.11	3.93	3.74	3.35	3.65	3.3	3.44	3.23	2.65
Temperature / K	773	773	773	773	773	773	773	773	773	773
All elements in wt%										
C	0.29	0.28	0.18	0.12	0.14	0.15	0.48	0.14	0.17	0.14
Si	0.2	0.2	0.2	0.25	0.25	0.61	0.3	0.25	0.6	0.65
Mn	0.75	0.72	0.5	0.48	0.57	0.6	0.72	0.56	0.56	0.53
Cr	1	1.02	1	0.64	0.96	1.2	1.15	1.02	1.27	1.22
Mo	1.25	1.12	0.45	0.51	0.53	0.51	0.59	0.5	0.52	0.52
W	0.01	0.01	0.01	0.01	0.01	0.01	0.01	0.01	0.01	0.01
Ni	0.34	0.32	0.02	0.04	0.15	0.35	0.12	0.04	0.17	0.23
Cu	0.14	0.2	0.01	0.04	0.14	0.14	0.06	0.06	0.15	0.16
V	0.26	0.27	0.01	0.01	0.01	0.01	0.28	0.01	0.01	0.01
N	0.01	0.01	0.01	0.01	0.01	0.01	0.01	0.01	0.01	0.01
Al	0	0	0.01	0.01	0.01	0.02	0.01	0	0.03	0.02
Co	0	0	0	0	0	0	0	0	0	0
Ae ₁ / K	985	987	993	995	997	1001	1003	1005	1009	1013
Ae ₃ / K	1087	1087	1113	1137	1119	1131	1051	1125	1135	1147
Creep strength / MPa	294	294	294	294	294	294	294	294	294	294
	11	12	13	14	15	16	17	18	19	20
log (Rupture time / h)	3.48	4.17	1.67	2.14	3.91	3.26	2.42	2.42	2.89	4.54
Temperature / K	773	773	823	823	773	723	773	773	773	723
All elements in wt%										
C	0.14	0.18	0.11	0.11	0.13	0.16	0.12	0.15	0.14	0.14
Si	0.34	0.37	0.01	0.02	0.66	0.31	0.72	0.27	0.21	0.25
Mn	0.73	0.66	0.56	0.56	0.58	0.7	0.5	0.61	0.53	0.55
Cr	1.06	1.07	11	11.02	1.24	2.27	1.2	2.35	2.4	2.44
Mo	0.96	1.03	0.42	0.41	0.5	0.99	0.46	0.96	1.01	1.03
W	0.01	0.01	1.94	1.95	0.01	0.01	0.01	0.01	0.01	0.01
Ni	0.13	0.1	0.33	0.33	0.03	0.2	0.1	0.32	0.14	0.18
Cu	0.08	0.12	0.81	0.85	0.03	0.04	0.04	0.02	0.16	0.13
V	0.23	0.3	0.18	0.19	0.01	0.01	0.01	0.01	0.01	0.01
Nb	0	0	0.02	0.05	0	0.01	0	0	0.01	0.01
N	0.01	0.01	0.05	0.05	0.01	0.01	0	0.01	0.01	0.01
Al	0	0.02	0	0.01	0	0	0.02	0.01	0.02	0.02
Co	0	0	0	0	0	0.05	0	0	0.05	0.05
Ae ₁ / K	1015	1017	1019	1021	1023	1025	1029	1031	1033	1035
Ae ₃ / K	1147	1147	1155	1175	1163	1121	1173	1121	1127	1129
Creep strength / MPa	294	294	294	294	294	294	294	294	294	294

Table 9.8: Composition of heat-resistant steels which have same creep strength though with varying Ae₁ temperatures.

	21	22	23	24	25	26	27	28	29	30
log (Rupture time /h)	3.14	3.61	1.18	3.63	4.11	2.31	2.88	2.63	2.1	1.88
Temperature / K	773	773	773	773	723	773	773	773	773	773
All elements in wt%										
C	0.11	0.1	0.12	0.13	0.12	0.12	0.12	0.12	0.1	0.1
Si	0.75	0.71	0.26	0.25	0.29	0.39	0.29	0.35	0.35	0.23
Mn	0.46	0.47	0.48	0.49	0.48	0.52	0.5	0.49	0.5	0.43
Cr	1.27	1.28	2	2.31	2.2	2.24	2.25	2.24	2.25	2.46
Mo	0.55	0.56	0.96	1.01	0.99	0.97	0.96	1.04	1.04	0.94
W	0.01	0.01	0.01	0.01	0.01	0.01	0.01	0.01	0.01	0.01
Ni	0.06	0.02	0.08	0.03	0.05	0.03	0.03	0.1	0.1	0.04
Cu	0.07	0.04	0.08	0.03	0.07	0.04	0.05	0.04	0.04	0.07
V	0.01	0.01	0.01	0.01	0.01	0.01	0.01	0.01	0.01	0.01
Nb	0	0	0	0.01	0	0.01	0.01	0.01	0.01	0.01
N	0.01	0.01	0.01	0.01	0.01	0.01	0.01	0.01	0.01	0.01
Al	0.01	0.01	0.01	0.04	0.02	0.01	0	0	0	0.01
Co	0	0	0	0.05	0	0.05	0.05	0.05	0.05	0.05
Ae ₁ / K	1037	1041	1043	1045	1047	1049	1051	1053	1055	1057
Ae ₃ / K	1187	1193	1145	1147	1153	1163	1151	1157	1167	1153
Creep strength / MPa	294	294	294	294	294	294	294	294	294	294
	31	32	33	34						
log (Rupture time /h)	2.74	2.31	2.33	0.43						
Temperature / K	773	823	873	923						
All elements in wt%										
C	0.08	0.08	0.13	0.2						
Si	0.42	0.02	0.05	0.06						
Mn	0.54	0.49	0.43	0.33						
Cr	2.28	9.37	8.95	10.5						
Mo	0.96	0.51	1.18	1.5						
W	0.01	1.82	0.65	0.01						
Ni	0.03	0.2	0.06	0.04						
Cu	0.03	0.01	0.05	0.05						
V	0.01	0.2	0.17	0.21						
Nb	0.01	0.05	0.06	0.06						
N	0.01	0.04	0.05	0.03						
Al	0	0	0	0						
Co	0.05	0	0.99	0.02						
Ae ₁ / K	1063	1091	1093	1111						
Ae ₃ / K	1189	1253	1161	1219						
Creep strength / MPa	294	294	294	294						

Table 9.9: Composition of heat resisting steels which have same creep strength though with varying Ae₁ temperatures.

APPENDIX V

Documentation of programs in the format of Materials Algorithm Project

<http://www.msm.cam.ac.uk/map>

Bibliography

- [1] <http://www.worldsteel.org/>.
- [2] R. D. Stout. and W. D. Doty. *Weldability of Steels*. Welding research council, 1953.
- [3] *Welding Handbook*, volume 3. American Welding Society, Miami, Florida, 7 edition, 1976.
- [4] G. E. Dieter. *Mechanical Metallurgy*. McGraw–Hill Book Company, London, si metric edition, 1988.
- [5] H. K. D. H. Bhadeshia. *Bainite in Steels*. The Institute of Materials, 1 Carlton House Terrace, London, first edition, 1992.
- [6] A. H. Cottrell. In J. A. Charles and G. C. Smith, editors, *Advances in Physical Metallurgy*, pages 181–187. Institute of Metals, 1 Carlton House Terrace, London., 1990. A collection of invited papers presented to mark the 70th birthday year of Prof. Sir Allan Cottrell.
- [7] R. W. K. Honeycomb and H. K. D. H. Bhadeshia. *Steels - Microstructure and Properties*. Edward Arnold, London, second edition, 1995.
- [8] H. K. D. H. Bhadeshia and L. E. Svensson. *Journal of Materials Science*, 21:3947–3951, 1986.
- [9] G. J. Davies and J. G. Garland. *International Metallurgical Review*, 20:83–106, 1975.

- [10] W. F. Savage and A. H. Aaronson. *Welding Journal*, 44:175, 1965.
- [11] C. L. Choi and D. C. Hill. *Welding Journal Research Supplement*, 57-58:23, 1978.
- [12] E. Levine and D. C. Hill. *Metallurgical Transactions*, (8A).
- [13] G. Krauss. In *Hardenability Concepts with Application to Steel*, page 235, 1978.
- [14] G. Rees. PhD thesis, Department of Materials Science, University of Cambridge, 1992.
- [15] H. H. Tweed and J. F. Knott. *Metal Science*, 17:45–54, 1983.
- [16] H. H. Tweed and J. F. Knott. *Acta Metallurgia*, 35:1401–1414, 1987.
- [17] A. A. B. Sugden and H. K. D. H. Bhadeshia. In S. A. David and J. M. Vitek, editors, *Recent Trends in Welding Science and Technology*, 2, pages 745–748, Materials Park, Ohio 44073, 1989. ASM International.
- [18] P. Bowen, S. G. Druce, and J. F. Knott. *Acta Metallurgia*, 34:1121–1131, 1986.
- [19] S. A. David. and J. M. Vitek. Analysis of weld metal solidification and microstructures. In H. Cerjak. and K. E. Easterling., editors, *Mathematical modelling of weld phenomena*, pages 41–59, 1, Carlton House Terrace, London SW1Y5DB, 1993. Institute of Materials.
- [20] O. Grong. *Metallurgical Modelling of Welding*. Institute of Materials, 1 Carlton House Terrace, London SW1Y 5DB, 1994.
- [21] M. C. Flemings. *Solidification Processing*. McGraw-Hill, New York, 1974.
- [22] H. Biloni. *Physical Metallurgy Part I*, page 478. Elsevier, New York, 1983.
- [23] E. Scheil. *Archiv. Eisenhuttenwesen*, (8), 1938.

- [24] M. F. Ashby and D. R. H. Jones. *Engineering Materials-An Introduction to their Properties and Applications*. Pergamon press, Oxford, England, first edition, 1980.
- [25] F. Abe, M. Igarashi, N. Fujitsuna, K. Kimura, and S. Muneki. In Lecomte-Beckers *et al.*, editor, *6th Leige Conference on Materials for Advance Power Engineering*, pages 259–268, October 1998.
- [26] H. Cerjak, H. Peter, and B. Schaffernak. *ISIJ International*, 39(9):874–888, 1999.
- [27] H. K. D. H. Bhadeshia. *ISIJ International*, 41(6):626–640, 2001.
- [28] F. Masuyama. *ISIJ International*, 41(6):612–625, 2001.
- [29] K. Maruyama, K. Sawada, and J. Koike. *ISIJ International*, 41(6):641–653, 2001.
- [30] T. Fujita. In E. Metcalfe, editor, *New steels for Advanced plant up to 620 °C*, pages 190–200, 58, Abingdon Road, Drayton, Oxon, OX14 4HP, UK, May 1995. National Power, PicA.
- [31] T. Fujita. *Metal Progress*, 130:33–36, 1986.
- [32] D. J. C. MacKay. In H Cerjak, editor, *Mathematical Modelling of Weld Phenomena*, 3, pages 359–389. Institute of Materials, 1997.
- [33] Guide to welding and weldability of Ni - alloyed cryogenic steels. Technical Report IX-G-312-83, International Institute of Welding, May 1983.
- [34] W. C. Leslie. *The Physical Metallurgy of Steels*. McGraw-Hill, London, 1981.
- [35] S. Yano *et al.* *Transactions ISIJ*, 13(135):133–140, 1973.
- [36] F. Darrel and J. W. Morris Jr. *Metallurgical Transactions A*, 17A:243–251, 1986.
- [37] Petr PAHUTA, Zdeněk JANÍK, and Ludmila HYSPECKÁ. *Transactions of the Iron and Steel Institute of Japan*, 26(7):649–654, 1986.

- [38] J. I. Kim, C. K. Syn, and J. W. Morris Jr. *Metallurgical Transactions A*, 14A:93–103, 1983.
- [39] J. I. Kim, H. J. Kim, and J. W. Morris Jr. *Metallurgical Transactions A*, 15A:2213–2219, 1984.
- [40] Y. H. Kim, H. J. Kim, and J. W. Morris Jr. *Metallurgical Transactions A*, 17A:1157–1164, 1986.
- [41] B. Fultz, J. I. Kim, Y. H. Kim, G. O. Fior, and J. W. Morris Jr. *Metallurgical Transactions A*, 16A:2237–2249, 1985.
- [42] B. Fultz and J. W. Morris Jr. *Metallurgical Transactions A*, 16A:2251–2256, 1985.
- [43] B. Fultz, J. I. Kim, Y. H. Kim, and J. W. Morris Jr. *Metallurgical Transactions. A*, 17A:967–971, 1986.
- [44] O. Furukimi and Y. Saito. *ISIJ international*, 30(5):390–396, 1990.
- [45] N. Bailey, editor. *Weld pool chemistry and metallurgy*, pages 19–29. The Welding Institute, Abington, 1980.
- [46] S. H. Kim, C. Y. Kang, and K. S. Bang. *Journal of Material Science*, 36(5):1197–1200, March 2001.
- [47] H. J. Kim and J.W. Morris Jr. *Supplement to the Welding Journal*, pages 210s–219s, 1983.
- [48] D. J. Widgery. *Welding Journal*, 55(3):57s–68s, 1976.
- [49] K.W. Mahin., J.W. Morris Jr., and I. Watanabe. In *Advances in the Cryogenic Eng.*, volume 26, pages 187–199, 1980.

- [50] S. Jin, J. W. Morris Jr, and V. F. Zackay. *Metallurgical Trans.*, 6A(1):141–149, 1975.
- [51] S. K. Hwang and J. W. Morris JR. *Metallurgical Transactions A*, 11A:1197–1206, 1980.
- [52] B. J. Kang, H. J. Kim, and S. K. Hwang. *ISIJ International*, 40:1237–1245, 2000.
- [53] L. E. Svensson. *Control of Microstructure and Properties in Steel Arc Welds*. CRC press, Inc., 2000 Corporate Blvd., N.W., Boca Raton, Florida 33431, 1994.
- [54] M. Lord. *Design and Modelling of ultra-High Strength Steel Weld Deposits*. PhD thesis, University of Cambridge, March 1999.
- [55] J. W. Morris, Jr. *ISIJ International*, 41(6):599–611, 2001.
- [56] B. D. Cullity. *Elements of X-ray diffraction*. Reading, MA, Addison-Wesley, 1959.
- [57] Dickson. *Acta Crystallographica*, 2:176–180, 1969.
- [58] xrdcalc, <http://www.msm.cam.ac.uk/map/map.html>.
- [59] D. J. C. MacKay. *Neural Computation*, 4:448–472, 1992.
- [60] H. K. D. H. Bhadeshia, D. J. C. MacKay, and L. E. Svensson. *Mater. Sci. Technol.*, volume 11:1046, 1995.
- [61] S. H. Lalam, H. K. D. H. Bhadeshia, and D. J. C. Mackay. *Science and Technology of Welding and Joining*, 5:135–147, 2000.
- [62] D. J. C. MacKay. *Neural Computation*, 4:415–447, 1992.
- [63] P. M. Lee. *Bayesian Statistics*. Edward Arnold, London, 1989.

- [64] H. K. D. H. Bhadeshia. In *Proceedings of the 6th International Conference on Trends in Welding Research*, Atlanta, Georgia, USA, 2002. ASM International, ASM International. in press.
- [65] <http://www.msm.cam.ac.uk/map/map.html>.
- [66] R. C. Reed and H. K. D. H. Bhadeshia. In S. A. David and J. M. Vitek., editors, *Recent Trends in Welding Science and Technology*, pages 205–209, 1989.
- [67] W. C. Leslie. *Metallurgical transactions*, 3, 1972.
- [68] H. K. D. H. Bhadeshia, L. E. Svensson, and B. Gretoft. *Acta Metallurgica*, 33:1271–1283, 1985.
- [69] S. M. Hodson. MTDATA - Metallurgical and Thermochemical Databank. National Physical Laboratory, Teddington, U.K., 1989.
- [70] B. A. Marlow. In A. Strang, W. M. Banks, R. D. Conroy, and M. J. Goulette, editors, *Advances in Turbine Materials, design and manufacturing*, pages 36–45. Institute of materials, London, 1997.
- [71] R. B. Scarlin. In A. Strang, W. M. Banks, R. D. Conroy, and M. J. Goulette, editors, *Advances in Turbine Materials, design and manufacturing*, pages 242–256. Institute of materials, London, 1997.
- [72] E. Metcalfe and B. Scarlin. In Lecomte-Beckers, F. Schubert, and P. J. Ennis, editors, *Materials for Advanced Power Engineering*, pages 35–46. Forschungszentrum Jülich GmbH, 1998.
- [73] D. V. Thornton and K. H. Mayer. In R. Viswanathan and J. Nutting, editors, *Advanced Heat Resistant Steels for Power Generation*, pages 349–364. Institute of Materials, 1999.

- [74] B. A. Marlow. In A. Strang *et al.*, editor, *Advanced Materials for 21st Century Turbines and Power Plants*, pages 40–57. Institute of materials, London, 1997.
- [75] H. Mimura, M. Ohgami, H. Naoi, and T. Fujita. In D. Coutsouradis *et al.*, editor, *Materials for Advanced Power Engineering, Part I*, pages 361–372. kulwer academic publishers, 1994.
- [76] P. J. Ennis and W. J. Quadakkers. In A. Strang and W. M. Banks, editors, *Parsons 2000, Advanced Materials for 21st Century Turbines and Power Plant*, pages 265–275, 2000.
- [77] F. Masuyama. In *Advanced Heat Resistant Steels for Power Generation*. IOM Communications, 1998.
- [78] P. J. Ennis, Y. Wouters, and W. J. Quadakkers. In *Advanced Heat Resistant Steel for Power Generation*.
- [79] F. Abe and S. Nakazawa. *Materials Science and Technology*, 8:1063–1069, 1992.
- [80] A. Iseda, Y. Sawaragi, S. Kato, and F. Masuyama. In *Creep: Characterisation, Damage and Life Assessments Proceesings of the fifth International Conference on Creep of Materials*, Lake Buena Vista, Florida, U.S.A., 1992.
- [81] V. Vodárek and A. Strang. *Scripta Materialia*, 38(1):101–106, 1998.
- [82] V. Vodárek and A. Strang. Int. conf. on microstructural stability of creep resistant alloys for high temperature plant application. Sheffield, UK, 1997.
- [83] T. Tsuchiyama, Y. Futamura, and A. Takaki. In *Creep and Fracture of Engineerying Materials and Structures, Key Engineering Materials*, volume 171–174, pages 411–418.
- [84] M. Igarashi and Y. Sawaragi. In *ICOPE'97*, volume 2, pages 107–112, Tokyo, 1997.

- [85] K.J. Irvine, D. J. Crowe, and F. B. Pickering. *Journal of Iron and Steel Institute*, pages 386–405, 1960.
- [86] K. Hidaka, Y. Fukui, S. Nakamura, R. Kaneko, Y. Tanaka, and T. Fujita. In R. Vishwananth and J. Nutting, editors, *Advanced Heat Resistant Steel for Power Generation*, pages 418–429, San Sebastian, Spain, 1998.
- [87] K. Yoshikawa, A. Iseda, M. Yano, F. Masuyama, T. Daikoku, and H. Haneda. In *First International Conference on Improved Coal-Fired Power Plants*, Palo Alto, California, 1986.
- [88] H. Naoi, H. mimura, M. Ohgami, H. Morimoto, T. Tanaka, Y. Yazaki, and T. Fujita. In E. Metcalfe, editor, *New steels for Advanced plant up to 620 °C* , pages 8–29, 58, Abingdon Road, Drayton, Oxon, OX14 4HP, UK, May 1995. National Power, PicA.
- [89] V. Foldyna, Jakobová, R. Riman, and A. Gemperle. *Steel Research*, 62(10):453–458, 1991.
- [90] J. Hald. In E. Metcalfe, editor, *New steels for Advanced plant upto 620 °C* , pages 152–173, 58, Abingdon Road, Drayton, Oxon, OX14 4HP, UK, May 1995. National Power, PicA.
- [91] K. S. Park, F. Masuyama, and T. Endo. In *Advanced Heat Resistant Steels for Power Generation*, pages 596–607. IOM Communications, 1998.
- [92] M. Morinaga, R. Hashizume, and Y. Murata. In D. Coutsouradis *et al.*, editor, *Materials for Advanced Power Engineering, Part I*, page 319. Kluwer Academic Publishers, Dordrecht, 1994.
- [93] F. Masuyama and N. Komai. In J. Lecomte-Beckers, F. Schubert, and P. J. Ennis, editors, *Materials for Advanced Power Engineering*, pages 269–276, Germany, 1998. Forschungszentrum Juelich.

- [94] M. Ohgami, H. Mimura, H. Naoi, and T. Fujita. In *Proceedings of the Fifth International Conference on Creep of Materials*, pages 69–73, Lake Buena Vista, Florida, U.S.A., 1992.
- [95] R. Ishii, Y. Tsuda, M. Yamada, and M. Miyazaki. In R. Vishwananth and J. Nutting, editors, *Advanced Heat Resistant Steel for Power Generation*, pages 277–287, San Sebastian, Spain, 1998.
- [96] N. Komai, F. Masuyama, I. Ishihara, T. Yokoyama, Y. Yamadera, H. Okada, K. Miyata, and Y. Sawaragi. In R. Vishwanathan and J. Nutting, editors, *Advanced Heat Resistant Steel for Power Generation*, pages 96–108, San Sebastian, Spain, 1998.
- [97] T. Fujita and N. Takahashi. *Transactions ISIJ*, 18:269–278, 1978.
- [98] J. Pilling, N. Ridley, and D. J. Gooch. *Metallurgical Transactions A*, 14A:1443–1449, 1983.
- [99] L. J. Cuddy, H. E. Knechtel, and W. C. Leslie. *Metallurgical Transactions*, 5:1999–2003, 1974.
- [100] F. Masuyama and M. Ohgami. In *Proceedings of JIMIS-7*, pages 325–332, Nagoya, 1993.
- [101] D. J. Gooch. *Metals Science*, 16:79–89, 1982.
- [102] T. Fujita. *Supplement, Transactions of Japanese Institute of Metals*, 1978.
- [103] F. Masuyama and M. Ohgami. In Y. Hosoi, H. Yoshinaga, H. Oikawa, and K. Maruyama, editors, *Symposium on Aspects of High Temperature Deformation and Fracture in Crystalline Materials*, pages 325–332, Nagoya, 1993. Japan Institute of Metals.

- [104] L. Lundin. *High Resolution Microanalysis of Creep Resistant 9–12 wt% Chromium Steels*. PhD thesis, Chalmers University of Technology, 1995.
- [105] T. Horiuchi, M. Igarashi, and F. Abe. *ISIJ International*, 42, Supplement:s67–s71, 2002.
- [106] P. N. Ernst, P. J. Uggowitzer, and M. O. Speidel. *Journal of Materials Science Letters*, (5):835–839, 1986.
- [107] Y. Tsuchida, R. Yamaba, K. Tokuno, K. Hasimoto, T. Ogawa, and T. Takeda. Internal report. Technical report, Nippon Steel Corporation, 1990.
- [108] K. Miyata, M. Igarashi, and Y. Sawaragi. *ISIJ International*, 39(9):947–954, 1999.
- [109] J. H. Woodhead and A. G. Quarrel. *Journal of Iron and Steel Institute*, 203:605–620, 1965.
- [110] Hosoi, Wade, and Urita. *Tans. ISIJ*, 26:B–30, 1986.
- [111] N. Fujitsuna, M. Igarashi, and F. Abe. *Key Engineering Materials*, 171–174:469–476, 2000.
- [112] A. Strang. and M. McLean., editors. *Modelling of microstructure evolution of creep resistant materials*, number 3.
- [113] Modelling phase transformation in steels. University of Cambridge, Programme for Industry, 30th March - 1st April 1998.
- [114] F. Abe. In T. Sakai and H. G. Suzuki, editors, *Fourth International Conference on Recrystallisation and Related Phenomena*, pages 289–294. The Japan Institute of Metals, October 1999.
- [115] R. F. Decker. and S. Floreen. In G. R. Speich. and J. B. Clark., editors, *Precipitation from iron-base alloys*, pages 69–139, 1963.

- [116] B. A. Senior. *Material Science and Eng.*, 119A:L5–L8, 1989.
- [117] Schwind, Hättestrand, and Andren. High resolution microanalysis of ferritic steel HCM12A. Technical report, Sweden, 1996.
- [118] K. Kuo. *Journal of Iron and steel Institute*, 173:363, 1953.
- [119] J. Beech. and D. H. Warrington. *Journal of Iron and Steel Institute*, 204:460, 1966.
- [120] Janovec, Vyrostkova, and Svoboda. *Metallurgical Transactions A*, 25A:267–275, 1994.
- [121] F. Barcelo and J. C. Brachet. *La Revue de Métallurgie - CIT / Science & Génie des Matériaux*, pages 255–266, 1994.
- [122] J. C. Brachet and A. Alamo. *Mem. and Edition Science – Revue de Metallurgie*, pages 33–46, 1990.
- [123] A. Alamo and J. C. Brachet. *Journal of Nuclear Materials*, 258–263:1228–1235, 1998.
- [124] R. C. Thomson. PhD thesis, University of Cambridge, U.K, 1992.
- [125] R. G. Baker. and J Nutting. *Journal of Iron steel Inst.*, 192:257–268, 1959.
- [126] *Selected powder diffraction data for metals and alloys-Data book*, volume II. JCPOS, first edition, 1978.
- [127] H. K. D. H. Bhadeshia. In A. Strang and W. M. Banks, editors, *Parsons 2000, Advanced Materials for 21st Century Turbines and Power Plant*, pages 3–39, 2000.
- [128] D. Venugopalan and J. S. Kirkaldy. Hardenability concepts with applications to steels. In D. V. Doane and J. S. Kirkaldy., editors, *TMS-AIME*, pages 249–267, Warrendale, Pennsylvania, 1978.

- [129] M. Ohgami, Y. Hasegawa, H. Naoi, and T. Fujita. In *IMEchE International Conference on Steam Power Plant*, pages 115–124, 1997.
- [130] D. Cole, C. Martin-Moran, A. G. Sheard, H. K. D. H. Bhadeshia, and D. J. C. MacKay. *Science and Technology of Welding and Joining*, 5:81–90, 2000.
- [131] Meyer. B and Gutte H. *Steel Research*, 72(9):361–365, 2001.
- [132] R. Viswanathan. *Metals Technology*, 1:284–293, June 1974.
- [133] C. A. Parsons. The steam turbine. In *Rede Lecture*, Cambridge, U.K, 1911. Cambridge University Press.
- [134] J. D. Baird. and A Janieson. *Journal of Iron Steel Inst.*, 210:841, 1972.
- [135] Y. Sawaragi, A. Iseda, K. Ogawa, F. Masuyama, and T. Yokoyama. In E. Metcalfe, editor, *New steels for Advanced plant upto 620 °C* , pages 45–55, 58, Abingdon Road, Drayton, Oxon, OX14 4HP, UK, May 1995. National Power, PicA.